UNIVERSITY OF VIRGINIA

Neutron Scattering Study on BiS_2-based Superconductors

by

Jooseop Lee

A thesis submitted in partial fulfillment for the degree of Doctor of Philosophy

in the

Department of Physics
University of Virginia

October 2013

"If I have ever made any valuable discoveries, it has been due more to patient attention, than to any other talent."

Isaac Newton

"Most people say that it is the intellect which makes a great scientist. They are wrong: it is character."

Albert Einstein

Abstract

The recent discovery of a new type of superconductors based on BiS_2 layers has excited the scientific community due to its structural similarities with other unconventional superconductors, such as cuprates and Fe-based superconductors. If the superconducting mechanism of BiS_2-based superconductors is unconventional, it will yield a new route to better understand the long-unsolved puzzle of unconventional superconductivity. Hence, it is crucial to determine the superconducting mechanism and the nature of superconductivity in this system.

There are contradicting scenarios regarding the superconducting mechanism in this system. The band structure calculation indicates the existence of Fermi surface nesting, like in iron pnictides, supporting a non-phonon mediated superconductivity. On the other hand, the electron-phonon coupling constant was calculated to be large enough to reproduce the reported T_c, suggesting an conventional phonon mediated superconductivity. Experiments to test these theoretical predictions are limited, however.

To tackle the controversy over the role of phonons in this system, we have performed elastic and inelastic neutron scattering measurements on polycrystalline samples of non-magnetic $La(O,F)BiS_2$ and magnetic $CeO_{0.3}F_{0.7}BiS_2$. We have examined its crystal structure and lattice vibrational modes, and compared these results with density functional perturbation calculations. We could not find any meaningful change related to superconductivity in the phonon density-of-states either by F-doping or by cooling through the transition temperature. This suggests that the possible electron-phonon coupling in this material is much weaker than expected based on theoretical calculations, implying this new BiS_2-based superconductors can be unconventional.

For the ferromagnetic $CeO_{0.3}F_{0.7}BiS_2$, we have studied the interplay of magnetism with superconductivity. This system exhibits the rare and interesting case of the coexistence of ferromagnetism and superconductivity, which is not realized in in the conventional phonon mediated superconductors due to their antagonistic nature.

The crystal and magnetic structures have been investigated together with the spin fluctuations, and we determined the spin Hamiltonian describing the spin dynamics in this system. In addition, we have examined the external magnetic field dependence of both magnetic structure and its excitation. Under field, the magnetic structure changes from ferromagnetic with the spins pointing along the c-axis to ferromagnetic in the ab-plane, and the spin fluctuation dispersion splits into two. While the splitting of spin excitations in a ferromagnet is untypical which needs further investigation, it seems that superconductivity is robust against a magnetic field and there is no direct relationship between magnetism and superconductivity in this system.

Our neutron scattering study on the crystal structure, lattice vibrations, and magnetism in the BiS_2-based superconductors will help us to understand the mechanism of superconductivity and its relationship with other degrees of freedom.

Acknowledgements

First and foremost, I would like to express my sincere gratitude to my advisor Prof. Seunghun Lee for his continuous guidance and support of my Ph.D study. His patience, motivation, enthusiasm, and immense knowledge were crucial to my development. I could not have imagined having a better advisor and mentor.

Besides my advisor, I would like to thank the rest of my thesis committee: Prof. Despina Louca, Prof. Israel Klich, and Prof. Leonid Zhigilei.

My sincere thanks also goes to Dr. Garrett Granroth for offering me the opportunity to pursue further studies in his excellent groups at SNS, ORNL, and for all the kindness he showed during the admission process. I would like to also thank to Dr. Masaaki Matsuda and Dr. Jaime Fernandez-Baca for having me as a visiting graduate student in their groups at HFIR, ORNL, and giving me lots of chances to work on diverse, exciting projects. I also appreciate the valuable experiences I shared with Prof. Taku Sato at University of Tokyo, and Dr. Igor Zaliznyak at BNL.

I am grateful to all my neutron instrument scientists collaborators: Dr. Doug Abernathy at ARCS, Dr. Vasile Ovidiu Garlea and Dr. Clarina Dela Cruz at HB-2A, Dr. Songxue Chi at WAND, Dr. Tao Hong at CTAX, Dr. Lee Robertson at CG-1B, Dr. Mark Green at BT-1, Dr. Yiming Qiu at DCS, Dr. Tatiana Guidi at Merlin, Dr. Ryoichi Kajimoto at 4SEASON, Dr. Kirrily Rule and Dr. Manh Duc Le at V2, and many others, for their earnest help. I would like to give my special thanks to my collaborators for this thesis work: Dr. Matthew Stone at ARCS, Dr. Georg Ehlers at CNCS, and Dr. Ashfia Huq at POWGEN. Without their collaboration, I could not have finished my degree.

I thank my present and former fellow labmates in University of Virginia: Sachith Dissanayake, Dr. Sungdae Ji, Dr. Naoyuki Katayama, Dr. Kazuki Iida, for the stimulating discussions and for all the fun we had together. Martin Lehmann in physics department helped me quickly proofread and gave constructive suggestions.

Last but not the least, I would like to thank my family: my parents, for giving birth to me, loving me, and supporting me spiritually throughout my life. I am also deeply grateful to Hyunjin Oh, my soon-to-be wife. She has been more than supportive for all the struggles I have encountered throughout this process. Writing this dissertation would never have been possible without her, and, above all, I would like to acknowledge her as I love her so much.

Contents

List of Figures

List of Tables

Abbreviations

BCS	**B**ardeen, **C**ooper, and **S**chrieffer
SC	**S**uper**C**onductor (**C**onducting, **C**onductivity)
AFM	**A**nti**F**erro**M**agnetism (**M**agnetic)
DOS	**D**ensity **O**f **S**tates
PDOS	**P**honon **D**ensity **O**f **S**tates
GDOS	**G**eneralized **P**honon **D**ensity **O**f **S**tates
FSN	**F**ermi **S**urface **N**esting
HP	**H**igh **P**ressure
CDW	**C**harge **D**ensity **W**ave
SDW	**S**pin **D**ensity **W**ave
E-Ph	**E**lectron **Ph**onon
QE	**Q**uantum **E**spresso
PWscf	**P**lane **W**ave **s**elf **c**onsistent **f**ield

Physical Constants

Plank Constant	h	$=$	$6.62606957(29) \times 10^{-34} J \cdot s$
		$=$	$4.135667516(91) \times 10^{-15} eV \cdot s$
Reduced Plank Constant	$\hbar$	$=$	$1.054571726(47) \times 10^{-34} J \cdot s$
		$=$	$6.58211928(15) \times 10^{-16} eV \cdot s$
Mass of Electron	m_e	$=$	$9.10938215(45) \times 10^{-31} kg$ (rest)
Bohr Magneton	$\mu_B (= \frac{e\hbar}{2m_e})$	$=$	$9.27400968(20) \times 10^{-21} erg \cdot G^{-1}$
		$=$	$5.7883818066(38) \times 10^{-5} eV \cdot T^{-1}$
Speed of Light	c	$=$	$2.997\ 924\ 58 \times 10^{8}\ \mathrm{ms}^{-\mathrm{S}}$ (exact)

Symbols

Γ	(0, 0, 0)	(center of the Brillouin zone)
M	(π, π, 0)	(in P 4/n m m space group)
E ($=\hbar\omega$)	Energy transfer	meV
p ($=\hbar\vec{Q}$)	Momentum transfer	kg m/s
Ω	Solid angle	sr (Steradian: dimensionless)
σ	scattering cross section	$b(1barn = 10^{-28}m^2)$
$d^2\sigma/d\Omega_f dE_f$	differential scattering cross section	$bsr^{-1}eV^{-1}$
$S(\vec{Q},\omega)$	scattering function	$b^{-1}sr^{-1}eV^{-1}$

Dedicated to my parents

Chapter 1

Introduction to Superconductivity

1.1 Introduction to conventional superconductivity

Superconductivity is characterized by the emergence of zero electrical resistivity [1] and expulsion of magnetic flux, i.e. Meissner effect [2], when a material is cooled below a critical temperature. The historical plot of first observed superconductivity by Onnes is shown in Figure 1.1. The discovery of superconductivity has continued to fascinate the world over a century since it was first discovered not only because of its wide variety of practical importance but because of its fundamental challenge to our understanding of quantum phenomena in a solid.

Superconductivity is by itself practically so attractive considering we lose about 13(10)% [3] of total energy while transferring electrical power from one place to another, and has become a keyword for the future solution for the energy crisis. Furthermore, superconductivity has various comtemporary applications such as MRI (Magnetic Resonance Image) in medicine, MagLev Train (Magnetic Levitation Train), and SQUID (Superconducting Quantum Interference Device) for magnetic moment measurement. The practical importance of superconductivity technology will become more significant as its onset temperature gets higher, thus being accessible with lower

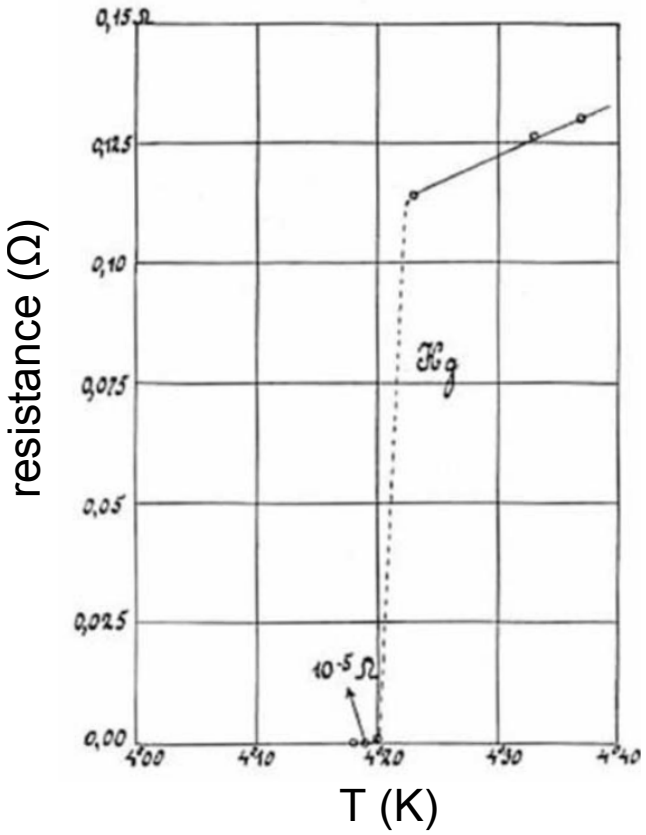

FIGURE 1.1: The first discovery of superconductivity in Hg by H. K. Onnes in October 1911. The resistance (in Ω) versus temperature (in K) graph shows the sudden drop of resistance at 4.20 K. Within 0.01 K, the resistance jumps from infinitesimally small value, less than $10^{-6}\Omega$, to a finite value of about 0.1 Ω. This figure was taken from Reference [4].

cost for cooling.

Superconductivity is interesting from a theoretical perspective as well since zero resistivity in impossible in a classical theory of a metal. Every metal is expected to have nonzero resistivity at a finite temperature due to the scattering of electrons by lattice vibrations. Even at zero temperature, a finite resistivity is expected due to scatterings from impurities and imperfections in the crystal lattice itself.

1.1.1 Introduction to BCS theory

Only after more than half-century of its first discovery, a working theory on superconductivity was developed by Bardeen, Cooper and Schrieffer [5–7]. In the BCS theory, two electrons form a bosonic pair, named Cooper pair, by the exchange of a phonon. Cooper showed when there is an arbitrary small attractive interaction, the pairing is favored having an energy gap, Δ, below the Fermi surface. In a classical picture, as an electron passes by positive ions in a lattice, it will attract the surrounding ions via Coulomb interaction, which in turn drags another electron having opposite spin and opposite momentum. In other words, two electrons can be coupled with a lattice vibration, i.e. phonon, which is illustrated in Figure 1.2.

As the total spin of this Cooper pair is an integer, it follows Bosonic statistics. Thus, the Cooper pairs can condense into a ground state with a finite energy gap in the excitation spectrum below a certain temperature, and superconductivity emerges. Below the transition temperature, this gap prevents scattering of electrons. Hence, the condensates, or the coherent superposition of Cooper pairs, can flow without any resistance as long as an external perturbation energy scale is smaller than the gap. The gap can be measured experimentally with, for example, tunneling measurements, and specific heat measurements. The Cooper pair boson condensate is an important example of quantum mechanical phenomena manifested at a macroscopic level.

In the BCS formulation, the mediating interaction is related with the shape of a gap via the self-consistent equation [17],

$$\Delta_{\vec{k}} = -\frac{1}{2}\sum_{\vec{k'}} \frac{\Delta_{\vec{k'}}}{(\Delta_{\vec{k}}^2 + \xi^2)^{1/2}} V_{\vec{k}\vec{k'}} \tag{1.1}$$

$$\xi = \epsilon_{\vec{k}} - \epsilon_F$$
$$V_{\vec{k}\vec{k'}} = \Omega^{-1} \int V(\vec{r})\ e^{i(\vec{k'}-\vec{k})} d\vec{r}$$

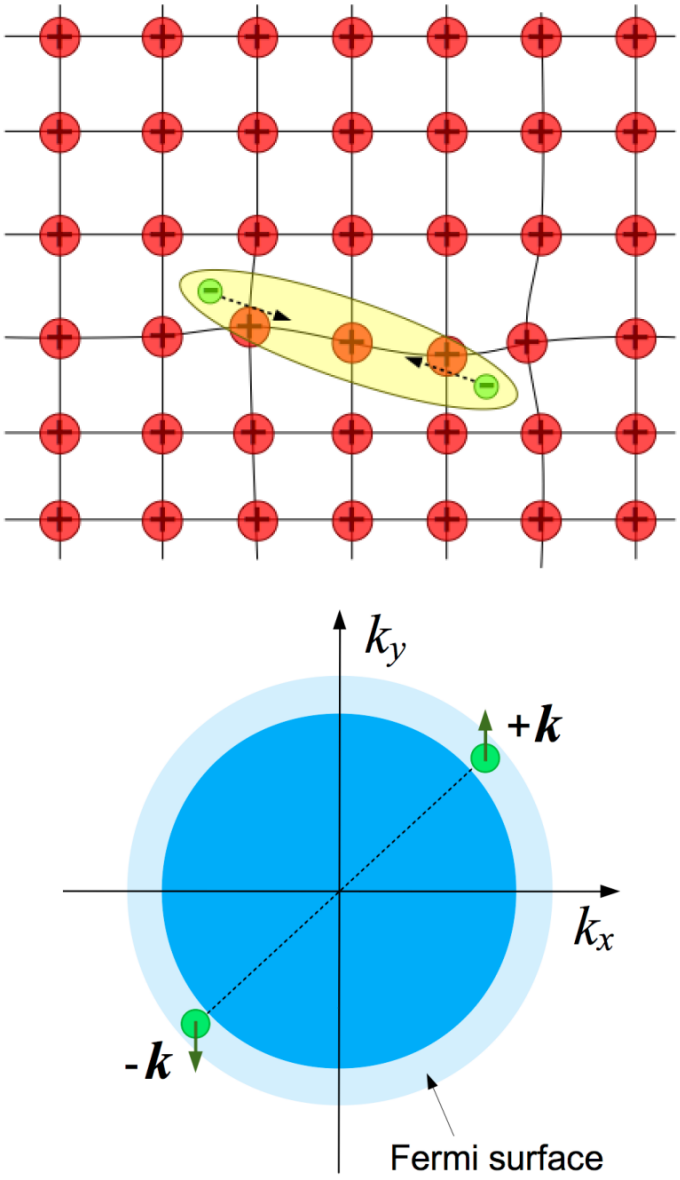

FIGURE 1.2: (top) Schematic figure of Cooper pair formation. Two electrons (green circles) are bound together forming a Cooper pair (yellow oval) by the deformation of background positive ions (red circles). The size of Cooper pair is given by the coherence length typically ranging from 10 Å to 1000 Å. (bottom) Schematic figure in momentum space showing the two interacting electrons. They have opposite momenta and spins, and they are paired with exchange of phonon. The Fermi sphere, and Fermi surface are shown with blue and light-blue circles. These figures were taken from Reference [8].

where ξ is the difference between the single particle energy ($\epsilon_{\vec{k}}$) and the Fermi energy (ϵ_F), and $V_{\vec{k}\vec{k'}}$ is the matrix component of the Fourier transformed interaction potential. From this equation, we can see the mediating interaction has significant effect on the nature of superconductivity as it is governed by the gap function.

BCS theory assumes (1) a k-independent weak attractive interaction, and (2) a spherical Fermi surface. In the case of conventional phonon mediated superconductivity, $V_{\vec{k}\vec{k'}}$ can be well described as a rectangular function which is a constant in a thin shell of thickness $\hbar\omega_c$ around the Fermi surface, and zero elsewhere.

Converting the sum in the equation 1.1 to an integral and substituting ω_c with the Debye phonon cutoff frequency, ω_D [17],

$$2\Delta = \frac{\hbar\omega_D}{\sinh[1/(VN(E_F))]} \approx 4\hbar\omega_D e^{-1/(N_F V)}. \tag{1.2}$$

Here, V is the magnitude of constant electron-phonon coupling interaction, and N_F is the density of normal-state electrons at the Fermi energy. It is clear that the isotropic electron-phonon interaction leads to an isotropic gap sitting at the Fermi surface, while the gap magnitude is proportional to the Debye phonon frequency and inversely proportional to the density of states on the Fermi surface. In normal state metal, the energy states exist continuously up to Fermi energy at T = 0 K, and the states up to Fermi energy are occupied by electrons. In a superconducting state, on the other hand, the gap centered at Fermi energy pushes allowed states outside the gap.

The temperature dependence of the gap, $2\Delta(T)$ can be analytically determined to be

$$\Delta(T) \approx AT_c\sqrt{1 - T/T_c} \qquad \text{for T ¡ } T_c \tag{1.3}$$

with the coefficient A = 3.06.

Furthermore, the transition temperature T_c can be determined in terms of three basic material parameters:

Material	T_c (K)	Θ_D (K)	$N(E_F)$	$\frac{2\Delta}{k_B T_c}$	λ_{ep}
Nb	9.25	276	0.91	3.6	0.85
V	5.40	383	1.31	3.4	1.0
Hg	4.19	87	0.15	4.6	1.6
Nb_3Ge	23.2	302	0.95	4.2	1.8
V_3Ga	16.5	310	2.7	4.0	1.17
V_3Si	17.1	330	2.5	3.6	1.10
$PbMo_6S_8$	15.3	411	0.67	3.84	1.20

TABLE 1.1: Properties of selected superconductors, taken from Reference [17].

$$k_B T_c = 1.13\ \hbar\omega_D\ exp\left[-1/\left\{VN(E_F)\right\}\right] \tag{1.4}$$

Thus, larger values of ω_D, V, and $N(E_F)$ will result in higher transition temperature. Practically, it is relatively easy to control ω_D or $N(E_F)$: ω_D can be increased by replacing ions with those with lighter mass, and $N(E_F)$ can be tuned by chemical doping. Meanwhile, V, electron-phonon coupling in BCS superconductor, is known to become significant near a structural phase transition, but is hard to control or predict [18].

By comparing Equation 1.2 and 1.4, one can find a direct relationship between the magnitude of the superconducting gap and superconducting transition temperature, T_c,

$$\frac{2\Delta}{k_B T_c} = 3.52 \tag{1.5}$$

This ratio has been confirmed in wide range of conventional superconductors as shown in Table 1.1.

There are many additional experimental observations that support the phonon-mediated BCS theory. Since the phonon frequencies depend on the mass of vibrating ions as $\sqrt{M}$, we can observe re-normalized superconductivity when the related ions have been replaced with an isotope with different mass. We can also observe changes in the particular phonon line shapes upon cooling into the superconducting phase. The

width of phonon peak along energy at a specific wave vector can be measured experimentally, for example, in neutron scattering. Strong electron-phonon coupling often lead to an increase of phonon line width when the system becomes superconducting.

The BCS theory was so successful that it could explain many conventional superconductors found by that time. The examples include elemental superconductors such as Hg, and Nb, or metal alloy superconductors like Nb_3Ge, and NbTi. Further work on BCS theory extended its applicability to explain some of the type II superconductors. Later in 2001, Jun Akimitsu in Japan found superconductivity in MgB_2 [19] at a relatively high temperature of $T_C \approx 39K$, which was also understood in the extended framework of BCS theory with a large electron-phonon coupling constant [20], λ, of ≈ 0.9.

1.1.2 MgB_2 as a conventional phonon mediated superconductor

It was clear that from the isotope effect, shown in Figure 1.3 the superconductivity in MgB_2 is due to electron-phonon coupling [21]; the transition temperature was reduced by 1 K when ^{10}B ions were replace with ^{11}B. However, there exist some peculiarities as well.

1. No isotope effect was found when ^{24}Mg ions were replaced with ^{25}Mg [22].
2. Given the fact that $N(E_F)$ is relatively low [27] and ω_D is comparable with other diboride systems, the transition temperature is unusually high.
3. The resistivity in normal, non-superconducting state was too low than what should be expected for a system with strong electron-phonon interaction [23, 24].
4. Both resistivity and upper critical field were anisotropic [28, 29].
5. The heat capacity measurements shows a shoulder at low temperature deviating the BCS expectation [30, 31].

This singularities could be explained with highly selective electron-phonon coupling and two nearly-noninteracting bands of different character [25–27]. (1) and (2) are the consequences of selective electron-phonon coupling, while (3), (4) and (5) are the results of two-band structure.

In a graphite-type structure of boron, as shown in Figure 1.3, 2D σ-bonding connects intra-layer boron ions, while 3D π-bonding connects inter-layer boron ions. Furthermore, there is very little hopping of electrons between two bands. The existence of two bands with different dimensionality and electron-phonon coupling results in the above-mentioned properties such as the anisotropy in resistivity and upper critical field.

Among these two bands, the 2D σ band has a strong electron-coupling because electrons are concentrated in the B-B axes rather than being spread out like in normal metal system. Therefore, the high frequency in-plane boron vibration are especially strongly-coupled to the electronic states in the σ band, and its energy replaces $\hbar\omega_D$, resulting in high transition temperature. In addition, this highly-selective electron-phonon coupling leads to the substantial effects from B-isotope and negligible effects from Mg-isotope.

Therefore, MgB_2 is a conventional phonon-mediated s-wave pairing symmetry superconductor with two gap coming from different electron-phonon coupling in 2D σ and 3d π bands.

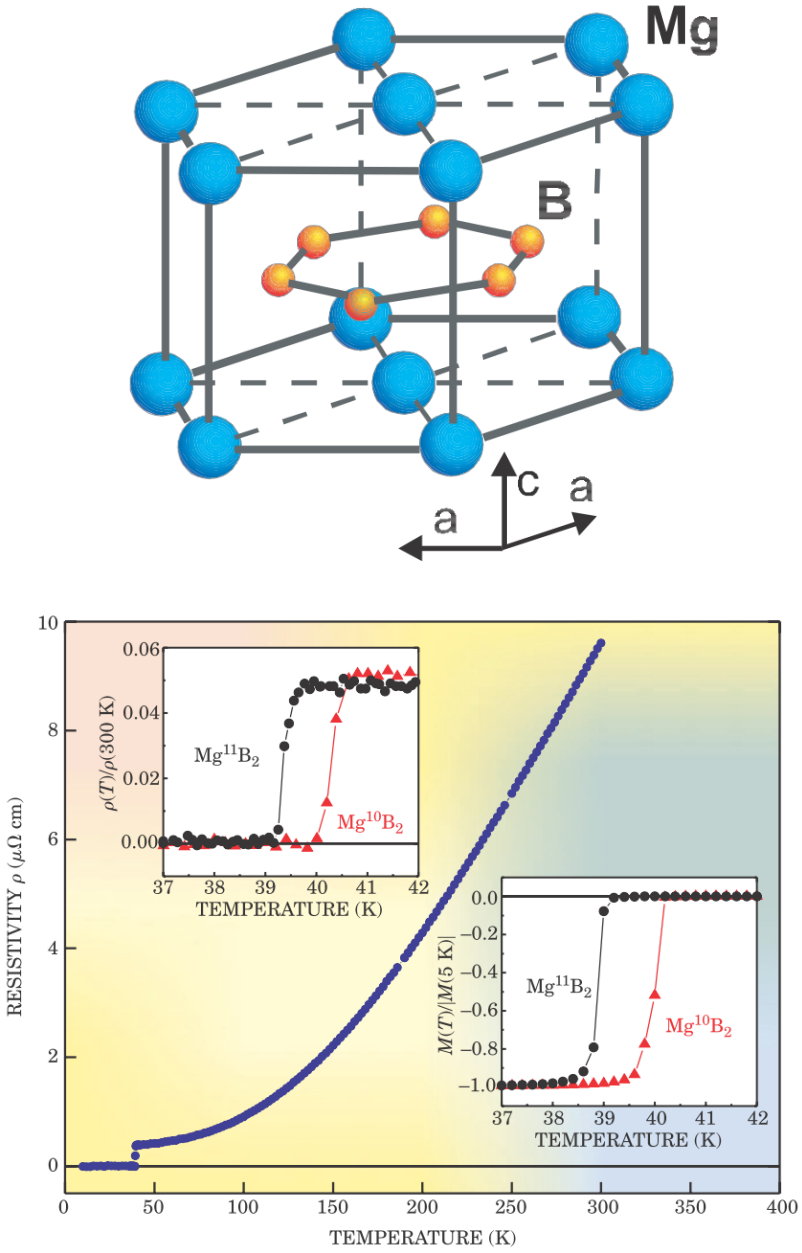

FIGURE 1.3: (top) The crystal structure of MgB_2 composed of graphite-type Boron (Yellow) layers separated by HCP layers of Magnesium (Blue). (bottom) Resistivity [32] of MgB_2 as a function of temperature. Clear onset of superconducting phase transition is observed around $T_c \approx 40$K. The insets show isotope effect of replacing ^{10}B with ^{11}B in normalized resistivity (left), or in normalized magnetization (right). Temperature reduction of about 1K are observed in both measurements, suggesting the mechanism of superconductivity in MgB_2 is related with lattice vibration. These figures were taken from Reference [18].

1.2 Introduction to unconventional superconductivity

1.2.1 Discovery of cuprates and Fe-based superconductors

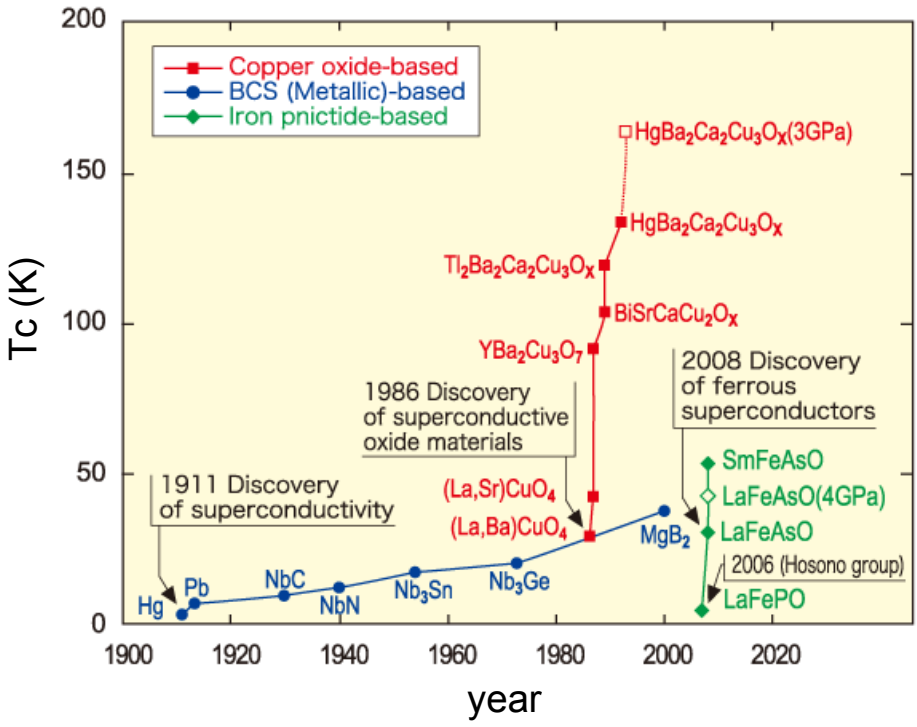

FIGURE 1.4: Timeline of superconducting materials and their transition temperature. The Conventional BCS superconductors, cuprates, and iron-pnictides are represented as blue circle, red square, and green diamond symbols. This figure was taken from Reference [33].

The discovery of superconductivity in $La_{2-x}Ba_xCuO_4$ at $T_c \approx 35$K [34] by Bednorz and Muller in 1986 came as a shock to the scientific community. It was because the conventional phonon mediated mechanism would give the onset temperature of superconductivity around 20K at most, due to the retarded slow interaction between electron and phonon [35]. As illustrated in Figure 1.4, the highest transition temperature before the discovery of cuprates was only about 23 K in Nb_3Ge.

The discovery of the Cu-based superconductors was immediately followed by a flurry of actions in the filed, which revealed related compounds with T_c as high as 153 K in $HgBa_2Ca_2Cu_3O_8$ [36] under external pressure. This new type of superconductors has been named cuprates since every compound contains Cu^{2+} ion square lattice layers as a common building block.

There were many indications that the superconducting mechanism of cuprates could be different from the conventional one. This was clearly demonstrated from the "Matthias' Rules", named after Bernd T. Matthias, which is the rule of thumb for successful searches for new superconductors before the cuprate. The "Matthias' Rules" state:

- high symmetry is good, cubic symmetry is best
- high density of electronic states is good
- stay away from oxygen
- stay away from magnetism
- stay away from insulators
- stay away from theorists

Most of these rules were proven incorrect for the case of cuprates, with possible exception of the last rule. The undoped cuprates are an insulators with tetragonal or orthorhombic symmetry and with moderate carrier density. Most importantly, their electron-phonon coupling was found not enough to induce the observed high T_C, and as such, the cuprate was considered as an unconventional superconductor as opposed to the conventional phonon mediated superconductor.

More importantly, the undoped cuprates exhibit antiferromagnetic (AFM) order. It was quite unexpected considering that a magnetic moment was known to break

Cooper pairs. Of course, superconductivity to emerge, the magnetic moment is suppressed as shown by a representative phase diagram in Figure 1.5: the magnetic order is suppressed with hole or electron doping, and upon further doping superconductivity arises. The proximity of the SC phase to the AFM phase was very unexpected. Furthermore, while the static magnetic order vanishes as superconductivity emerges, the strong magnetic fluctuation survives inside the superconducting phase.

In year 2008, another new family of unconventional superconductors based on $3d^6$ Fe^{2+} ion, that is strongly magnetic when isolated. Thus magnetism must be closely related to superconductivity in these unconventional superconductivity.

The iron-based superconductors family are usually called after the chemical stoichiometry of their parent compounds: 1111 for RFeAsO(R: rare earth), 122 for AFe_2As_2(A: Ca, Sr, Ba), 11 for FeTe. The 1111 and 122 subsets are often called iron-pnictides as they have pnictogens (As, P). So far, the highest T_c of the Fe-based superconductor family is just above 50K as in $Gd_{1-x}Th_xFeAsO$ sample [38].

There are many common features between cuprates and Fe-based superconductors. First, both systems exhibit antiferromagnetic (AFM) order in their parent compounds as shown in Figure 1.5. Second, the building block of cuprates and Fe-based superconductors is a square lattice of cations, which is copper for the former and iron for the latter. Last but not least, both superconductors have layered structures composed of superconducting layers sandwiched between blocking layers. It is known that low dimensionality induced by doping the parent compound is favorable for superconductivity.

Meanwhile, there are several differences in the physical properties of these two unconventional superconductors. The Cu ions in the parent compound of cuprates have only one unpaired electron in $d_{x^2-y^2}$ orbital, and this electron hardly moves due to strong Coulomb repulsion, making the parent compound a Mott insulator. The antiferromagnetism in cuprates comes from these localized electrons. On the other hand, Fe ions in iron-based superconductors have at least two unpaired electrons, and band calculations suggest that all five 3d orbitals contribute to the density of state (DOS)

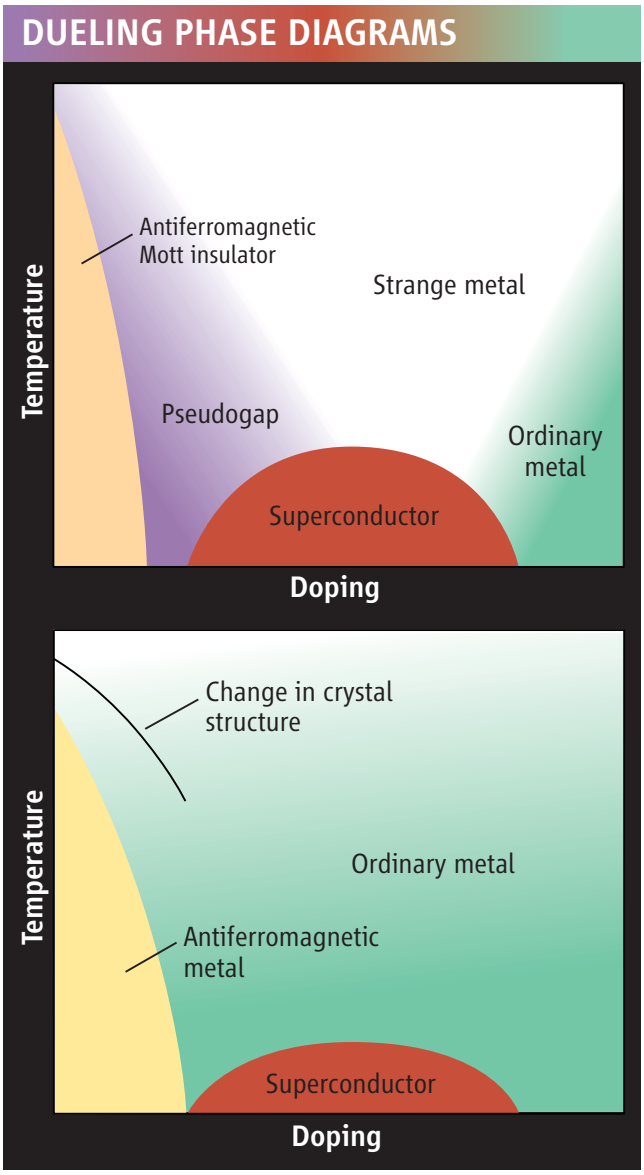

FIGURE 1.5: Typical phase diagram of cuprates (top) and Fe-based superconductors (bottom). The presence of SC dome near AFM phase in both systems suggests that magnetic fluctuations plays an important role in inducing superconductivity. This figure was taken from Reference [43].

near the Fermi surface. Both theoretically and experimentally, it has been proven that there is a strong Fermi Surface Nesting between the hole pocket and electron pocket in, at least, iron pnicitde. This nesting is known to lead to the Spin Density Wave instability of this system.

1.2.2 Possible pairing mechanisms in unconventional superconductors

There are two approaches to understand the unconventional superconductivity. The first approach is to consider the unconventional superconductivity as a completely novel mechanism different from BCS superconductivity. Here, superconductivity emerges from the Mott-Hubbard state. A well-known theory in this approach is the RVB (Resonant Valence Bond) model proposed by Philip Anderson. In his model, a novel phase of matter where spins are bound in singlet pairs resonating between different configuration will emerge upon doping the parent compound in an antiferromagnetic state. The charged resonating spin singlets will manifest themselves as a superconducting state.

Another approach is the spin fluctuation based model, which is currently the most commonly accepted scenario. In this approach, superconductivity emerges from a Fermi liquid, and it can be regarded as modified and extended BCS theory. It is well-known that the superconducting phase is always nearby the antiferromagnetic phase, and the magnetic exchange interaction is estimated to be strong in the unconventional superconductors. Even though static magnetic order compete with superconductivity, the magnetic fluctuations can be essential in mediating the unconventional SC pairs acting as a pairing 'glue'. Just as a charge polarization cloud from lattice fluctuations mediates the Cooper pairs in the conventional superconductors, a spin polarization cloud from spin fluctuations could also be responsible for the pairing of electrons in the unconventional superconductors.

Still today, the real mechanism of the high T_c superconductivity is under debate. Many other candidates for the microscopic mechanism were proposed such as orbital fluctuation [42] and charge fluctuation [40, 41]. In fact, any critical fluctuations from

a quantum critical point is believed to be able to mediate superconductivity [9, 10]. Especially in cuprates, there is much experimental evidence that supports the existence of a charge density wave near the superconducting phase dome [44] as shown in Figure 1.6.

For phonon mediated superconductors, the electron-ion interaction can be expanded in a controlled many-body perturbation series [11, 12]. On the other hand, for unconventional superconductors where the electron-electron interaction is important, it is not easy to employ such techniques, which prevents a rigorous description of unconventional superconductivity.

1.2.3 Pairing symmetries in unconventional superconductors

Because a pair of identical electrons have odd exchange symmetry, if the spin symmetry is odd (singlet), the the spatial symmetry must be even (eg. s-wave or d-wave); if the spin symmetry is even (triplet), then the spatial symmetry must be odd (eg. p-wave). The p-wave superconductor is particularly interesting in that it can support ferromagnetic fluctuations. However, the actual materials that shows the spin-triplet superconductivity are rare: $^{3+}$He and possibly Sr_2RuO_4 [15, 16].

The pairing symmetry of conventional phonon mediated superconductor is a simple s-wave. The pairing symmetry of unconventional superconductors can, however, vary according to the underlying physics including density, spin, and transverse current interactions [14]. The corresponding pairing symmetry is believed to be d-wave for cuprates, and $s^{\pm}$ for iron pnictides. It is believed that the simple s-wave symmetry is not favored for unconventional superconductivity because paired electrons would want to avoid close contact with each other, thereby reducing the effect of their mutual Coulomb repulsion.

Looking back on the BCS theory, there is no restriction that the mediating potential should be attractive from the equation,

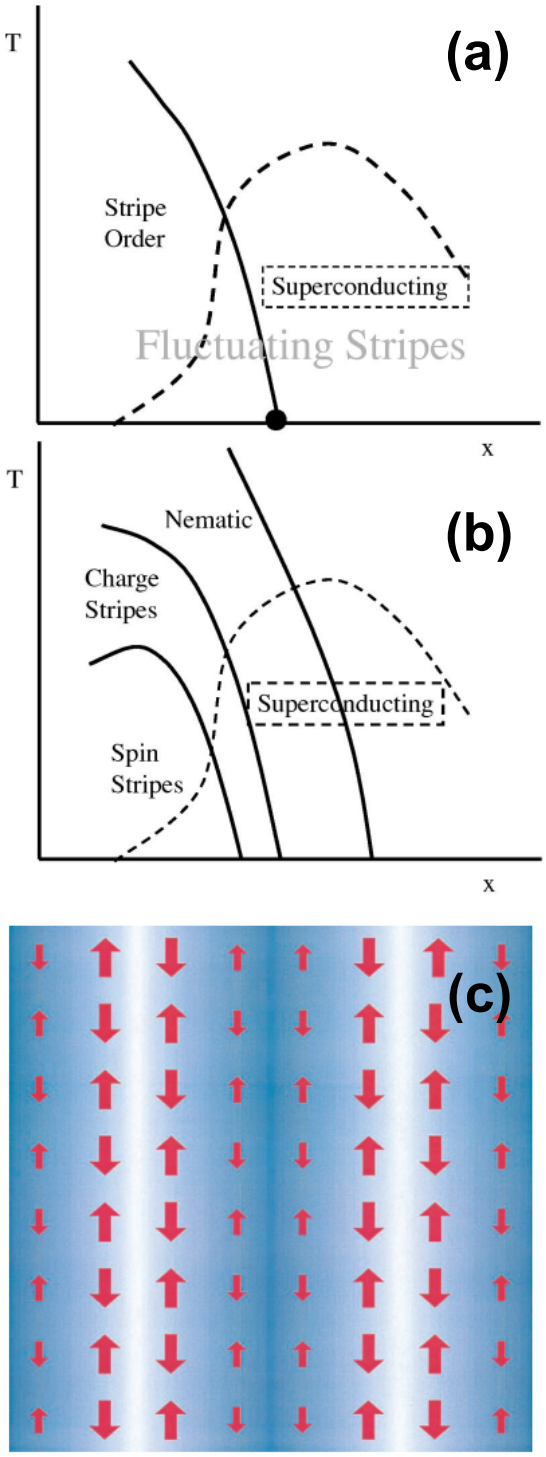

FIGURE 1.6: Schematic phase diagram showing various forms of stripe order and their interactions with high temperature superconductivity. (a) Stripe order competing with superconductivity. There is significant local stripe order in the region marked 'fluctuating stripes', which even extends beyond the ordered stripe phase. (b) More complicated version where other broken-symmetry phases are exhibited. The shape, topology, and even the number of ordered phases may vary for material-specific reasons. (c) Schematic picture of a stripe-ordered phase. The arrows represent the magnetic order and the blue scale represents the local charge density. These figures were taken from Reference [44].

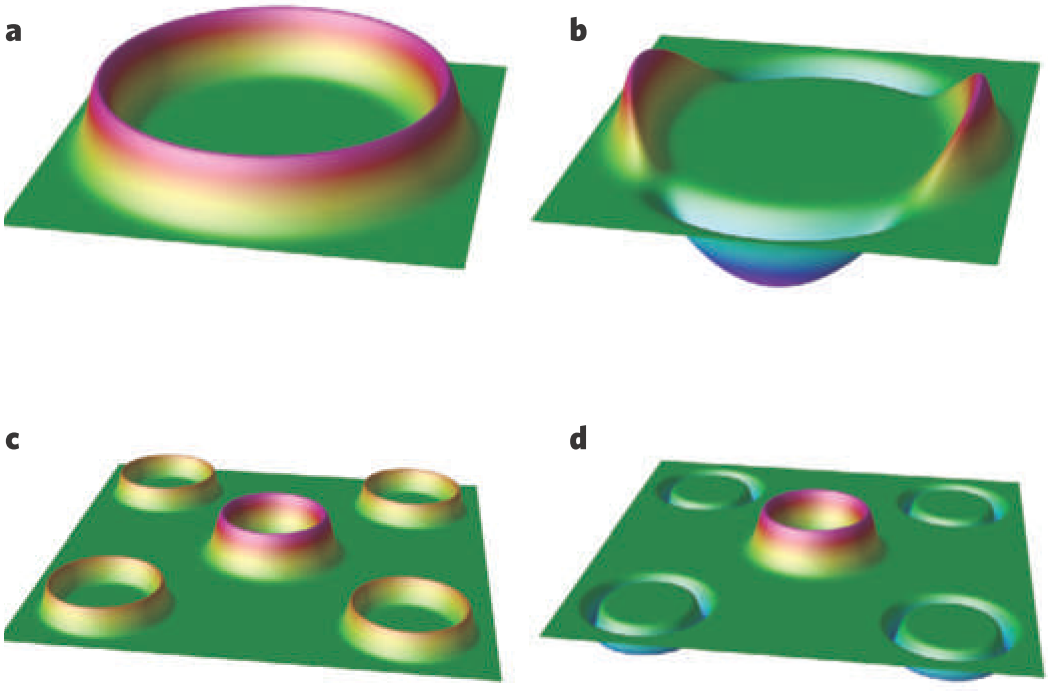

FIGURE 1.7: (a) a conventional, uniform, s-wave (b) a d-wave as in the case in cuprates (c) a two band s-wave with the same sign as in MgB_2 (d) $s^{\pm}$ wave suggested for Fe-pnictides. In all cases, the height of the 'rubber sheet' is proportional to the magnitude of the order parameter including its sign. These figures were taken from Reference [13].

$$\Delta_{\vec{k}\alpha} = \sum_{\vec{q}\beta} V_{\vec{k}\vec{q},\alpha\beta} \Delta_{\vec{q}\beta} \tag{1.6}$$

In this notation, positive V represent attractive interaction. If $\Delta_{\vec{k}\alpha}$ and $\Delta_{\vec{q}\beta}$ are of the same sign, V must be positive. However, if they are of the opposite sign, the corresponding V can be negative, which means repulsive interaction can pair electrons.

Charge fluctuations are always attractive regardless of pairing state, therefore pairs s-wave. On the other hand, spin fluctuations are repulsive in a singlet channel, and attractive in a triplet channel. Therefore, spin fluctuations can mediate the p-wave triplet pairing state, or a singlet pairing state, if that changes sign over the Fermi

surface, of d-wave or $s^{\pm}$ wave.

In magnetic fluctuation mediated superconductivity, therefore, it is important to have Fermi surface topology that matches the structure of magnetic excitations. In Figure 1.7, the Fermi structures for various superconductors are shown. For conventional phonon mediated superconductors, single-band or multi-band s-wave symmetries are found. For cuprates and iron-pnictides, on the other hand, the Fermi surfaces are connected with magnetic wave vectors, (π,0) and (π,π), respectively.

1.2.4 Crystal structure as a key factor

Whatever the underlying mechanism, it is always instructive to look at the relationship between superconductivity and crystal structure as superconductivity is an emergent phenomena coming from the strong correlation between different degrees of freedom. There are lots of debates as to what is the key factor inducing the high transition temperature superconductivity. In the case of iron-based superconductors, some argue that the anion height from the Fe-layer is closely related to the superconducting transition temperature [46]. Other people insist that the angle of $FeAn_4$(An: anion) tetrahedron is crucial for inducing high transition temperature [47], and the T_c becomes maximal at the angle of regular tetrahedron. (See Figure 1.8.)

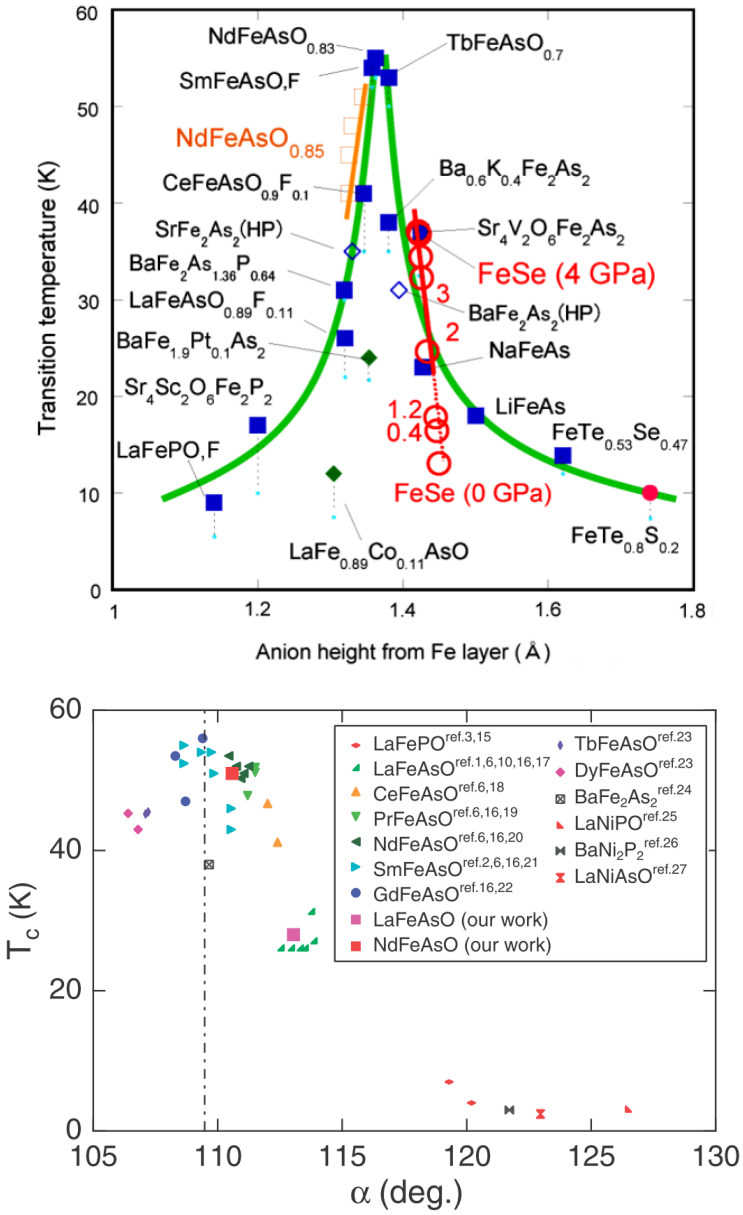

FIGURE 1.8: (top) Anion height dependence of T_c for typical Fe-based superconductors. Large symbols indicates the onset temperature. The zero resistivity temperature at ambient pressure are indicated by small light-blue circle. Filled diamonds indicate the data at ambient pressure. Open diamonds are the data of $SrFe_2As_2$ and $BaFe_2As_2$ under the optimal pressure. Open squares indicate the data of $NdFeAsO_{0.85}$. under high pressure (HP). The data of FeSe under high HP are indicated by open circles. A filled circle indicates the data of $FeTe_{0.8}Se_{0.2}$. Filled green diamonds are the data points for the Pt-doped $BaFe_2As_2$ and Co-doped LaFeAsO. (bottom) T_c versus As-Fe-As bond angle α for various pnictide superconductors. Formulas of parent compositions of superconductors are depicted in the inset. Crystal structure parameters of samples showing almost maximum T_c in each system are selected. The vertical dashed line indicates the bond angle of a regular tetrahedron where $\alpha = 109.47°$. These figures were taken from Reference [46, 47].

1.3 Introduction to BiS_2-based superconductors

Very recently, in 2012, new superconductors based on BiS_2 layer have been found [51]. After the discovery of $Bi_4O_4(SO_4)_{1-x}$ with transition temperature of 4.5 K, other members of this family were soon discovered: $LaO_{1-x}F_xBiS_2$ (Tc $\approx$ 10.6 K) [52], $NdO_{1-x}F_xBiS_2$ (Tc $\approx$ 5.6 K) [53], $PrO_{1-x}F_xBiS_2$ (Tc $\approx$ 5.5 K) [54], $CeO_{1-x}F_xBiS_2$ (Tc $\approx$ 3.0 K) [55].

1.3.1 Comparison with cuprates and Fe-based superconductors

These BiS_2-based superconductors are quite interesting in that they have layered structures just like cuprates and Fe-based superconductors, which is illustrated in Figure 1.9. Layered structure with low dimensionality tend to have stronger fluctuation which could be helpful for superconductivity pairing. In addition, the Bi ions form square lattice as Cu or Fe ions do. Band structure calculations find that the BiS_2 layer is responsible for superconductivity while there are blocking layers between the superconducting layers. Bi ions, however, are nonmagnetic, contrary to Cu or Fe ions in cuprates or Fe-based superconductors.

1.3.2 Possible pairing mechanisms suggested

After the discovery of the BiS_2-based superconductors, which share many common structural features with other unconventional superconductors, the natural question that arises is whether the newly found superconductors are just conventional BCS superconductors, or another family of non-BCS superconductors yielding a new route for unconventional superconductivity.

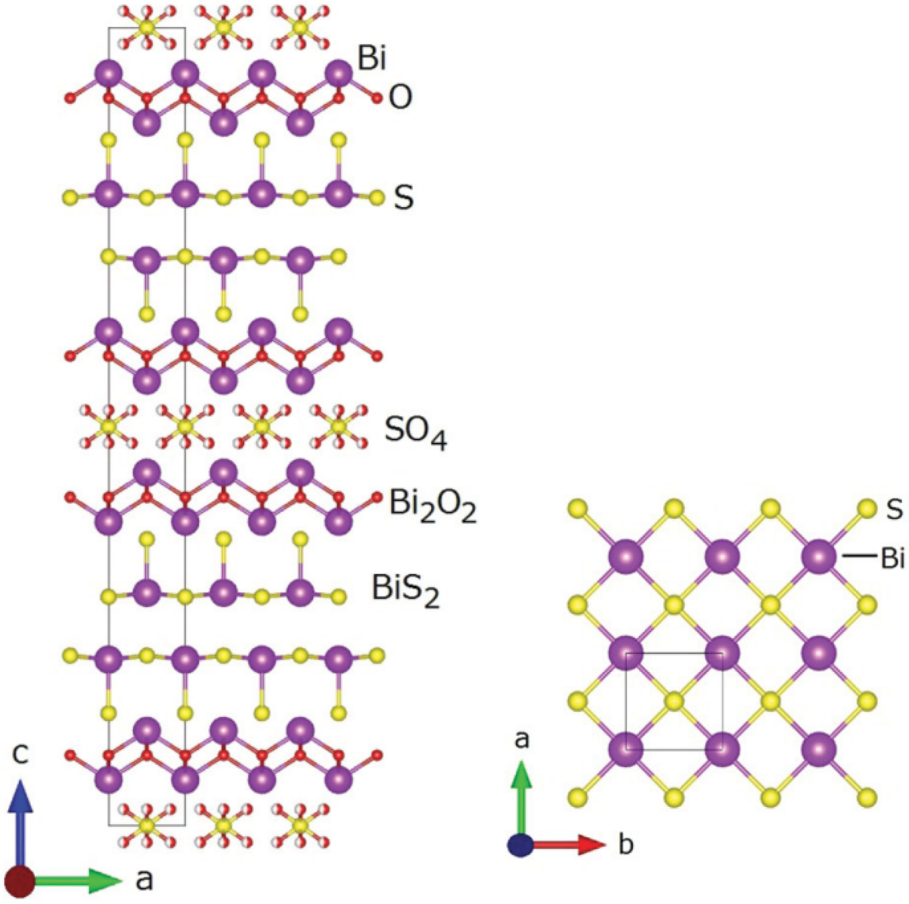

FIGURE 1.9: (left) Crystal structure of $Bi_4O_4S_3$, the first discovered superconducting sample in the BiS_2-based superconductor family. Purple, yellow, and red sphere indicate Bi, S, and O ions, respectively. The occupancy of O2 sites (the Oxygen in the SO_4 layers) is 0.5, hence their color are represented with half red and half white. (right) Schematic image of BiS_2 square lattice in the ab-plane which is common superconducting layer in the BiS_2 superconductor family. These figures are taken from Reference [51].

1.3.2.1 Electronic pairing mechanism

Several theoretical studies searching for possible pairing mechanism have been reported so far. According to the ab initio electronic structure calculation, around the optimal doping level there is a strong Fermi Surface Nesting at (π, π) just like Fe-based superconductors as shown in Figure 1.10) . This FSN can induce strong spin fluctuation which can act as a glue for the Cooper pair. The discovery of FSN

suggests that the pairing mechanism of the BiS_2-based superconductors can be electronic, making it a new type of unconventional superconductors.

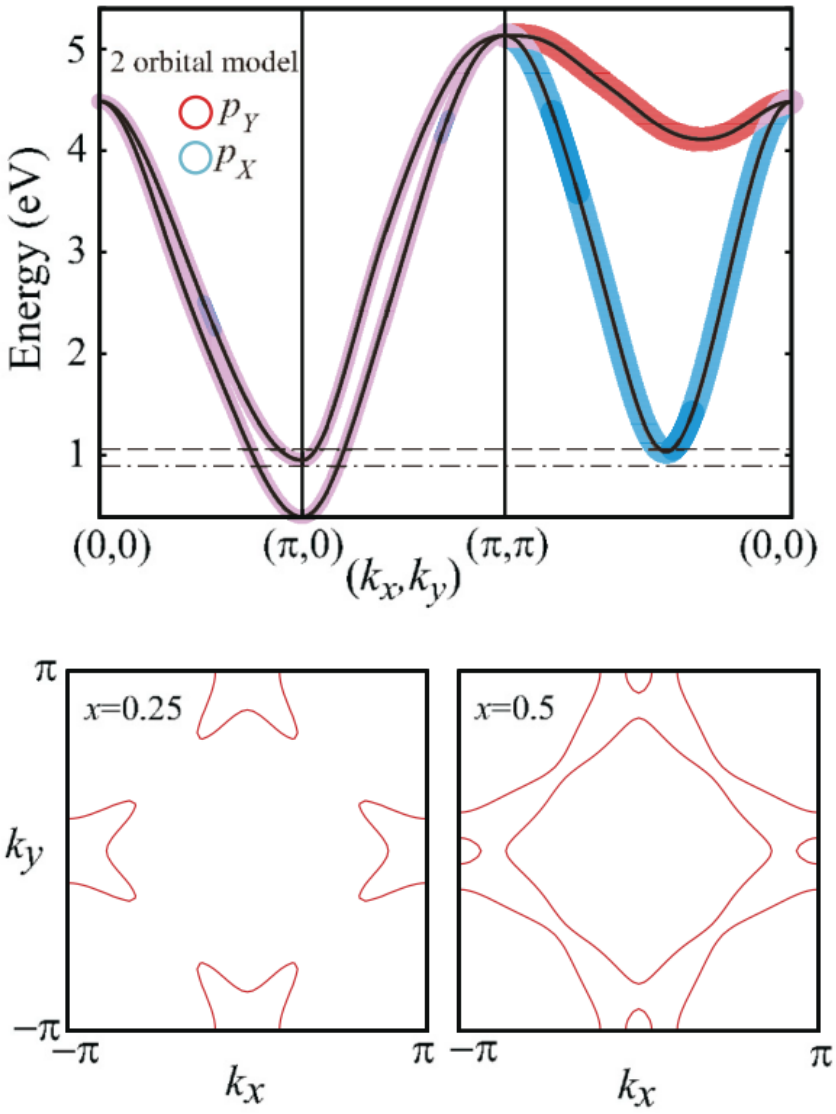

FIGURE 1.10: (top) The band structure calculated with two orbital model. The dashed lines denote the Fermi energy for the doping level of 0.5 and the dotted-dashed lines represent that for the doping level 0.25. (bottom) The Fermi surface of the two orbital model for the doping rate x of 0.25 and 0.5. These figures are taken from Reference [57].

1.3.2.2 Phononic pairing mechanism

On the other hand, other theorists find the electron-phonon coupling in this system can be strong enough to support the observed superconducting transition temperature. (See Figure 1.11 for the phonon dispersions and the electron-phonon coupling of $LaO_{0.5}F_{0.5}BiS_2$ estimated from ab-initio calculations.) This implies that the BiS_2-based superconductor can be a conventional superconductor with strong electron-phonon coupling just like MgB_2.

1.3.2.3 Charge density wave instability

It is quite interesting that phonon calculations predict unstable imaginary modes. All the phonon calculations up to now have been done for the $LaO_{1-x}F_xBiS_2$ sample with highest superconducting transition temperature. In the parent compound (x = 0), people found negative phonon modes at the zone center, Γ point. The ionic potential is shown in Figure 1.12, and the minimum energy position is not located at the equilibrium zero point. The potential well is, however, too shallow for the ion to be statically displaced. At the optimal doping level (x = 0.5), the phonon modes become unstable at the M point, (π, π), or along the line connecting the Γ and the M point. It should be noted that the M point is where the FSN occurs. The ionic potential for the optimally doped system is shown in Figure 1.13. In the doped sample, the potential is deep enough for the ion to be displaced to another equilibrium point, which could cause the static structural phase transition in this system. It has been suggested that the new structural space group can be P 2_1 m n (International Table number 31), and as you can see at the bottom the Figure 1.13, there could be a modulation in the position of ions, that is, charge density wave (CDW).

Therefore, it has been argued that the superconducting system is at, or in close proximity to the CDW phase. This CDW can compete with superconductivity, and its fluctuation can be responsible for the pairing mechanism.

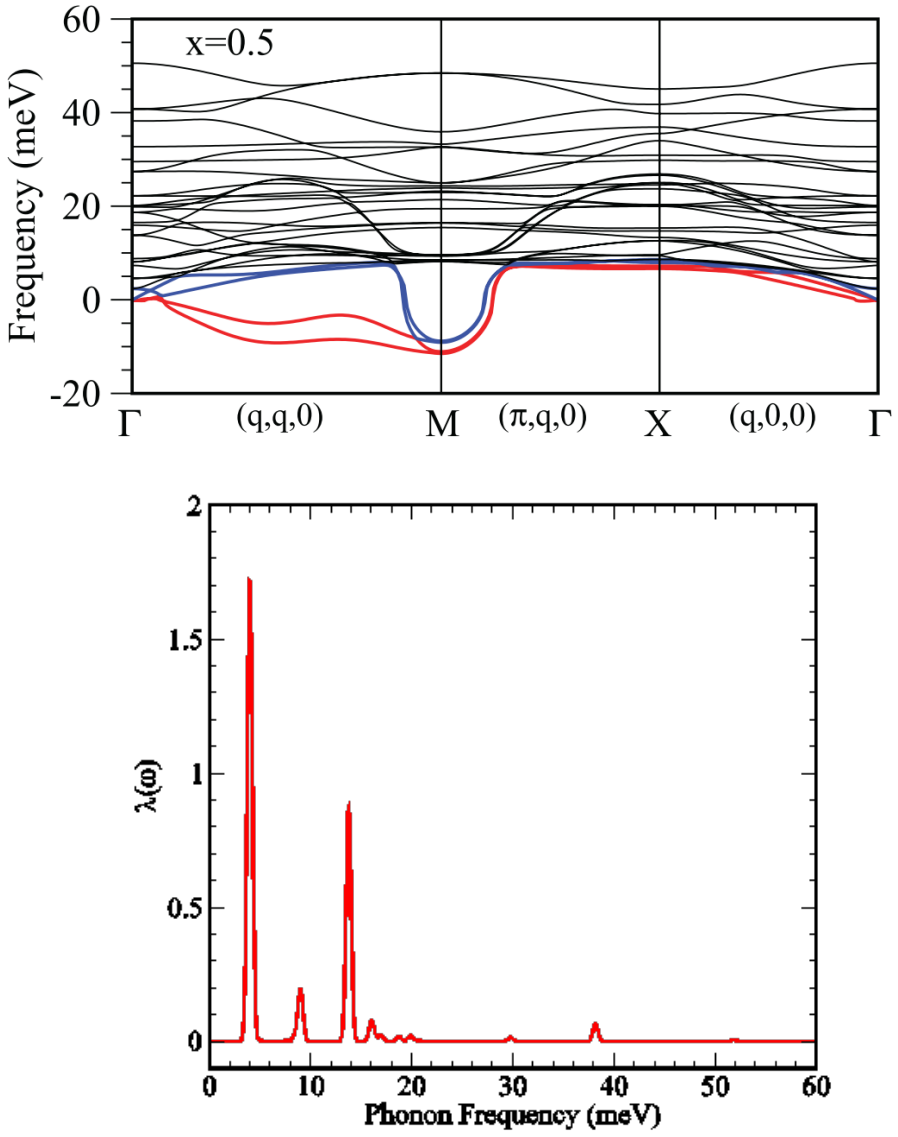

FIGURE 1.11: (top) Phonon dispersion curves for doping level x=0 ($LaOBiS_2$) and x=0.5 ($LaO_{0.5}F_{0.5}BiS_2$). This figure is taken from Reference [64]. (bottom) The electron-phonon coupling at zone center. There are four main peaks near 4meV, 9meV, 14meV, and 16meV.

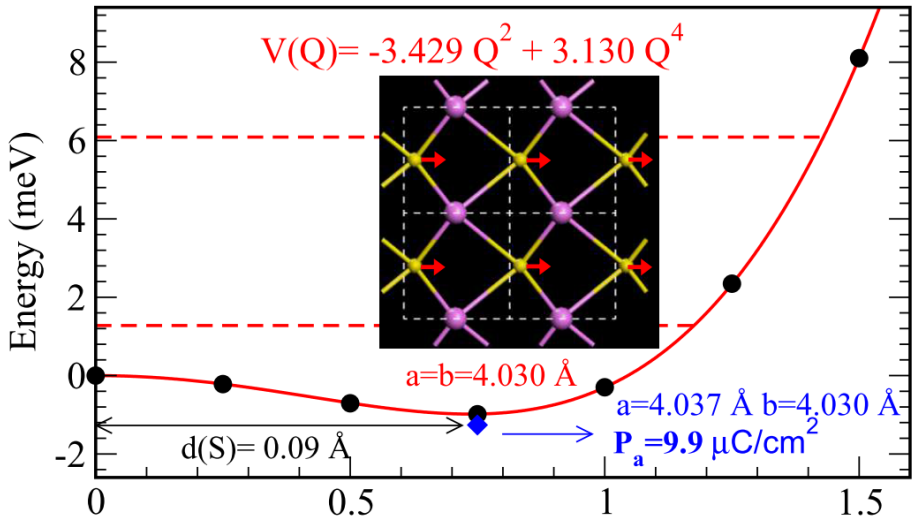

FIGURE 1.12: Total energy as the system is distorted by the most negative phonons at Γ in the $LaOBiS_2$. The frozen phonon potential is shown in the red curve, and the two lowest eigenstates. The lattice parameters of distorted orthorhombic structure, and the calculated polarization following the most negative phonon are indicated in the figure. The dispersion equation of the potential, and the minimum energy point from equilibrium is also noted. This figure is taken from Reference [64].

1.3.3 Theoretical relation between structure and superconductivity

As the structure of this system could be closely related with superconductivity, this relationship has been extensively investigated. It has been theoretically predicted that, upon doping the parent compound up to the optimal level, the a-axis lattice parameter increases a little bit, while the c-axis lattice parameter decreases substantially. Furthermore, if one pays attention to the atomic positions of BiS_2 layer, one can find the buckling of the plane decrease, and the plane becomes flat at x = 0.5 doping level. These structural changes as a function of F-doping are illustrated in Figure 1.14.

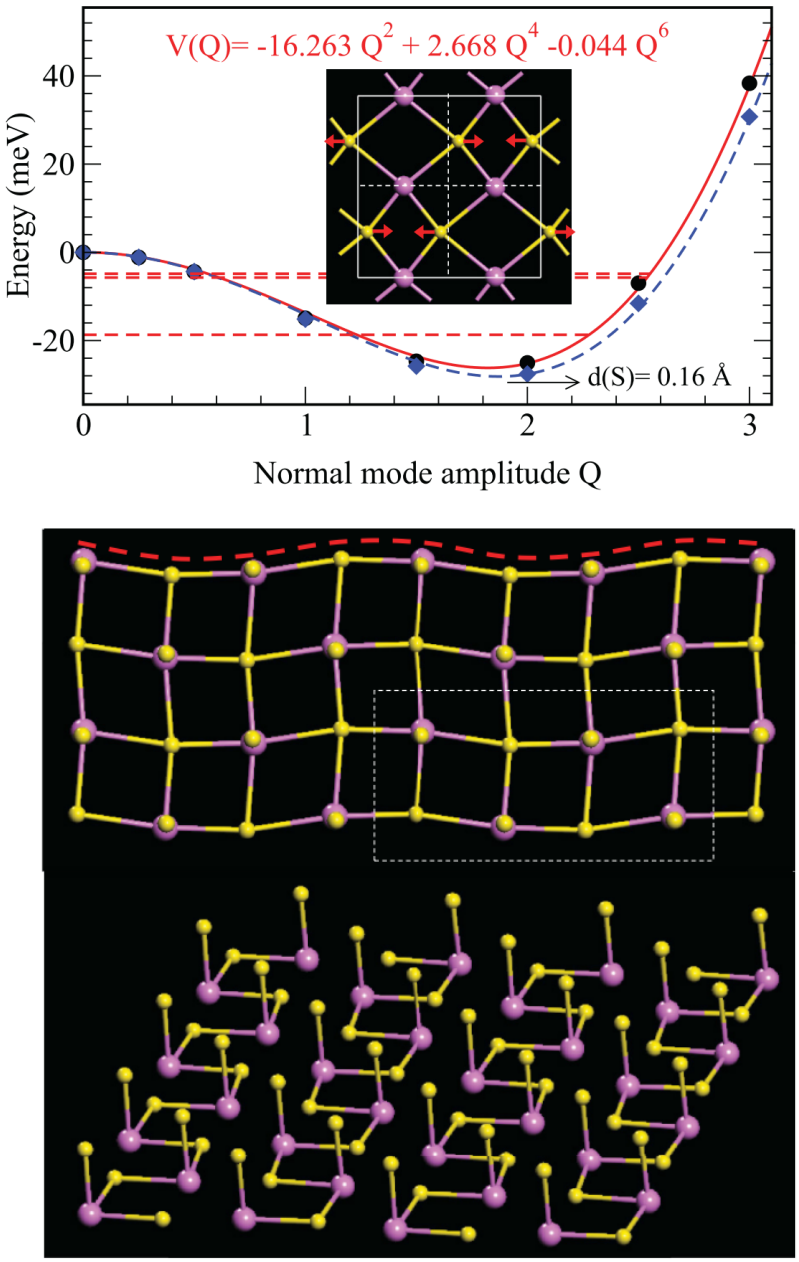

FIGURE 1.13: (top) Total energy as the system is distorted by the most negative energy phonons in the $\sqrt{2} \times \sqrt{2}$ cell of $LaO_{0.5}F_{0.5}BiS_2$ at Q = (π, π). The inset shows the sketch of the unstable phonons. The horizontal dashed red lines show the energy level of frozen-phonon potential (red curve). (bottom) The BiS_2 plane in a fully optimized CDW phase of $LaO_{0.5}F_{0.5}BiS_2$. Large pink and small yellow spheres are Bi and S ions, respectively. The dashed red line is a guide to eyes, indicating the sinusoidal distortion of the atoms. The white dashed square indicates the $\sqrt{2} \times \sqrt{2}$ unit cell of the CDW phase. The bottom panel shows the same structure with a Bi-S bond cutoff distance of 2.8 Å, where the one-dimensional nature of the chains becomes apparent. These figures are taken from Reference [64].

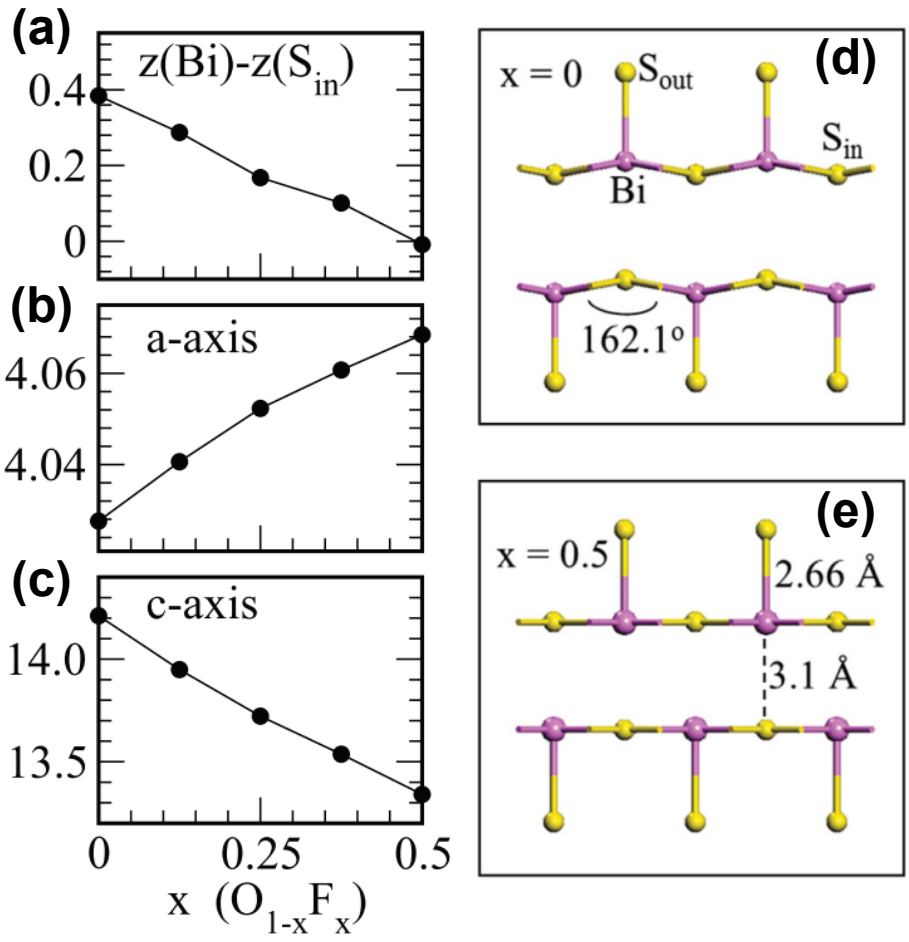

FIGURE 1.14: (left panels) Theoretically estimated crystal structural change as a function of Fluorine doping demonstrating (a) the difference of the z values of in-plane S ions (S_{in}) and Bi ions, (b) a-axis lattice parameter, and (c) c-axis lattice parameter. The y-axis are in the unit of Åin all cases. (right panels) Schematic side views diagram showing the expected change of BiS_2 bilayer buckling as the doping rate changes. (d) Zig-zag pattern when undoped (x = 0) and flat BiS_2 plane when the doping is optimal (x = 0.5). These figures are taken from Reference [64].

1.4 Thesis outline

We have briefly reviewed superconductivity in both conventional and unconventional forms. We covered the BCS theory based on phonon-mediated Cooper pairing, and also studied its failure in the unconventional superconductors such as cuprates and iron-based superconductors. In the unconventional superconductors, another kind of mediating interaction such as SDW or CDW is at play rather than lattice vibrations. To find out the critical factors that induce unconventional superconductivity, it is also instructive to look at the crystal structure. Recently discovered BiS_2-based superconductors will be studied in this regard with the help of neutron scattering techniques.

Theory on neutron scattering will be presented before investigating actual systems. We will study why the neutron scattering method is powerful, and what kind of sources and instruments are available for our purpose. Mathematical formulation of neutron scattering cross section for elastic/inelastic scattering from nucleus or magnetic ion will be discussed.

The La(O,F)BiS_2 system is the best sample to study the effect of phonon in the BiS_2-based superconductor family as it has the highest T_c and La is nonmagnetic without any magnetic ordering. The crystal structure, as a key factor related to superconductivity, will be investigated between the non-superconducting parent compound and the superconducting doped compound, and also between observed and theoretically calculated parameters. The generalized phonon density of states can be measured by neutron scattering to find out the role of phonon in this system. The GDOS between non-SC and SC compound are compared together with ab initio calculated ones. Finally, the change of GDOS as a function of temperature across the transition temperature is investigated.

$CeO_{0.3}F_{0.7}BiS_2$ shows a very rare and interesting case of coexistence of ferromagnetism and superconductivity. Its magnetic structures are examined at zero field and under an external field. Neutron powder diffraction simulation based on group theoretical

approach is used to find the possible magnetic structures, and field induced magnetic structure change is observed. The magnetic excitation is also investigated to understand the interactions of magnetic moment again with and without a magnetic field. By fitting the dispersion and intensity of neutron scattering, we can find its spin Hamiltonian is isotropic Heisenberg type with nearest and next nearest neighbor interactions.

Chapter 2

Introduction to Neutron Scattering

2.1 Theory of neutron scattering

2.1.1 Properties of neutrons as a probe for condensed matter

Neutron scattering is arguably one of the most powerful techniques to study condensed matter. In the neutron scattering technique, the sample of interest is radiated by a flow of neutrons. Then, from the scattered pattern of neutrons, we can infer either the internal structure of constituent atoms or the interactions between them. Especially for magnetism, neutron scattering is the most direct approach, and hence widely used to investigate magnetic structure and interactions. Furthermore, we can explore large energy and momentum space with relative ease. The power of neutron scattering lies in the physical properties of the neutron itself. Some of the properties of neutrons are summarized in Table 2.1.

Table 2.1: Physical properties of neutron

charge	0
spin	1/2
magnetic dipole moment	-1.913 μ_N
mass	1.675×10^{-27} kg

First, neutrons have zero net charge (which gives the name, "neutron"). Therefore, it can penetrate deeply inside a sample without being scattered by electrons. As a consequence, neutron scattering reflects bulk properties rather than surface effects. This property also serves well to study materials under different environment. It becomes relatively easy to accommodate cryogenic, vacuum, or magnetic field devices. More importantly, since neutrons are oblivious to the electron cloud, it directly interacts with nuclei of a material. While X-ray scattering cannot see light elements with few electrons such as Hydrogen or Oxygen, neutrons can easily index these elements which makes neutron more important in the study of fields like bio-materials, hydrogen storage materials, or high temperature superconductors.

Second, although the neutron's net charge is zero, its internal structure of quarks and gluons gives it a magnetic moment. Every electron also has a magnetic moment, therefore if there are unpaired electron spins in an atom, neutrons can interact with them via dipole-dipole interaction. The scattering length, a representative parameter for scattering strength, of a magnetic ion in neutron scattering is almost comparable to that of a nuclei. This makes neutron scattering a unique tool to study a material's magnetic properties.

Third, neutrons have relatively large mass. Consequently, hot neutrons with high kinetic energy generated from reactors can effectively be moderated by materials of comparable mass, such as water or liquid hydrogen. The moderated neutron has de Broglie wavelength of typical inter-atomic distance of a solid, making it suitable for diffraction. Moreover, the kinetic energy of moderated neutrons are usually of 0.1meV $\sim$ 100meV, and this is the order of many excitations in condensed matter like phonons or magnons, which render neutron scattering an excellent probe for excitations in a solid.

It should be noted, however, that the disadvantage of neutron scattering also comes from the same physical properties that make it so advantageous. Neutrons hardly interact with other materials that are essential to perform a neutron scattering experiment such as guide, sample, detector, etc. Neutron scattering scientists often

suffer from a lack of neutrons. A large amount of sample, high beam flux, well designed guide, enough amount of high efficiency-detectors are always desired. The large amount of neutron flux, however, is not always the best answer to a neutron scattering experiment as it may influence the data resolution. The optimal balance between the neutron flux and resolution is one of the key successes for a neutron scattering experiment.

2.1.2 Neutron sources

Neutron beams for scattering experiment are obtained from nuclear research reactors and spallation sources. From a reactor, neutrons are generated by spontaneous fission of ^{235}U. These neutrons are generated in a continuous manner. To gain a monochromatic energy beam of neutrons, Bragg reflection is employed using monochrometer materials like pyrolytic graphite, germanium, or copper. By changing the scattering angle at the monochrometer, we can control the wavelength, that is, the energy, of incident neutrons on the sample.

Spallation source neutrons are produced by bombarding heavy metal targets such as Hg, W, or Ta, with high energy proton packets accelerated in a magnetic field. These neutrons arrive as pulses, and usually, the time-averaged, moderated flux is less than that from a continuous reactor source. However, since the beams are pulsed in a spallation source, they are well suited for time-of-flight experiments. The beams are monochromated using several choppers rotating at different frequencies allowing only neutrons of specific velocity, or energy, to pass through.

2.1.3 Neutron scattering instrument

There are lots of neutron scattering instrument serving a variety of research fields with varying interests. Here I am going to describe the two most common neutron

scattering instruments for inelastic study: the triple-axis spectrometer and the time-of-flight spectrometer.

The triple-axis spectrometer, shown in Figure 2.1, gets its name because it utilizes three rotating axes: the monochrometer, the sample, and the analyzer. By controlling the angle of these axes, we can measure any point in energy and momentum space as long as it is allowed by the scattering geometry. The monochrometer angle defines the momentum and energy of incident beam; the sample angle chooses which reciprocal points are to be studied; and the analyzer angle selects the momentum and energy of the final scattered beam. Since the triple-axis spectrometer is installed with neutrons from a reactor source, it has high flux, and thus suitable for detailed study on a small region of ω -q space.

The time of flight spectrometer, shown in Figure 2.2, determines neutron energy by measuring its time-of-flight from one point to another. The energy of incident neutrons can be monochromated, as previously explained, by using several choppers. It is like a car moving at a specific speed can pass through all the blinking traffic lights without being stopped. Since we can select the neutron beam energy, we can predict when it hits the sample. Furthermore, since (1) we know the distance between the sample and detectors and (2) we can measure the time for neutron to fly from the sample to the detector, we can then calculate the energy of scattered neutrons. The direction of momentum transferred can be calculated from the detector angle. Time-of-flight spectrometers can be also installed in steady-state reactors if combined with pulsing choppers. The time-of-flight method is powerful because it can map out a huge ω -q space simultaneously generating a large amount of data.

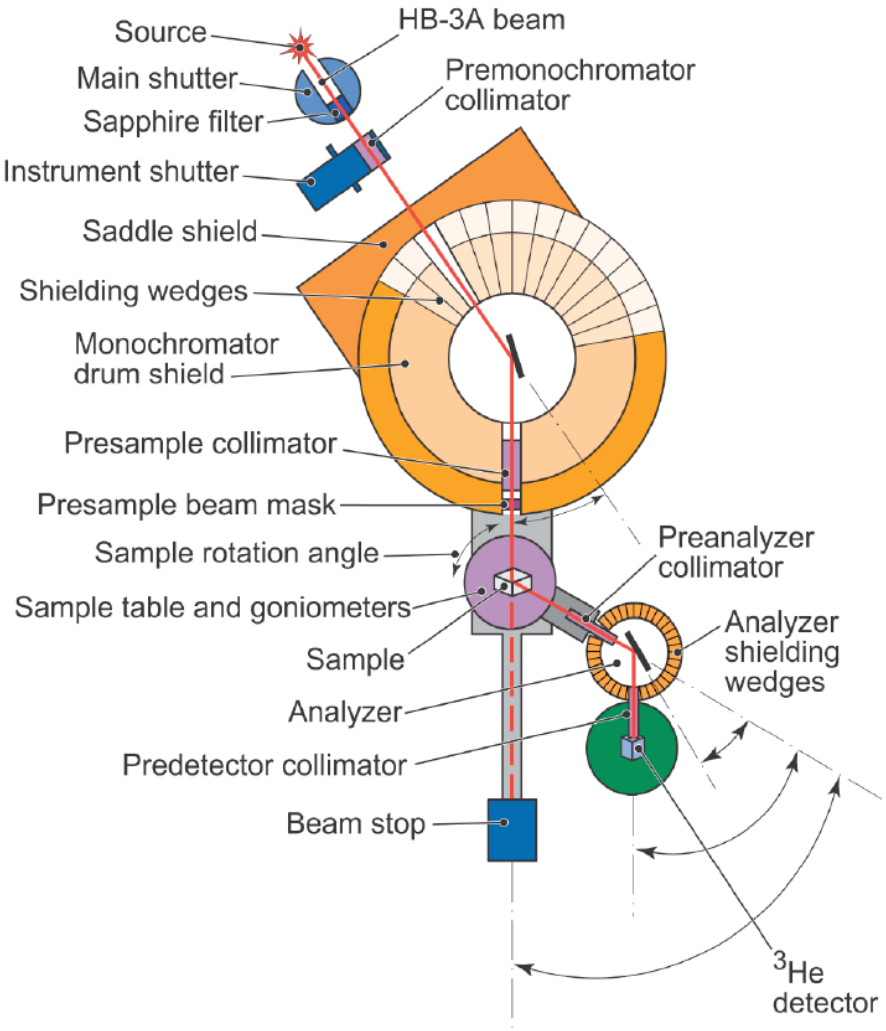

FIGURE 2.1: The schematic diagram of triple axis spectrometer at HB-3, High Flux Isotope Reactor, Oak Ridge National Laboratory. The name comes from the three rotating axes of monochrometer, sample table, and analyzer. One can explorer the energy-momentum space by changing the angle of these axes. Neutron beam from the source is reflected at monochrometer to have specific incident momentum and energy. Then, it is scattered from the sample, and the final momentum and energy is chosen by the analyzer. The double differential cross section, the number of neutrons scattered with specific momentum and energy, is measured by the ^{3}He detector. All shutters, shields, beam stops are to minimize the radiation in the background.

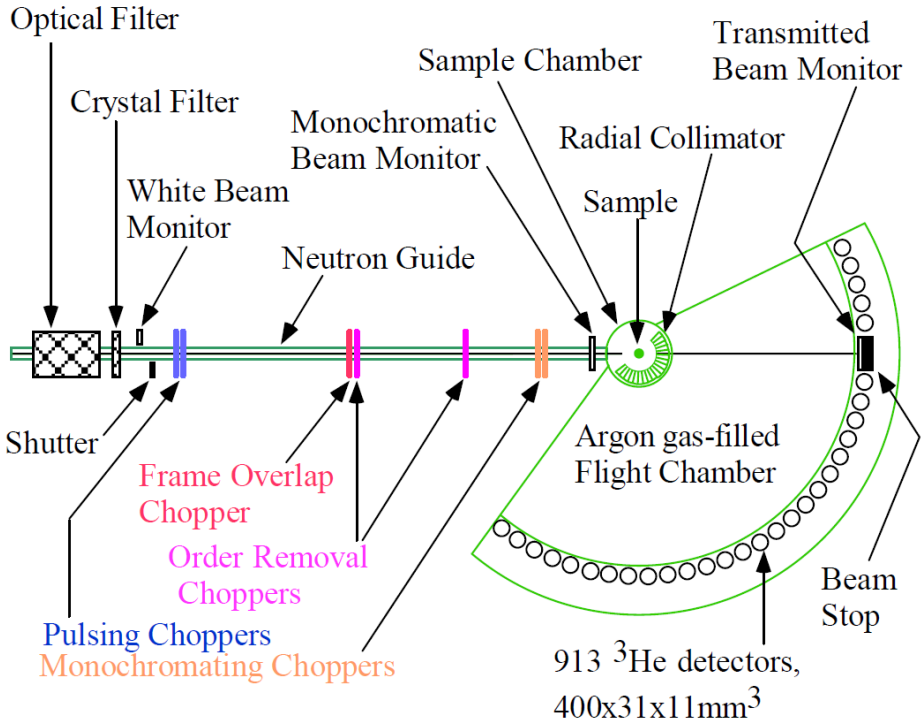

FIGURE 2.2: The schematic diagram of time of flight machine, DCS at Nist Center for Neutron Research, National Institute of Standard and Technology. The neutron beams from the source are monochromatized by the use of several choppers, and the momentum direction is almost parallel with the neutron guide. After the neutrons are scattered from the sample, the time of flight from the sample to the detector is measured electronically, which is converted to final energy of each neutron. 913 ^{3}He detectors are located in predefined position, so that we can figure out the angle of scattering, i,e, the final momentum of the neutron.

2.2 Mathematical formula for neutron scattering

2.2.1 Neutron scattering geometry

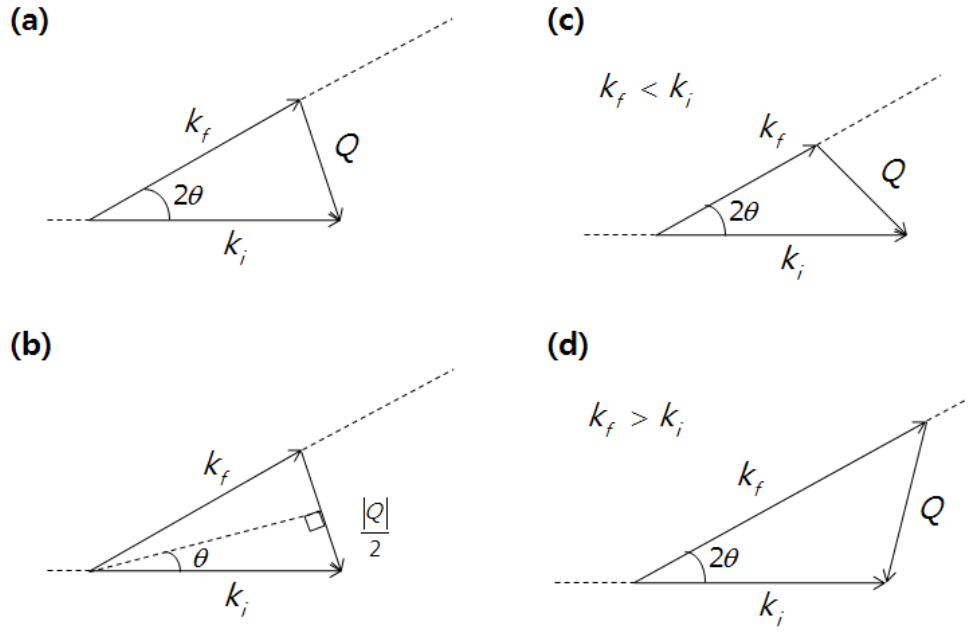

FIGURE 2.3: The scattering triangles composed of incident wave vector $\vec{k}_i$, scattered wave vectpr $\vec{k}_f$,and trasfered wave vector $\vec{Q}$. In case of elastic scattering where initial and final energy are equal, (a), the triangle becomes an isosceles, that is, $|\vec{k}_i| = |\vec{k}_f|$. We can see from (b), this condition gives special relation between $|\vec{k}|$ and $|\vec{Q}|$ that $Q = 4\pi sin\theta/\lambda$. When the scattering becomes inelastic, there is an energy transfer (c) from the neutron to the sample (neutron energy loss), or (d) vice versa (neutron energy gain). In the former case, $|\vec{k}_i| < |\vec{k}_f|$, and for the latter, $|\vec{k}_i| > |\vec{k}_f|$.

The two most important conservation laws in kinematics, "energy conservation" and "momentum conservation", should, of course, hold for neutron scatterings as well. Therefore, we obtain:

$$\vec{Q} = \vec{k_f} - \vec{k_i}$$
$$\hbar\omega = E_i - E_f \tag{2.1}$$

where $\vec{k}$ is the wave vector with magnitude k=$2\pi/\lambda$ (λ: wave length of neutron), E is the energy, and i and f subscripts are the initial and final state, respectively. Here, $\hbar\vec{Q}$ is the momentum transferred to the sample, and $\hbar\omega$ is the energy transfered ($\hbar$: Plank constant). The relation between momentum and energy is given by

$$E = \frac{\hbar^2 k^2}{2m_e} \tag{2.2}$$

where m_e is the mass of neutron. In the case of elastic scattering as in Figure 2.3 (a) and (b), by definition, there is no energy transfered to the sample, and the magnitude of wave vector, $\left|\vec{k}\right|$, does not change. On the other hand, when there is inelastic scattering as in 2.3 (c) and (d), the magnitude of the wave vector either increases when there is neutron energy loss or decreases in neutron energy gain.

2.2.2 Differential cross section

In neutron scattering, or in general, in every scattering experiment, we are interested in how many particles (neutrons, in our case) are scattered into a solid angle $d\Omega_f$ with energy range of E_f and $E_f + dE_f$ given the flux of incident particles $\phi(k_i)$ (see Figure 2.4), and this is called the differential cross section. When σ, the scattering cross section, represents the total scattering rate in every direction with all possible energies, the differential scattering cross section can be written as

$$\frac{d^2\sigma}{d\Omega_f dE_f}. \tag{2.3}$$

Neutron scattering can be considered as a weak perturbation causing a transition between states in the system while leaving the nature of the states themselves as they are. The proper equation describing this perturbation is Fermi's Golden Rule, and therefore, the differential scattering cross section can be represented as

$$\left.\frac{d^2\sigma}{d\Omega_f dE_f}\right|_{\lambda_i \to \lambda_f} = \frac{k_f}{k_i}\left(\frac{m_n}{2\pi\hbar^2}\right)^2 |\langle \vec{k_f}\lambda_f | V | \vec{k_i}\lambda_i \rangle|^2 \delta(\hbar\omega + E_i - E_f) \tag{2.4}$$

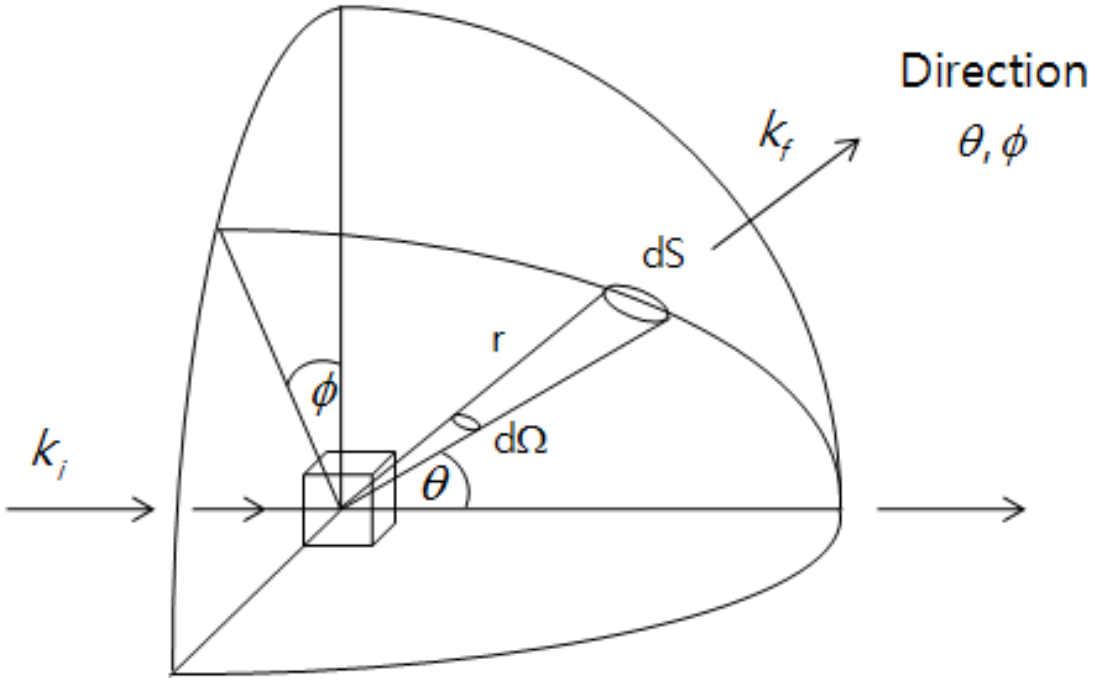

FIGURE 2.4: A neutron incident on a sample with the momentum of $\hbar k_i$. From the interaction between the sample and the neutron, the neutron is scattered in a specific direction in a spherical coordinate at the polar angle θ and the azimuthal angle ϕ with solid angle $d\Omega$. The momentum changes to $\hbar k_f$. The purpose of every scattering experiment is basically to measure the amount of scattering to a certain solid angle with specific energy and momentum.

where the initial and final state of sample are labeled by quantum number λ_i and λ_f. Since the interaction between the neutron and the sample is weak, we can further assume both incident and scattered wave functions as plane waves, i. e., the Born approximation. Under these assumptions, and using several mathematical techniques, it can be shown that

$$\frac{d^2\sigma}{d\Omega_f dE_f} = N\frac{k_f}{k_i}b^2 S(\vec{Q},\omega) \tag{2.5}$$

$$\begin{aligned} S(\vec{Q},\omega) &= \frac{1}{2\pi\hbar N}\sum_{ll'}\int_{-\infty}^{\infty} dt\langle e^{-i\vec{Q}\cdot\vec{r}_{l'}(0)}e^{i\vec{Q}\cdot\vec{r}_l(t)}\rangle e^{-i\omega t} \\ &= \frac{1}{2\pi\hbar N}\int_{-\infty}^{\infty} dt\langle\rho_{\vec{Q}}(0)\rho_{-\vec{Q}}(t)\rangle e^{-i\omega t}. \end{aligned} \tag{2.6}$$

Here,

$$\rho_{\vec{Q}}(t) = \sum_{l} e^{i\vec{Q}\cdot\vec{r}_l(t)} \tag{2.7}$$

is the atomic density operator, and the angle bracket means average over all possible states. Thus, the scattering function, $S(\vec{Q},\omega)$, is the Fourier transform of the time-dependent pair-correlation function. The scattering function only depends on $\vec{Q}$ and ω, not on the initial or final value of momentum or energy.

2.2.3 Coherent and incoherent scattering

Equation 2.5 can be rewritten to distinguish two kinds of scattering, coherent and incoherent, as

$$\begin{aligned} \frac{d^2\sigma}{d\Omega_f dE_f} &= N\frac{k_f}{k_i}(\bar{b})^2 S(\vec{Q},\omega) + N\frac{k_f}{k_i}\{(\bar{b^2}) - (\bar{b})^2\}S(\vec{Q},\omega) && (2.8)\\ &= N\frac{k_f}{k_i}\frac{\sigma_{coh}}{4\pi}S(\vec{Q},\omega) + N\frac{k_f}{k_i}\frac{\sigma_{inc}}{4\pi}S(\vec{Q},\omega). && (2.9) \end{aligned}$$

Here, $\sigma_{coh} = 4\pi(\bar{b})^2$ is the cross section for coherent scattering, and $\sigma_{inc} = 4\pi\{(\bar{b^2}) - (\bar{b})^2\}$ is for incoherent scattering. Due to isotopes, a monoatomic sample can have varying scattering lengths, and furthermore, even in an isotope, the scattering length can vary depending on relative spin direction between neutron and nuclei. These varying scattering lengths result in incoherent scattering. As is evident from the equation, coherent scattering is from the average scattering length, while incoherent scattering is from the variance of scattering lengths. In other words, the coherent scattering provides information about the cooperative phenomena among different atoms like Bragg scattering, phonons, or magnons, whereas the incoherent scattering gives information about individual particle motion, such as diffusion. In this dissertation, we will mainly focus on the coherent part of scattering.

2.2.4 Coherent nuclear scattering

2.2.4.1 Coherent nuclear elastic scattering

For coherent nuclear elastic scattering, we only consider the time averaged position, so that,

$$S(\vec{Q},\omega) = \delta(\hbar\omega)\frac{1}{N}\langle\sum_{ll'} e^{i\vec{Q}\cdot(\vec{r_l}-\vec{r_{l'}})}\rangle \tag{2.10}$$

$$= \delta(\hbar\omega)\frac{(2\pi)^3}{v_0}\sum_G \delta(\vec{Q}-\vec{G}). \tag{2.11}$$

Here $\vec{G}$ are reciprocal lattice vectors, and v_0 is the unit cell volume. We can generalize the above equation to non-Bravais lattice where there are more than one atom per unit cell. Furthermore, we can incorporate reduction of Bragg peak intensity due to thermal fluctuation of the atoms by using Debye-Waller factor. Then the equation becomes

$$\left.\frac{d\sigma}{d\Omega}\right|_{coh}^{el} = N\frac{(2\pi)^3}{v_0}\sum_G \delta(\vec{Q}-\vec{G})|F_N(\vec{G})|^2 \tag{2.12}$$

$$F_N(\vec{G}) = \sum_j \bar{b_j} e^{i\vec{G}\cdot\vec{d_j}} e^{-W_j} \tag{2.13}$$

where $\vec{d_j}$ is the position within the unit cell of the jth atom, and $W = \frac{1}{2}\langle(\vec{Q}\cdot\vec{u})^2\rangle$ for small displacement $\vec{u}$ of atom from its equilibrium position. $F_N(\vec{G})$ is called the static nuclear structure factor. It determines the relative intensity of Bragg peaks at different reciprocal sites, and hence, is used to find the position of atoms in a unit cell by fitting the experimental data.

2.2.4.2 Coherent nuclear inelastic scattering

First, let's start by mentioning some of the important properties of the scattering function. We begin with what is called the principle of detailed balance:

$$S(-\vec{Q},\omega) = e^{-\hbar\omega/k_BT} S(\vec{Q},\omega) \tag{2.14}$$

where k_B is the Boltzman constant, T is temperature, and $\hbar\omega$, the energy transfered, is assumed to be positive. This equation relates the probability of transition to depend on the weight factor of initial states, and results in higher intensity in the positive energy transfer region (excitation creation or neutron energy-loss region) than in the negative energy region (excitation annihilation or neutron energy-gain region).

Furthermore, from the fluctuation-dissipation theorem, $\chi''(\vec{Q},\omega)$,the imaginary part of dynamic susceptibility, that is, dissipation, can be related with the scattering function,

$$S(-\vec{Q},\omega) = \frac{\chi''(\vec{Q},\omega)}{1-e^{-\hbar\omega/k_BT}}. \tag{2.15}$$

This equation applies for both positive and negative ω. When the scattering function is an even function of Q, i.e.,$S(-\vec{Q},\omega) = S(\vec{Q},\omega)$, the principle of detailed balance requires $\chi''(\vec{Q},\omega)$ to be an odd function of ω, as can be shown below.

$$\frac{\chi''(\vec{Q},-\omega)}{1-e^{+\hbar\omega/k_BT}} = e^{-\hbar\omega/k_BT}\frac{\chi''(\vec{Q},\omega)}{1-e^{-\hbar\omega/k_BT}}$$

$$\chi''(\vec{Q},-\omega) = \frac{1-e^{+\hbar\omega/k_BT}}{1-e^{-\hbar\omega/k_BT}} e^{-\hbar\omega/k_BT}\chi''(\vec{Q},\omega) = -\chi''(\vec{Q},-\omega).$$

The coherent excitation of nuclei in a crystal is called a phonon. When there is n atoms in a unit cell, a total 3n mode of phonons should be expected with 3 dimensional degree of freedoms. When a neutron interacts with a single phonon, one obtains

$$\chi^{''} = \frac{1}{2}\frac{(2\pi)^3}{v_0}\sum_{\vec{G},\vec{q}}\delta(\vec{Q}-\vec{q}-\vec{G})\sum_{s}\frac{1}{\omega_{\vec{q}s}}|\mathfrak{F}(\vec{Q})|^2[\delta(\omega-\omega_{\vec{q}s})-\delta(\omega+\omega_{\vec{q}s})] \tag{2.16}$$

with $\mathfrak{F}(\vec{Q})$ being the dynamical structure factor given by

$$\mathfrak{F}(\vec{Q}) = \sum_{j}\frac{\bar{b}_j}{\sqrt{m_j}}(\vec{Q}\cdot\xi_{js})e^{i\vec{Q}\cdot\vec{d}_j}e^{-W_j}. \tag{2.17}$$

Here, q is the wave vector from the nearest reciprocal lattice, that is, $\vec{Q} = \vec{G} + \vec{q}$. $\omega_{\vec{q}s}$ is the frequency of phonon mode s at position $\vec{q}$, and ξ_{js} is the polarization vector of phonon mode s for the jth atom. Note that the minus sign in the above equation is required from the odd parity of $\chi^{''}(\vec{Q},\omega)$.

There can be various interactions which give rise to a finite lifetime for phonons, such as phonon-phonon or electron-phonon interactions. In the view of a phonon as a quantum single harmonic oscillator, this finite lifetime can be represented with damped harmonic oscillator model, making delta functions in energy space replaced with lorentzians. Therefore, the above equation, in this case, should be modified with a substitution of

$$\frac{1}{\omega_{\vec{q}s}}\delta(\omega\pm\omega_{\vec{q}s}) \rightarrow \frac{1}{\pi\omega'_{\vec{q}s}}\frac{\Gamma_{\vec{q}s}}{[\omega\pm\omega'_{\vec{q}s}]^2+\Gamma^2_{\vec{q}s}} \tag{2.18}$$

where, $\Gamma_{\vec{q}s}$ is the half-width at half-maximum(HWHM) of the peak, and $\omega'^2_{\vec{q}s} = \omega^2_{\vec{q}s} - \Gamma^2_{\vec{q}s}$.

2.2.5 Magnetic scattering

For an atom with spin S, the amplitude of magnetic scattering can be expressed as

$$pS = (\frac{\gamma r_0}{2})gf(\vec{Q})S \tag{2.19}$$

where γ is the gyromagnetic ratio, $r_0 = e^2/m_e c^2$ is the classical electron radius, g is Landé splitting factor, and $f(\vec{Q})$ is the magnetic form factor which is the Fourier transform of normalized unpaired spin density on an atom.

To determine the cross section of magnetic scattering, one needs to consider not only the initial and final state wave vector of the neutron, but also the spin state. If we account this in Equation 2.4, and solve for the unpolarized neutron case with a single species of magnetic atom, the differential cross section is given by

$$\frac{d^2\sigma}{d\Omega_f dE_f} = \frac{N}{\hbar}\frac{k_f}{k_i}p^2 e^{-2W}\sum_{\alpha,\beta}(\delta_{\alpha,\beta} - \hat{Q}_\alpha \hat{Q}_\beta)S^{\alpha\beta}(\vec{Q},\omega) \tag{2.20}$$

$$S^{\alpha,\beta}(\vec{Q},\omega) = \frac{1}{2\pi}\int_{-\infty}^{\infty} dt e^{-i\omega t}\sum_l e^{i\vec{Q}\cdot\vec{r}_l}\langle S_0^\alpha(0)S_l^\beta(t)\rangle \tag{2.21}$$

where $\alpha, \beta = x, y, z$ components. So, $S^{\alpha,\beta}(\vec{Q},\omega)$ is the Fourier transform of the time-dependent spin component α and β correlation function, analogous to equation 2.6.

It should also be noted that if we integrate $S^{\alpha,\beta}(\vec{Q},\omega)$ over all energies and over a Brillouin zone, the sum rule is obtained.

$$\int_{-\infty}^{\infty} d\omega \int_{BZ} d\vec{Q} S^{\alpha\beta}(\vec{Q},\omega) = \frac{(2\pi^3)}{3v_0}S(S+1)\delta_{\alpha\beta}. \tag{2.22}$$

As will be shown below, the elastic magnetic Bragg scattering is proportional to the square of $\langle S\rangle$, the ordered moment of spin, which is close to S in a classical spin system at low temperature. Thus, from the sum rule, the amount of summed spectral weight available for magnetic excitation is proportional to S.

2.2.5.1 Coherent magnetic elastic scattering

The cross section of coherent elastic scattering from a magnetic moment is given by

$$\left.\frac{d\sigma}{d\Omega_f}\right|_{coh,mag}^{el} = N_M \frac{(2\pi)^3}{v_M} \sum_{\vec{G}_M} \delta(\vec{Q} - \vec{G}_M) |\vec{F}_M(\vec{G}_M)|^2 \tag{2.23}$$

$$\vec{F}_M(\vec{G}_M) = \sum_j p_j \vec{S}_{\perp j} e^{i\vec{G}_M \cdot \vec{d}_j} e^{W_j} \tag{2.24}$$

which is similar to equation 2.12. Here, the subscript M indicates magnetic, as N_M and v_M refers to the number of magnetic unit cells in a sample and the volume of a magnetic unit cell, respectively.

2.2.5.2 Coherent magnetic inelastic scattering

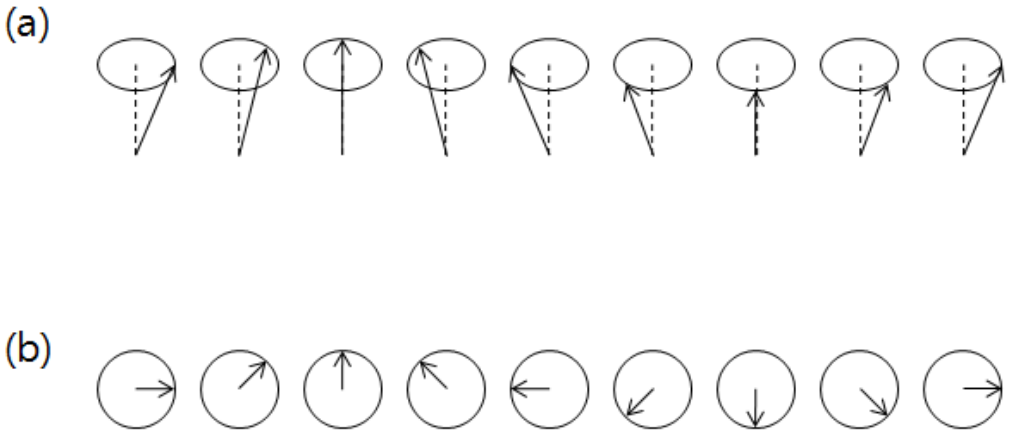

FIGURE 2.5: Classical picture of spin wave. (a) perspective and (b) top view of spin wave. It can be viewed as by propagating excitation in orthogonal direction to the average ordered moment.

Just as the collective excitations of nuclei in a solid which are called phonons, there can be collective excitations of magnetic moments (see Figure 2.5). These are called

spin-wave since, in a classical picture, the magnetic moments fluctuate like a propagating wave, and are also called magnons in the point of view from quasiparticle excitations. Spin wave involves displacements of the spins perpendicular to the average spin direction. If we assume the spins are ordered along z direction, for a single species of magnetic ion, we find that the magnetic double-differential cross section of the equation 2.20 can be modified by the following substitution.

$$\sum_{\alpha,\beta}(\delta_{\alpha,\beta}-\hat{Q}_{\alpha}\hat{Q}_{\beta})S^{\alpha\beta}(\vec{Q},\omega)=\frac{1}{2}(1+\hat{Q}_{z}^{2})S_{sw}(\vec{Q},\omega). \tag{2.25}$$

The inelastic scattering function for spin wave, $S_{sw}(\vec{Q},\omega)$, depends on the magnetic ordering pattern. For example, in the case of a Heisenberg ferromagnet with only nearest-neighbor interactions, it can be written as

$$S_{sw}(\vec{Q},\omega)=S\sum_{\vec{G},\vec{q}}[(n_{q}+1)\delta(\vec{Q}-\vec{q}-\vec{G})\delta(\omega-\omega_{q})+n_{q}\delta(\vec{Q}+\vec{q}-\vec{G})\delta(\omega+\omega_{q})]. \tag{2.26}$$

When we include the effect of damping, we can describe it by

$$\chi^{''}(\vec{Q},\omega)=S(\frac{\omega_{\vec{q}}}{\omega_{\vec{q}}^{'}})[\frac{\Gamma}{(\omega-\omega_{\vec{q}}^{'})^{2}+\Gamma^{2}}-\frac{\Gamma}{(\omega+\omega_{\vec{q}}^{'})^{2}+\Gamma^{2}}] \tag{2.27}$$

where

$$\omega_{\vec{q}}^{'}=\omega_{\vec{q}}-\Gamma^{2}. \tag{2.28}$$

Chapter 3

Crystal Structure, Phonon, and Superconductivity in La(O,F)BiS_2

3.1 Introduction

As discussed in Chapter 1, several families of superconducting (SC) materials and mechanisms have been found and proposed. The early discovered conventional superconductor was explained in BCS theory by mediating phonons, i.e., lattice vibrations. However, the newer unconventional superconductor has yet to be fully understood. Many of the materials that belong to the latter category have layered crystal structures with low dimensionality. The cuprates with CuO_2 layers and the Fe-based superconductors with Fe-An (An: pnictogen or chalcogen anion) layers are two extensively studied examples [48–50].

Very recently, a new family of materials based on BiS_2 layers has been found to be SC at low temperatures: $Bi_4O_4(SO_4)_{1-x}$ [51] and $LnO_{1-x}F_xBiS_2$ (Ln=La [52], Nd [53], Pr [54], Ce [55], and Yb [56]). The natural question that arises is whether the new Bi-based superconductors are conventional BCS superconductors or another family of non-BCS type superconductors yielding a new route for unconventional superconductivity.

Several theoretical studies have been reported especially for $LaO_{0.5}F_{0.5}BiS_2$ with currently the highest $T_c \approx 10.8$ K among the BiS_2-based superconductors. A recent band structure calculation [57] has shown the electronic bands near the Fermi surface are multi-bands with characteristics of mainly Bi-6p and S-3p orbitals. Without F-doping, there is an approximately 0.8 eV gap across the Fermi level, as shown in the Figure 3.1, making $LaOBiS_2$ a band insulator [57, 59–61]. Upon F substitution, the chemical potential increases to make the compound metallic for $T \geq T_c$ in a rigid band manner [60]. Because the conduction band is mainly from the p states of the BiS_2 layer, it is suggested that the BiS_2 layer is responsible for the superconductivity in these materials.

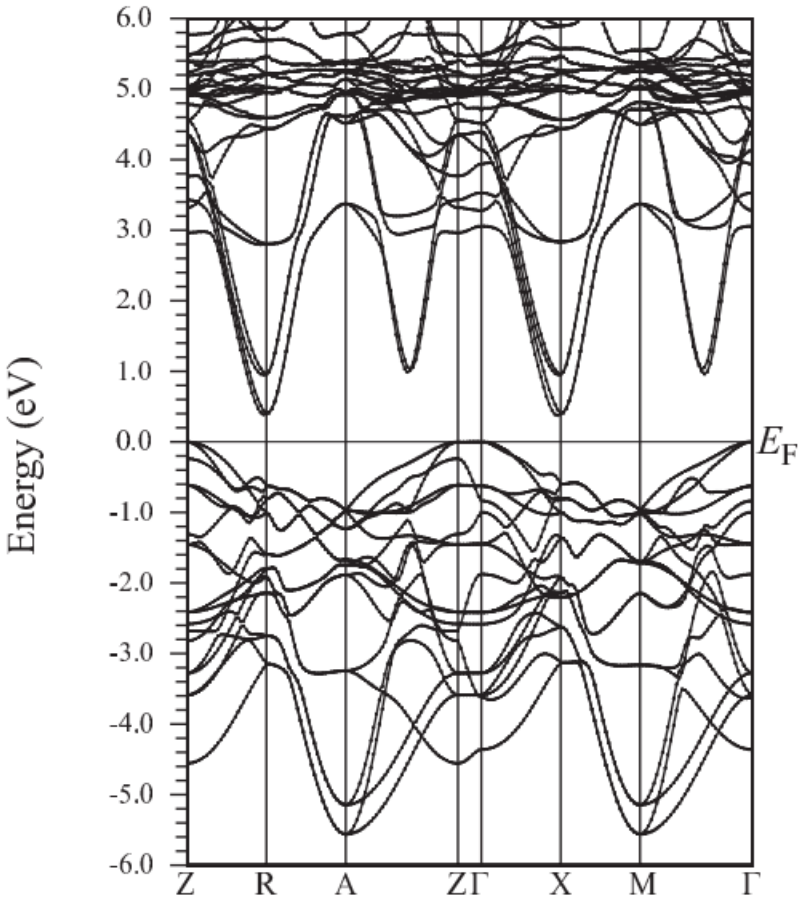

FIGURE 3.1: The first principle calculated band structure for. The panel is taken from the reference [57].

Calculations indicate the Fermi level in $LaO_{0.5}F_{0.5}BiS_2$ crosses four conduction bands

and results in only electron pockets [57, 59–61]. The quasi-one-dimensional (1d) nature of the conduction bands gives rise to a (π,π) wave vector Fermi surface nesting [57, 58, 60] just as in the Fe-pnictides. In addition, there are suggestions [66] that the SC pairing is much stronger than in the limit of the conventional phonon mediated picture, making electronic correlations a candidate for the pairing mechanism [58, 62]. Alternatively, an electron-phonon (e-ph) coupling constant calculation [60, 61, 64] finds $\lambda \approx 0.85$ with $T_c \approx 11.3$ K, close to the experimental value, when the Coulomb parameter of the Allen-Dynes formula is 0.1. This suggests $LaO_{1-x}F_xBiS_2$ is a conventional superconductor with strong e-ph coupling. Moreover, just like the spin-density wave (SDW) instability in Fe-based superconductors, a charge-density-wave (CDW) instability from negative phonon modes at or around the Γ point, (π,π), is suggested to be essential to the superconductivity [60, 64].

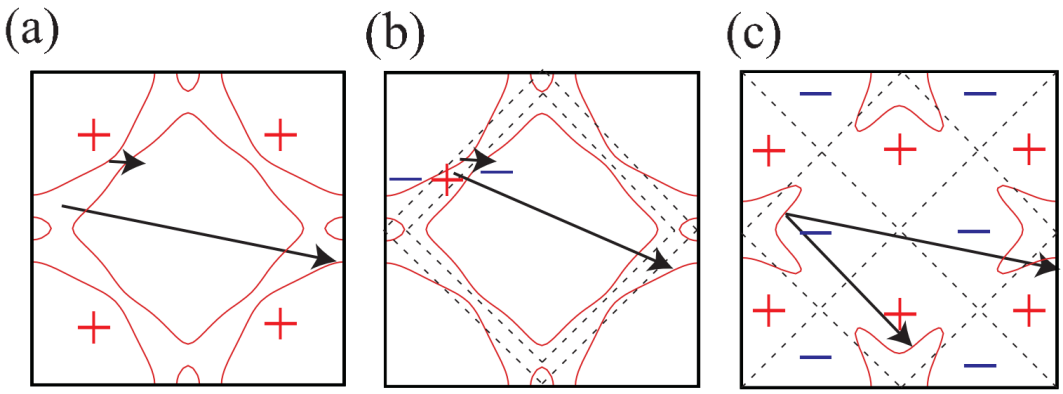

FIGURE 3.2: Schematic diagram of three types of pairing symmetries with spin fluctuation mediated spin singlet, and their nesting vectors (a) sign conserving s-wave, (b) sign reversing s-wave, and (c) d-wave superconducting gap

Several pairing symmetries have been proposed for superconductivity in the BiS_2-based superconducting materials [57, 58]: *s*-wave, sign reversing *s*-wave, and *d*-wave. It should be noted that since the Fermi surface is near a topological instability [52, 57, 68], the pairing mechanism can also change with substitution level. Considering the large extent of Bi-6*p* orbitals, the electron-electron (e-e) interaction may not be as strong, and the e-ph coupling can contribute to the sign reversing *s*-wave pairing enhanced by Fermi surface nesting and a large density of states near the optimal substitution. Alternatively, if e-e repulsion is not negligible but short-ranged, spin-fluctuations can mediate either $s\pm$-wave or *d*-wave pairing depending on the

substitution level and the intra/inter orbital interaction strength. Some examples of spin-fluctuation mediated pairings are shown in Figure 3.2. Finally, due to its quasi 1d band properties, spin-triplet pairing is also a candidate, as was suggested in Sr_2RuO_4 [69].

Experimental studies to test the theoretical scenarios, however, are limited: only some Hall effect and magnetoresistance measurements [66, 67] supporting the existence of electron pockets and multiband nature of this system have been reported so far. Thus, detailed experimental study of the crystal structure and lattice vibrations of non-SC and SC compounds, and its comparison with theoretical predictions are crucial in understanding the new BiS_2-based superconductors.

3.2 Methods

3.2.1 Experimental details

A 4.89 g polycrystalline sample of $LaOBiS_2$ was synthesized using the solid-state reaction method under ambient pressure while a 0.89 g polycrystalline sample of $LaO_{0.5}F_{0.5}BiS_2$ was synthesized under high pressure at the National Institute for Materials Science (NIMS) in Tsukuba, Japan. Details concerning sample synthesis are described in Refs. [52] and [65]. Figure 3.3 shows the low-temperature resistivity of the parent and the F-doped compound. $LaO_{0.5}F_{0.5}BiS_2$ exhibits a clear onset of SC transition at $T_c \approx 10.8$ K. Bulk superconductivity has been observed by a large diamagnetic signal below 8 K in the magnetic susceptibility measurement [52, 65]. Recent specific heat measurements also confirm that the superconductivity in this sample is bulk in nature [56].

Neutron scattering measurements were performed at the Spallation Neutron Source (SNS) using the POWGEN diffractometer, the wide angular range chopper spectrometer (ARCS), and the Cold Neutron Chopper Spectrometer (CNCS). Samples were loaded into vanadium (at POWGEN and CNCS) or aluminum (at ARCS) cans with a He atmosphere and mounted to the closed-cycle refrigerator (at POWGEN and ARCS) or liquid helium cryostat (at CNCS). Neutron diffraction data were collected using a wavelength band to cover a wide range of d spacing from 0.55 to 4.12 $\mathring{A}$ at POWGEN [70]. Inelastic neutron scattering (INS) measurements were performed at ARCS [71] with monochromatic neutrons of incident energies $E_i = 40$ and 80 meV. For improved resolution at low energy transfers, INS measurements were performed at CNCS [72] with $E_i = 25$ meV. All the INS data presented here are corrected for background by subtraction of an empty-can measurement.

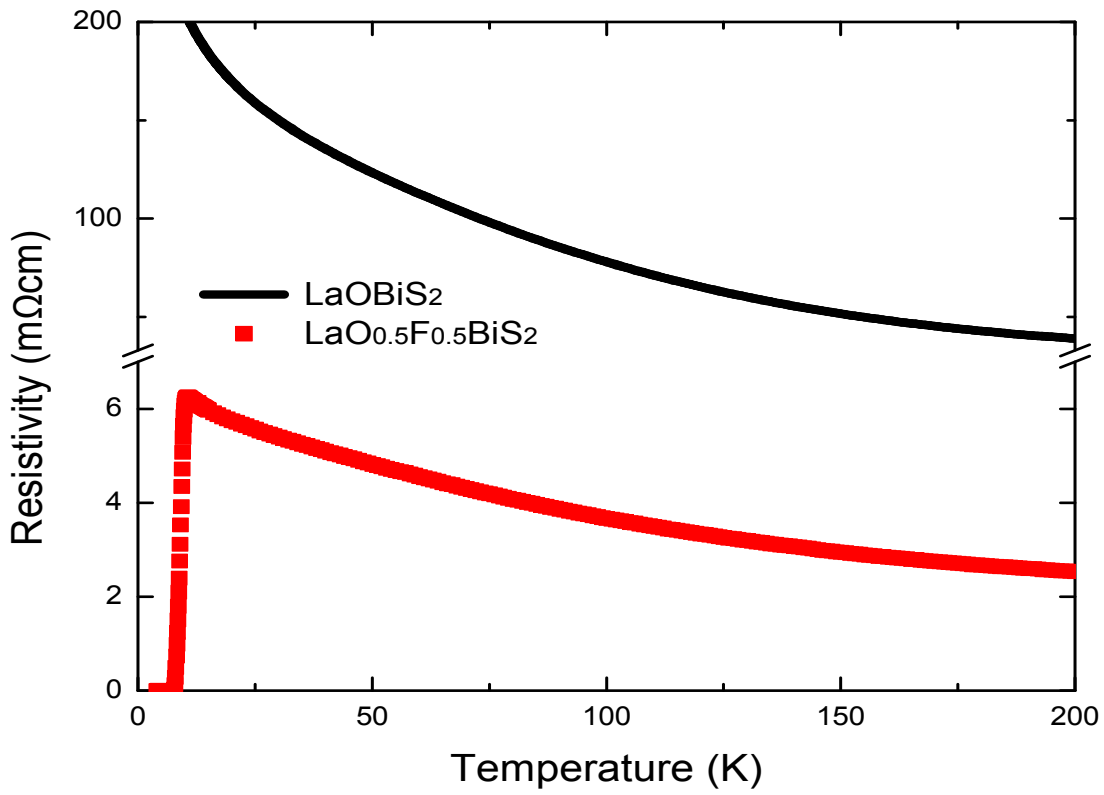

FIGURE 3.3: Temperature dependent resistivities of $LaOBiS_2$ (black lines) and $LaO_{0.5}F_{0.5}BiS_2$ (red squares).

3.2.2 Calculation details

The phonon calculations were performed using QUANTUM-ESPRESSO [73] with ultrasoft pseudopotentials. The generalized gradient approximation (GGA) of Perdew, Burke, and Ernzerhof [74] was used for the exchange correlation potential. A 20 x 20 x 6 regular grid over the irreducible Brillouin zone was used for the self-consistent calculation of the F-doped and parent compound. A plane-wave energy cutoff of 60 Ry and charge density energy cutoff of 480 Ry were used for both materials. A manual check of convergence for grid density, energy cutoff, and lattice parameter values was performed.

As we could find negative energy phonon modes at M = (π, π, 0), we double-checked our calculation with five different models. We list the phonon energies at M point to show that our calculations are well converged, confirming the existence of negative

energy modes at M.

To simulate the half doping in the SC sample, we replace oxygen at one of the 2a Wyckoff sites with F in an ordered fashion. In order to test the effect of the (O/F) ordering on the buckling of BiS_2 plane, we also repeated calculations using a system with charge doping without actual F substitution. We obtained similar results for both models.

We tested two models. In the first model, we approximate the F-doping by assuming a supercell structure of perfectly ordered O/F lattice. In the second model, we assume we have a perfect disorder of O/F and therefore the system can be simply modeled as a charged system without actual F-doping. The buckling of the BiS_2 plane from both models is shown in Figure 3.4. We note that both models give the same behavior, i.e. the buckling decreases with doping. In the ordered O/F model, the buckling vanishes completely at x=0.5 doping level while it is reduced down to 1 % for the charged-model with O/F disorder. This indicates the importance of the nature of F-doping in a real system.

The phonon DOS is calculated using the eigenvectors from the linear response calculations. The negative-energy modes are excluded in DOS calculations. However, due to very limited number of negative-energy modes, we do not expect significant contribution from them to the DOS. The powder-averaged phonon DOS is calculated using a 20 x 20 x 8 q-grid based on the linear response calculations of the dynamical matrix over a 4 x 4 x 2 grid.

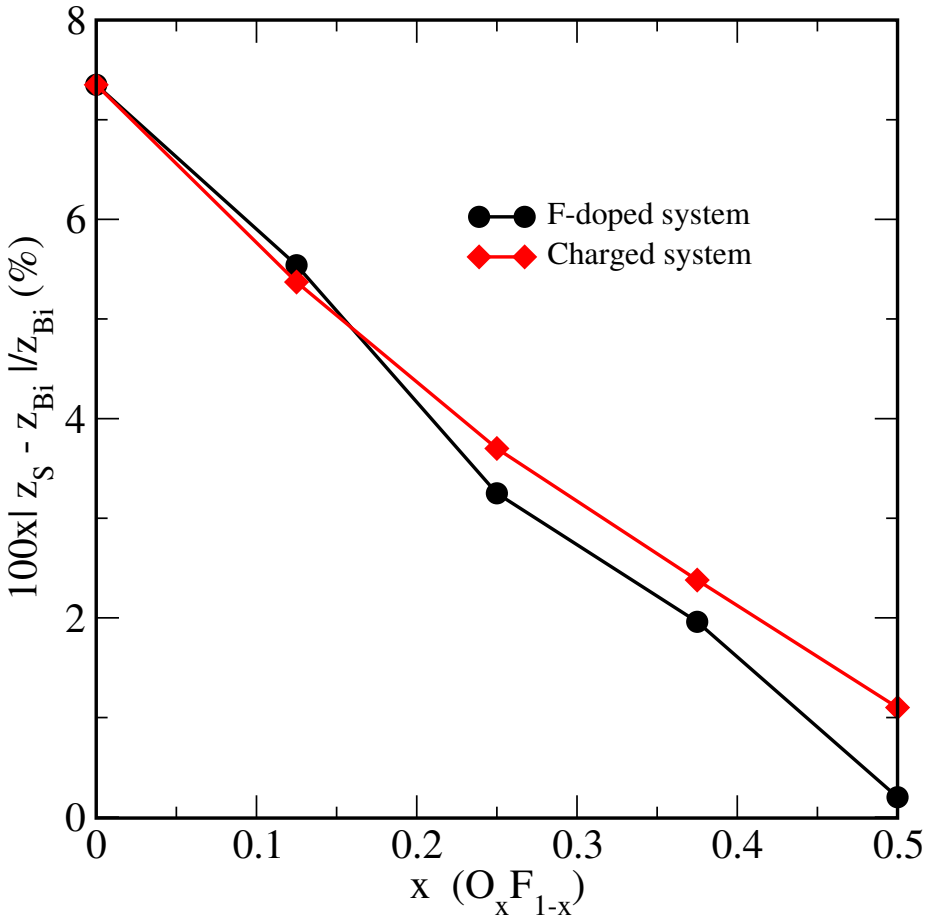

FIGURE 3.4: The buckling, defined as $|z_{Bi} - z_{S_1}|/z_{Bi}$, as a function of doping. The doping effect is modeled as an ordered structure of (F/O) (black line) and as a disordered model where the system is treated with a net charge and without actual F-doping (red line). We note that both doping models give similar trend that the buckling of the BiS_2 plane decreases with doping level approaching to 0.5.

3.3 Structure study

3.3.1 Neutron powder diffraction measurement

3.3.1.1 NPD and refinement of $LaOBiS_2$

The detailed crystal structure for the parent compound, $LaOBiS_2$, was first investigated in our report. Figure 3.5 (a) shows neutron diffraction data and Rietveld refinements obtained from this sample. The resolution of nuclear Bragg peaks are instrumentally limited, which indicates good crystallinity. The data for the parent compound is well reproduced by the $P4/nmm$ space group with structural parameters and goodness-of-the-fit listed in Table 3.1.

We determine the crystal structure, as shown in the Figure 3.6, to be similar to that found by the preliminary x-ray scattering measurements on the doped compound [52, 65]. The system has a layered structure where BiS_2 bilayers are well seperated by $La_2(O,F)_2$ blocking layers. The Bi ions form a square lattice just as the Cu and Fe ions do in the cuprates and Fe-based superconductors, respectively. There are two distinct Wyckoff sites for the sulfur ions, S_1 and S_2. While S_1 ions reside nearly on the same plane as the Bi square lattice with some buckling, the S_2 ions are just above or below the Bi ions.

3.3.1.2 NPD and refinement of $LaO_{0.5}F_{0.5}BiS_2$

In contrast, the SC $LaO_{0.5}F_{0.5}BiS_2$ has most of the nuclear Bragg peaks broader than our instrumental resolution (Figure 3.5 (b)), indicating imperfect crystallinity. Similar broadening has been reported in prior X-ray measurements [52, 65]. We note that the broad peaks have an asymmetric line-shape, characteristic of a low dimensional crystal ordering. The asymmetric broad peaks index with nonzero l values, while $l = 0$ Bragg peaks are considerably sharper and more symmetric. This is clearly seen in Figure 3.5 (b), for example, where the (200) peak at $d = 2.03$ Å and the (110)

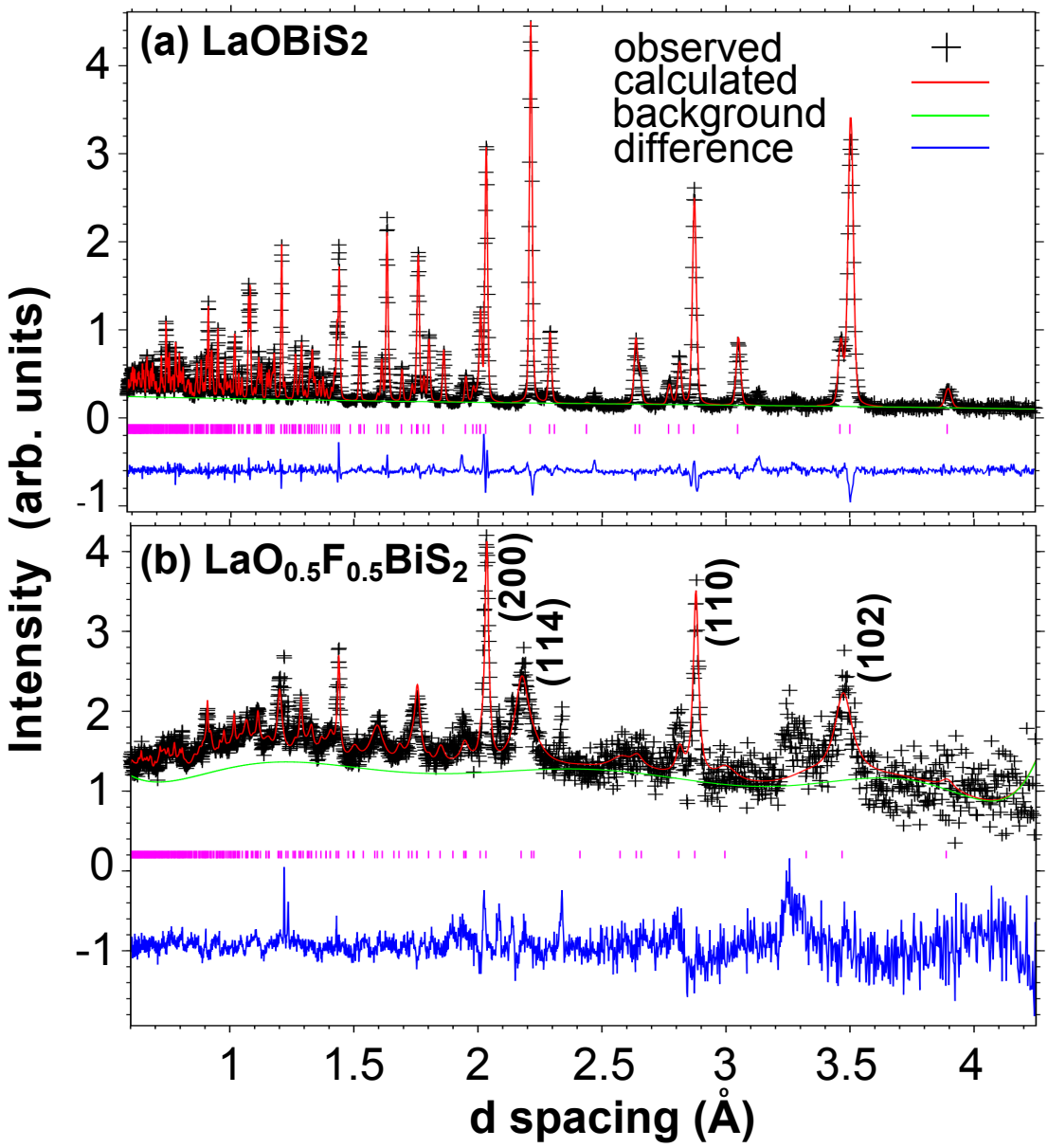

FIGURE 3.5: Neutron powder diffraction data obtained from (a) $LaOBiS_2$, and (b) $LaO_{0.5}F_{0.5}BiS_2$ at 15K. Black crosses represent observed data. Red, green, and blue solid lines are the calculated intensity, estimated background, and difference between the observed and calculated intensity obtained by GSAS [75], respectively.

	Experiment	Calculation
$LaOBiS_2$	Rwp = 0.074	
P4/nmm T=15K	$\chi^2 = 19.4$	
a (Å)	4.05735(5)	4.03949
c (Å)	13.8402(3)	14.30361
c/a	3.41114(8)	3.54095
La 2c (0.5, 0, z)	0.0907(1)	0.0853
Bi 2c (0, 0.5, z)	0.3688(1)	0.3665
S_1 2c (0.5, 0, z)	0.3836(3)	0.3949
S_2 2c (0.5, 0, z)	0.8101(2)	0.8112
O 2a (0, 0, 0)	–	–
$\lvert z_{Bi} - z_{S1} \rvert / z_{Bi}$	4.01(8) (%)	7.75 (%)
$LaO_{0.5}F_{0.5}BiS_2$	wRp = 0.065	
P4/nmm T=15K	$\chi^2 = 3.43$	
a (Å)	4.0651(3)	4.07989
c (Å)	13.293(7)	13.42520
c/a	3.2700(16)	3.2906
La 2c (0.5, 0, z)	0.1007(5)	0.1034
Bi 2c (0, 0.5, z)	0.3793(5)	0.3839
S_1 2c (0.5, 0, z)	0.362(2)	0.3840
S_2 2c (0.5, 0, z)	0.815(1)	0.8160
O 2a (0, 0, 0)	–	–
F 2a (0, 0, 0)	–	–
$\lvert z_{Bi} - z_{S1} \rvert / z_{Bi}$	4.5(5) (%)	0.0260 (%)

TABLE 3.1: Refined structural parameters of $LaOBiS_2$ and $LaO_{0.5}F_{0.5}BiS_2$ obtained from neutron powder diffraction and calculated with structural optimization implemented in QUANTUM ESPRESSO. The quantity $\lvert z_{Bi} - z_{S1} \rvert / z_{Bi}$ characterizes the amount of buckling. wRp and χ^2 respectively are the weighted R factor and chi squared values from the structural refinements [75]. Though there are some unindexed peaks in the refinement, the weight percentage of impurities is small based upon their relative intensities. Numbers in parentheses here and throughout the manuscript correspond to one standard deviation in the mean value.

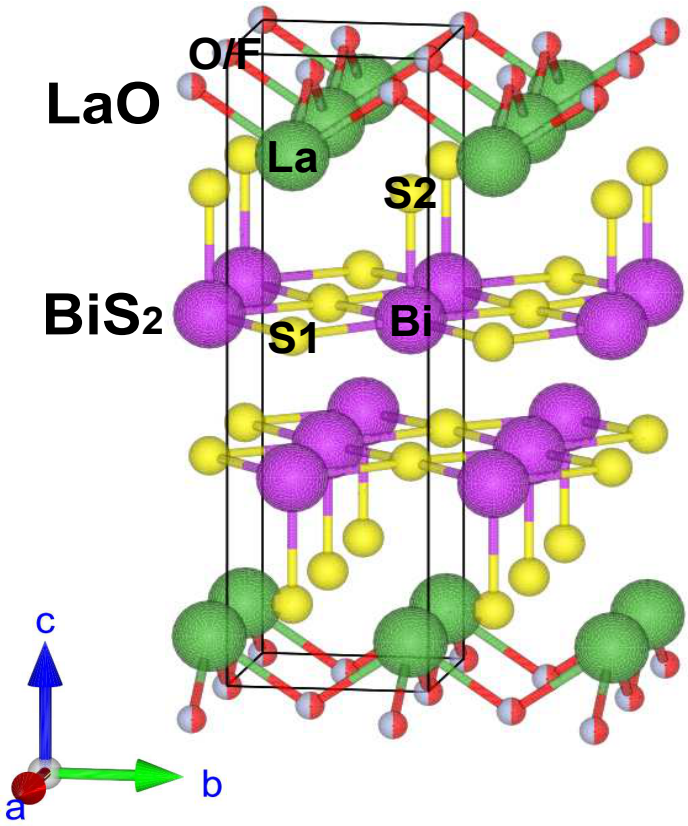

FIGURE 3.6: The crystal structure of $LaO_{1-x}F_xBiS_2$.

peak at $d = 2.87$ Å are sharp while the (114) peak at $d = 2.17$ Å and the (102) peak at $d = 3.47$ Å are broad and asymmetric. This suggests that strain may be induced along the c-axis due to a random replacement of the F ions at O sites. As a result, the La(O,F) planes are not well ordered along the c-axis.

S_{400}	S_{004}	S_{220}	S_{202}
5.767E+01	6.083E+00	4.025E+01	1.546E+02
(1.140E+01)	(1.642E+00)	(1.059E+01)	(1.036E+01)

TABLE 3.2: The anisotropic phenomenological strain parameter used to fit the diffraction pattern in the F substituted compound, $LaOFBiS_2$. The numbers in the parentheses represent estimated error.

The solid line in Figure 3.5(b) is our best refinement to the data, where a phenomenological model of anisotropic broadening has been used. This coarsely reproduces the diffraction data and allows for reasonable determination of the structural

parameters, summarized in Table 3.1. To describe the neutron diffraction pattern of $LaO_{0.5}F_{0.5}BiS_2z$, a phenomenological model of anisotropic broadening with multi-dimensional distribution of lattice metrics [76] has been used. In this model, the d spacing of Miller index is defined by

$$1/d^2 = M_{hkl} = \alpha_1 h^2 + \alpha_2 k^2 + \alpha_3 l^2 + \alpha_4 kl + \alpha_5 hl + \alpha_6 hk. \tag{3.1}$$

The local variance of the d-spacing, or M_{hkl}, can be related to the line broadening, and can be expressed as

$$\sigma(M_{hkl}) = \sum_{i,j} C_{i,j} \frac{\partial M}{\partial \alpha_i} \frac{\partial M}{\partial \alpha_j} = \sum_{HKL} S_{HKL} h^H k^K l^L \tag{3.2}$$

where $C_{i,j} = \langle (\alpha_i - \langle \alpha_i \rangle)(\alpha_j - \langle \alpha_j \rangle) \rangle$ is the covariance matrix of the Gaussian distribution, and S_{HKL} is defined for H+K+L=4. Given the tetragonal crystal system, the possible non zero anisotropic strain parameters are S_{400}=S_{040}, S_{202}=S_{002}, S_{004}, and S_{220}, whose refined parameters are summarized in the Table 3.2.

We also provide a more comprehensive characterization of the goodness-of-the-fit in the Table 3.3. Though the χ^2 and Rwp are smaller for the SC compound, it is mainly due to the poor data statistics of this sample. Smaller overall Rexp, and Bragg R-factors also support that these effects are coming from the smaller intensities and larger relative errors in the SC compound.

	χ^2	R_{wp}	R_{exp}	B-R_{wp}	B-R_{exp}
$LaOFBiS_2$	19.4	0.074	0.017	0.074	0.017
$LaO_0.5F_0.5BiS_2$	3.43	0.065	0.035	0.084	0.045

TABLE 3.3: The goodness of the fit for both samples. Rwp and Rexp follow the definition used in the GSAS [75] program, and B-R_{wp} and B-R_{exp} are R factors calculated for the Bragg peaks only.

3.3.2 Comparison of observed structure between non-SC and SC sample

We find upon F doping, the lattice elongates along a by approx. 0.2 % while it contracts along c by approx. 4.1 %, consistent with previous x-ray results [65]. This F-doping induced lattice change is reproduced by our calculations although the rates are different.

The buckling of the BiS_2 plane is found to slightly increase as shown in Table 3.1. This contradicts a prior theoretical prediction [64] as well as the structure optimization calculations presented here. The atomic positions in the superconducting sample, however, should be considered with care due to the large noise in the data. We note that although there is additional broadening in the superconducting sample diffraction data, the refinement converges to reliable values. Further work with additional or improved samples may be able to provide better accuracy.

3.3.3 Comparison of structure between observed and calculated

We were successful obtaining the optimized structure from the ab-initio calculation as well. The PWscf (Plane-Wave Self-Consistent Field) package in Quantum Espresso was employed for this purpose. PWscf performs many kinds of self-consistent calculations of electronic-structure properties within Density-Functional Theory (DFT), using Plane-Wave (PW) basis set and psuedopotentials (PP). We have tested the convergence of k-mesh size, energy cutoff, a-lattice parameter, and c-lattice parameter manually, and then relaxed atomic position. This manual process gave almost the same result with automated crystal structure optimization procedure, VCrelax. More information about the structural optimization can be found in Appendix B, or in the Quantum Espresso homepage.

We note that there are discrepancies between experimental and calculated structural parameters. First, there is a large difference in the interlayer distance: the optimized

interlayer distance is larger than the experimental one, especially in the parent compound. This becomes more clear if we compare the c/a ratio as in Table 3.1. We also observe in *both* compounds a large discrepancy in the z position of the S_1 atom between experimental and theoretical values. The discrepancy in the z position of the S_1 atom was regarded as a sign of a possible structural instability in this system [64]. This deviation seems to become larger with F doping. According to frozen phonon calculations, the instability at or near the M point can reduce the symmetry of the F doped compound statically to $P222_1$ [64], the CDW phase, or P -4 m 2 [61]. This potential structural transition, however, could not be experimentally confirmed due to the Bragg peak broadening.

3.3.4 Further discussion on the crystal structure and refinement

In summary, as Oxygen is substituted with Fluorine, the system becomes less crystalline, and a-axis lattice parameter decreases while c-axis lattice parameter increases. Some disagreements between the refined structure and the theoretically optimized one have been found: 1) the buckling in the BiS_2 plane remains almost the same contrary to expectation, 2) the c-axis lattice parameter is much smaller than expected, 3) the position of S_1 atoms is a lot different from what is predicted.

It is conceivable that these discrepancies are the result of extrinsic effects such as low sample quality. For example, the level of actual Fluorine doping could be different from the nominal one. Since we did not observe a significant decrease in the buckling of BiS_2 plane (and, as will be discussed in the GDOS section, also since the mode softening with doping is much smaller than calculated one), we can consider the actual F-doping level in our sample not complete and probably very inhomogeneous.

It is, however, also possible that these inconsistencies between theory and experiment are related with the inherent structural instability in this system, and the structure

is not at the lowest energy state expected for theoretically optimized crystal structure.

It should also be noted that during the NPD refinement, we observed unusually large thermal factor for the S_1 ions in both $LaOBiS_2$ and $LaO_{0.5}F_{0.5}BiS_2$, which is not explicitly reported here due to reliablity problems coming from impurities and broadening. Furthermore, it is very likely that this thermal motion is anisotropic, strong in the ab-plane. This possible anisotropic large thermal broadening suggests anharmonic potential of S_1 ions which is again related with structural instability in this system, consistent with the theoretical expectation. This, however, is hard to confirm due to large broadening of the Bragg peaks in the doped compound. This point should be re-investigated more carefully when high quality samples are available.

3.4 Phonon study

To examine if the pairing mechanism of the superconductivity is phononic, we have performed INS measurements to obtain the neutron weighted generalized PDOS (GDOS). Figure 3.7 shows the GDOS as a function of energy transfer, $\hbar\omega$, for the two compounds at $T = 5$ K.

3.4.1 Data processing to find GDOS

The background corrected neutron scattering intensity is directly proportional to the double differential cross-section which is directly proportional in turn to the scattering function, $S(Q, \omega)$,

$$\frac{d^2\sigma}{d\Omega d\omega} \propto \frac{k_f}{k_i} S(\vec{Q}, \omega) \tag{3.3}$$

where the k_i, and k_f are the incident and final neutron wave vectors. The scattering function for single phonon scattering in a polycrystalline sample can be written as,

$$S(Q, \omega) = \sum_i \sigma_i \frac{(\hbar Q)^2}{2m_i} exp(-2W_i) \frac{G_i(\omega)}{\omega} \langle n(\omega) + 1 \rangle \tag{3.4}$$

where $\hbar Q$, $\hbar\omega$, $n(\omega)$, σ_i, m_i, $exp(-2W_i)$ and $G_i(\omega)$ are the momentum transferred to the sample, the energy transferred, the Bose thermal factor at a given temperature, total scattering cross section, mass, Debye-Waller factor, and the phonon density of states for the i^{th} atom in the unit cell, respectively. The bare PDOS can be written mathematically as,

$$F(\omega) = \frac{1}{N} \sum_{j,\vec{q}} \delta \left[\omega - \omega \left(j, \vec{q}\right)\right] \tag{3.5}$$

where $\omega(j, \vec{q})$ is the frequencies of the phonon modes. We can see that the scattering function is related to the GDOS, $G(E)$, as, [77, 78]

$$G(E) = \sum_i \frac{\sigma_i}{2m_i} e^{-2W_i(Q)} F_i(\omega) / \sum_i \frac{\sigma_i}{2m_i} e^{-2W_i(Q)}. \tag{3.6}$$

The GDOS, therefore, reflects the PDOS while the intensity contribution from its components are weighted by σ_i/m_i, which are 0.07, 0.26, 0.21, 0.04, 0.03 barn/amu for La, O, F, Bi, and S, respectively. It is clear that the effect from oxygen and fluorine will be prominent in the GDOS measured by neutron scattering, and the GDOS will be weighted to the higher frequency compared with the bare PDOS. In general, however, the peak positions are not very sensitive to this neutron scattering weighting factor. The incoherent approximation requires the scattering function to be averaged over a wide range of wave vector transfer, Q, unless the scattering is purely incoherent so that the correlation between motions of distinct atoms cancels. For our measurement, the neutron scattering intensity was averaged over momentum of 3 $Å^{-1}$ to 6 $Å^{-1}$ for E_i = 25 meV, 4 $Å^{-1}$ to 7 $Å^{-1}$ for E_i = 40 meV, and 3 $Å^{-1}$ to 8.5 $Å^{-1}$ for E_i = 80 meV.

Since the above equation only applies for single phonon scattering, proper consideration of multiple scattering and multiphonon contributions is necessary. It is known that, in general, the correction from these factors produce only minor effects on the realistic PDOS, and in our case, constant background subtraction [79] was applied to remove linearly increasing GDOS intensity above the phonon cutoff energy. The contribution from elastic scattering has also been eliminated by removing the intensities below 2meV. The final GDOS has been normalized for the integrated area over the whole energy range to become unity for both samples.

3.4.2 GDOS measured

For the non-SC $LaOBiS_2$, (Fig. 3.7 (a)), there are well-defined phonon modes over a wide range of $\hbar\omega$ up to 70 meV. At least five prominent bands of lattice vibrations are present at 7.7(2), 14.2(1), 22.9(2), 40.4(1), and 61.8(4) meV. Upon F doping, as shown in Fig. 3.7 (b), the phonon modes at higher energies change significantly. All the vibrational modes become broader than their corresponding modes of $LaOBiS_2$. Furthermore, the top of the band softens in energy from 61.8(4) to 55.2(1) meV, and the sharp 40 meV peak significantly weakens. Conversely, the first two low energy peaks remain similar to those of the parent compound even though they broaden.

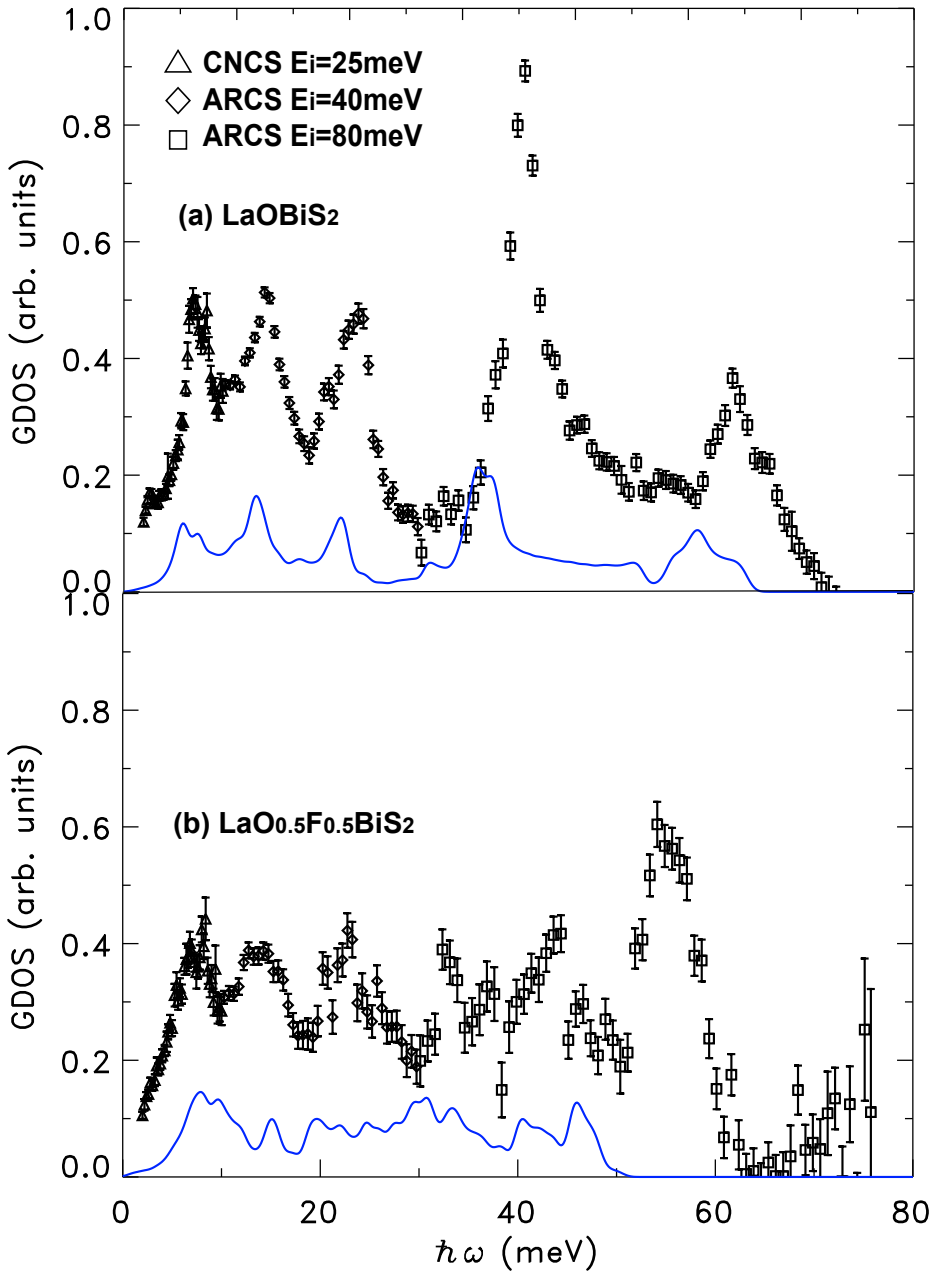

FIGURE 3.7: GDOS as a function of $\hbar\omega$ for the (a) parent non-SC and (b) F substituted SC compound. Black symbols are the experimental data; blue solid lines are the calculated GDOS scaled for comparison. Three measurements have been combined: below 10 meV are from CNCS E_i = 25 meV, between 10 and 30 meV from ARCS E_i = 40 meV, and above 30 meV from ARCS E_i = 80 meV. To obtain the GDOS, the neutron scattering intensities were averaged over momentum transfers of [3, 6] $Å^{-1}$, [4, 7] $Å^{-1}$, and [3, 8.5] $Å^{-1}$, respectively.

Several mechanisms can responsible for the broadening of GDOS upon F-doping. The first possible scenario is that as superconductivity is induced, the electron-phonon coupling gets stronger, which broadens the line-width of the phonon spectrum. This scenario is plausible for the phonon mediated superconductivity mechanism. Another possibility is that the broadening of the phonon spectrum is related with less crystalline nature of the superconducting sample. As the doped superconductor becomes more disordered compared to the parent compound judging from the broad Bragg peaks, it is quite natural to expect a broadened lattice vibration spectrum in $LaO_{0.5}F_{0.5}BiS_2$. Finally, it may just be that the phonon becomes more disperive when doped, which would appear as a broadening in the phonon spectrum. Single-crystal phonon spectrum study will help us decide which is the most important factor in the phonon broadening.

3.4.3 Calculated GDOS compared with experimental data

3.4.3.1 $LaOBiS_2$ case

Our calculated GDOS is shown as solid lines in Figure 3.7. For the non-SC sample, it reproduces the observed prominent phonon modes reasonably well. Our calculations at the zone center show that the 40 and 62 meV bands are mainly due to vibrations of light ions. For example, in the inset of Figure 3.8, the last 5 figures show the high energy vibration modes. These modes mostly involve O and/or S_2 vibrations. The intermediate energy modes around 13 and 23 meV are mainly due to S_1 and/or S_2 vibrations, while the low energy modes below $\approx$ 10 meV are due to the vibrations of BiS_2 and/or LaO layers. Our zone-center calculations also yield imaginary frequency, unstable phonon modes involving vibrations of the BiS_2 layer, which was previously reported as the sign of anharmonic ferroelectric soft phonons [64].

3.4.3.2 $LaO_{0.5}F_{0.5}BiS_2$ case

For the SC-sample, the calculated GDOS reproduces the features occurring at large $\hbar\omega$ (albeit shifted in energy), and these include: the broadening of high energy peaks,

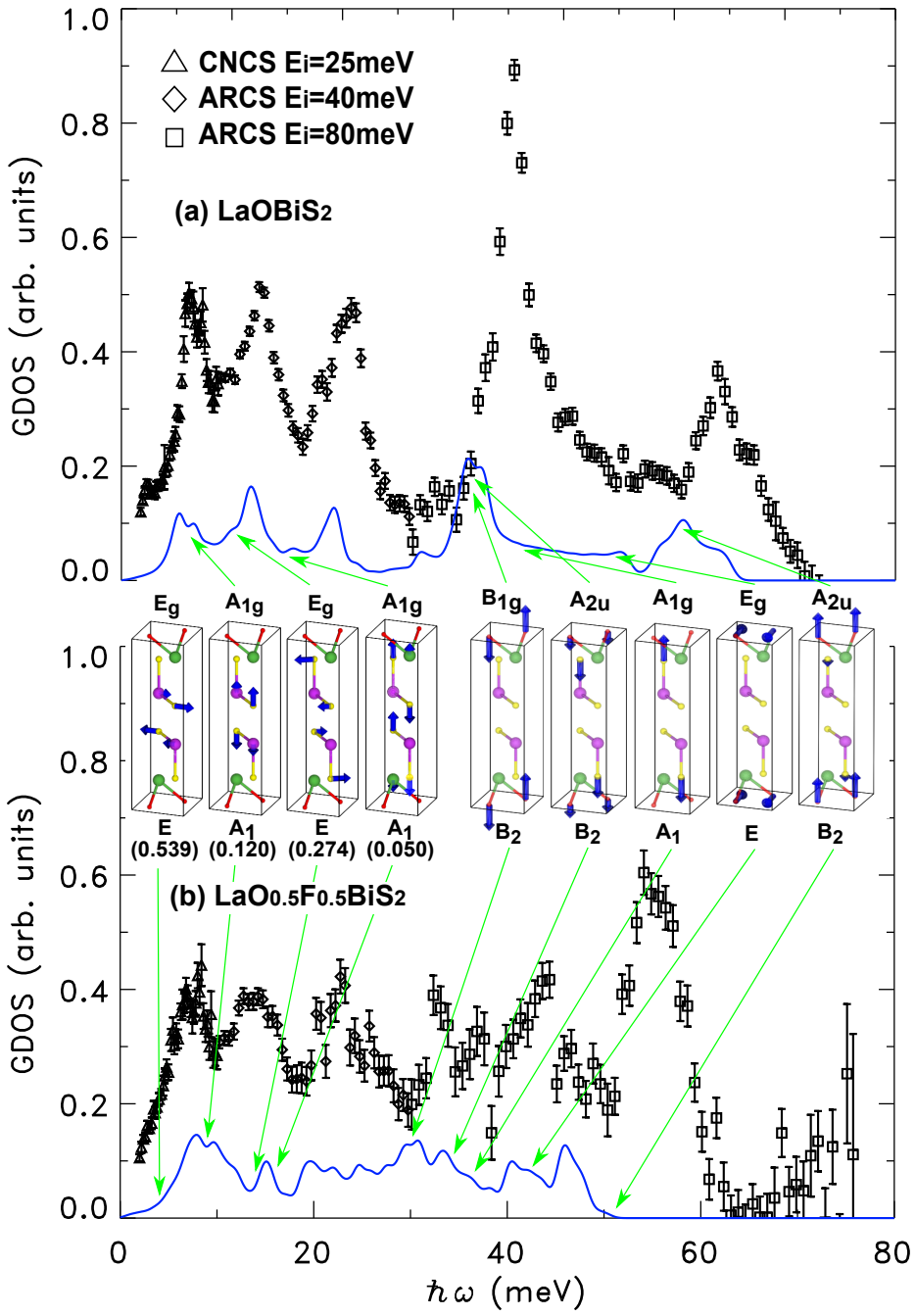

FIGURE 3.8: The phonon modes at the Γ point are shown in the inset with their symmetries for the parent (above) and SC (below) compound. Atoms are shown with the same colors as in Figure 3.6, and their relative displacements are represented with thick blue arrows. The left four figures in the inset are the vibrational modes that are theoretically expected to have the large e-ph couplings, with each λ shown in parentheses. For the first mode shown here, the corresponding energy becomes negative (-2.9 meV) in the parent compound. For doublet modes, only one of the two orthogonal modes is shown.

reduction of the sharp 40 meV peak, and softening of the highest energy O/F vibration modes. These changes can be partially understood as being due to the high energy O modes being shifted because of substitution with heavier F ions. This, however, fails to explain the low energy data. According to the calculation, solid lines in Figur 3.8, most of the e-ph coupling comes from the low energy modes below approx. 20 meV, and this is where we expect meaningful changes of the GDOS relevant to superconductivity to occur. While the theory predicts considerable re-distribution of GDOS in this low energy region, we do not observe any such change in the measured spectrum upon F doping.

Looking at the phonon mode more in detail, our phonon mode calculation at the zone center finds that there are 4 modes with significant electron-phonon coupling with $\lambda \approx 0.5$, 0.27, 0.12, 0.05 at 4.0, 13.77, 9.0, 16.0 meV, respectively, all at low energies. Their vibration modes all have definite in-plane or out-of-plane character as previously pointed out in Reference [60]. In the order of decreasing e-ph coupling, the 1st phonon mode (E = 4 meV) is longitudinal where whole BiS_2 plane is moving along the ab-direction. The 2nd mode (E = 13.77 meV) is also longitudinal, but in this case, only Sulfur ions are moving along ab-direction. So the effective mass of this phonon mode is lighter when compared with the 1st mode, and this results in higher energy. The 3rd mode (E = 9 meV) is the transverse mode with the whole BiS_2 plane moving in c-direction. The last mode (E = 16meV) is a transverse mode where only Sulfur ions are moving in c-direction, again resulting in higher energy. We list the calculated modes at the zone center in detail.

3.4.4 Details of the phonon modes calculation

3.4.4.1 Phonon modes at the Γ point

In Tables 3.4 and 3.5, all the phonon modes have been identified with their symmetry label together with the mode energies at the Γ point. It also shows the ions involved and their vibrational direction. All the modes have either in plane or out of plane vibrational character.

3.4.4.2 Convergence of the negative energy modes near M

In order to test the accuracy of our results, here we repeated the linear response phonon calculations at the M=$(\pi, \pi, 0)$ point for $LaO_{0.5}F_{0.5}BiS_2$, using different energy and charge cutoff as well as different k-point grid. We also test if the negative energy modes are sensistive to the the z-values of the S-atoms used in the calculations. We repeated calculations using both optimized atomic positions and experimental positions. The results are summarized in Table 3.6. From this table, it is clear that our calculations are well converged since the phonon energies do not change much with different cutoff and k-grid point. Most importantly, we always get the negative energy modes, which has been attributed to charge density wave ordering [60, 64].

3.4.5 Generalized phonon density of states measurement

3.4.6 Temperature dependence of GDOS

To further probe for a phonon anomaly associated with superconductivity, we also examine the temperature dependence of the dynamical susceptibility, $\chi''(\omega)$, of the SC $LaO_{0.5}F_{0.5}BiS_2$. Figure 3.9 shows $\chi''(\omega)$ at three different temperatures spanning $T_c \approx 10.8$ K. Our experimental data show that $\chi''(\omega)$ does not change within the experimental errors when the system transits from the normal to SC state. This suggests that, if it exists, the possible e-ph coupling in this material is much weaker than theoretically expected. We caution however that further detailed studies with a single crystal would be necessary to reach a more concrete conclusion in this regard.

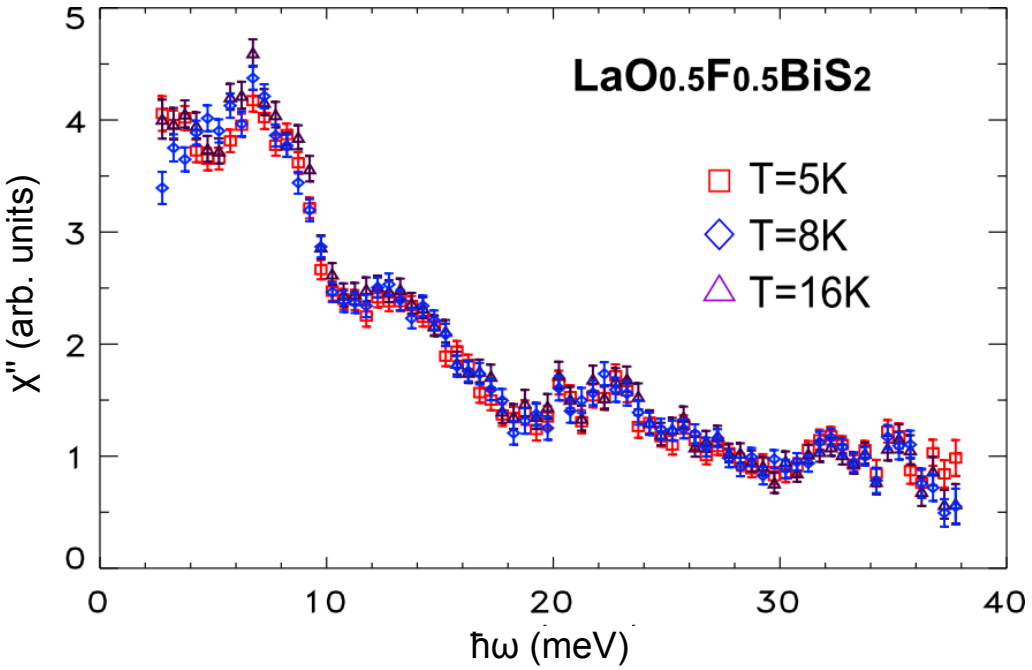

FIGURE 3.9: Temperature dependence of the dynamical susceptibility. The data have been measured at ARCS with E_i = 40 meV, and integrated over Q = [4, 7] $Å^{-1}$.

Mode	displacement direction	atoms involved	symmetry	energy (meV)
1 2	a - b diagonal a + b diagonal	S_1	E_u	-5.7
3 4	(mainly) b (mainly) a	S_1	E_g	-2.9
5 6	(mainly) b (mainly) a	all	E_u	0
7	along c	all	A_{2u}	0
8 9	a - b diagonal a + b diagonal	S_1	E_u	4.1
10 11	(mainly) a (mainly) b	S_1	E_g	5.2
12	along c	BiS_2 layer	A_{1g}	7.8
13	along c	S_1	A_{2u}	8.4
14 15	a - b diagonal a + b diagonal	S_2 and La	E_g	12.7
16	out of plane	S_1	A_{1g}	15.9
17	out of plane	S_1	A_{2u}	16.0
18 19	(mainly) b (mainly) a	S_2	E_u	17.4
20 21	(mainly) b (mainly) a	S_2	E_g	17.9
22	out of plane	La	A_{1g}	22.9
23 24	(mainly) a (mainly) b	O	E_u	33.9
25	out of plane	O	A_{2u}	35.9
26	out of plane	S_2 and O	B_{1g}	37.7
27	out of plane	S_2	A_{1g}	42.7
28 29	(mainly) b (mainly) a	O	E_g	52.5
30	out of plane	O	A_{2u}	58.9

TABLE 3.4: The zone-center phonon modes of parent compound based on the fully optimized structure. The symmetry decomposition of the phonons are $\Gamma = 4\ A_{1g} + 5\ A_{2u} + B_{1g} + 5\ E_u + 5\ E_g$. The optimized lattice parameters are a=b=4.029 Å, c=14.21 Å, z(La) = 0.0859, z(Bi) = 0.3676, z(S) = 0.6054, z(S) = 0.1899.

Mode	displacement direction	atoms involved	symmetry	energy (meV)	el-ph λ
1	(mainly) b	all	E	0.0	0.0
2	(mainly) a				
3	out of plane	all	B_2	0.0	
4	(mainly) b	S_2	E	4.0	0.539
5	(mainly) a				
6	(mainly) b	BiS_2 layer	E	5.2	0.001
7	(mainly) a				
8	out of plane	S_1 and La	B_2	7.6	0.002
9	(mainly) a	S_2	E	8.5	0.007
10	(mainly) b				
11	out of plane	BiS_2 layer	A_1	9.0	0.120
12	mixed	S_2	E	13.8	0.274
13	mixed				
14	out of plane	S_1	A_1	16.1	0.050
15	out of plane	S_1	B_2	16.9	0.014
16	mixed	S_1 and S_2	E	18.8	0.006
17	mixed				
18	out of plane	S_1 and La	A_1	19.9	0.013
19	mixed	S_1	E	20.7	0.001
20	mixed				
21	mixed	S_1	E	22.6	0.0
22	mixed				
23	(mainly) b	O/F	E	29.4	0.0
24	(mainly) a				
25	out of plane	F	B_2	29.8	0.009
26	out of plane	O	B_2	33.9	0.001
27	out of plane	S_2	A_1	38.2	0.144
28	(mainly) b	O/F	E	42.1	0.0
29	(mainly) a				
30	out of plane	O and S_2	B_2	51.83	0.005

TABLE 3.5: The zone-center phonon modes of the F substituted compound based on fully optimized structure. The symmetrey decomposition of the phonons are $\Gamma = 4\ A_1 + 6\ B_2 + 10\ E$. The optimized lattice parameters are a=b=4.0697 Å, c=13.3433 Å, z(La) = 0.89602, z(Bi) = 0.38448, z(S) = 0.6163, z(S) = 0.18494. The calculated electron-phonon coupling constant (λ) for each phonon mode is also given.

		Cal.1	Cal.2	Cal.3	Cal.4	Cal.5
		60 Ry	60 Ry	40 Ry	40 Ry	40 Ry
		600 Ry	600 Ry	480 Ry	480 Ry	480 Ry
		18x18x8	8x8x8	18x18x8	8x8x8	8x8x8
Mod.	Sym.	opt.	opt.	opt.	opt.	exp.
ω_1	A_1	-105.1	-118.2	-91.8	-118.1	-118.8
ω_2	B_1	-102.1	-114.5	-88.7	-114.4	-114.6
ω_3	B_2	-82.6	-82.8	-72.5	-82.7	-72.0
ω_4	A_2	-79.6	-77.0	-70.1	-76.9	-65.5
$\omega_{5,6}$	E	67.2	66.2	68.5	67.4	58.0
$\omega_{7,8}$	E	68.2	68.7	69.3	69.7	64.4
ω_9	B_2	74.7	76.5	75.8	75.8	66.9
ω_{10}	A_2	75.7	76.5	76.7	75.9	68.2
ω_{11}	A_1	77.5	77.0	77.3	77.8	72.5
ω_{12}	B_1	77.6	77.8	77.6	78.6	72.5
ω_{13}	B_2	77.8	79.1	78.4	80.2	82.3
ω_{14}	A_2	123.5	123.4	123.7	123.6	124.5
$\omega_{15,16}$	E	132.1	129.4	132.9	129.4	101.6
ω_{17}	A_1	156.8	156.9	156.7	157.0	156.8
ω_{18}	B_1	172.4	172.6	172.3	172.5	173.2
ω_{19}	A_2	185.3	184.3	186.6	185.3	196.2
ω_{20}	B_2	189.0	188.4	189.4	188.6	196.4
ω_{21}	A_1	193.4	193.0	193.5	192.9	199.7
ω_{22}	B_1	196.5	195.6	196.8	195.6	205.1
$\omega_{23,24}$	E	204.7	205.8	214.0	214.8	214.0
$\omega_{25,26}$	E	261.6	260.5	263.3	262.3	259.4
ω_{27}	A_2	263.8	264.0	272.2	272.4	271.5
ω_{28}	B_2	306.0	305.8	310.6	311.0	310.0
$\omega_{29,30}$	E	399.1	398.0	401.8	401.6	401.6

TABLE 3.6: The phonon modes at the $M(\pi, \pi, 0)$ for $LaO_{0.5}F_{0.5}BiS_2$ calculated with different energy and charge density cutoff and k-point grid. All the atomic positions were optimized except the last raw (cal.5) which is calculated using experimental z-positions for the S atoms. We note that regardless of the details of the calculations, we always get four negative energy modes. The mode energies are given in cm^{-1}.

3.5 Further study

In the neutron powder diffraction data of $LaO_{0.5}F_{0.5}BiS_2$, it should be noted that there are significant background under the Bragg peaks when compared with the almost flat background of $LaOBiS_2$. This is very likely to be related with the disorder in atomic positions of the superconducting sample, and further study on the local structure environment and its relationship with superconductivity using pair density function analysis is desired.

The relationship between crystallinity and superconductivity is another interesting problem that should be addressed in this system. Very recently, it has been reported [80] that high pressure(HP) annealing temperature influences both crystallinitiy and T_c of $LaO_{0.5}F_{0.5}BiS_2$. As can be seen from Figure 3.10 (a), the Bragg peak becomes much broader compared to the as-grown sample once annealed under HP. As we increase the annealing temperature, however, the Bragg peak gets sharper, and at the annealing temperature of 700 °C, it becomes as sharp as that of as-grown sample.

At the same time, as in Figure 3.10 (b), while the HP annealing process increases the transition temperature, the T_c decreases as we increase the annealing temperature. Also, at 700 °C, the T_c is as low as that of as-grown sample. In short, we can conclude that low crystallinity, or amorphousness could be beneficial for high superconducting transition temperature.

It has long been recognized [81] that crystalline disorder can induce the onset of an increase of the e-ph coupling to the transverse phonon modes, and the decrease of the coupling for the longitudinal mode, the net effect of which can increase the T_c. It will be an interesting follow-up study to measure the GDOS of samples annealed at different temperatures, and measure how transverse modes and longitudinal modes change as the system goes into superconducting states. This work may shed light on the relationship between the structure, crystallinity, and the superconductivity of this BiS_2 based superconductor.

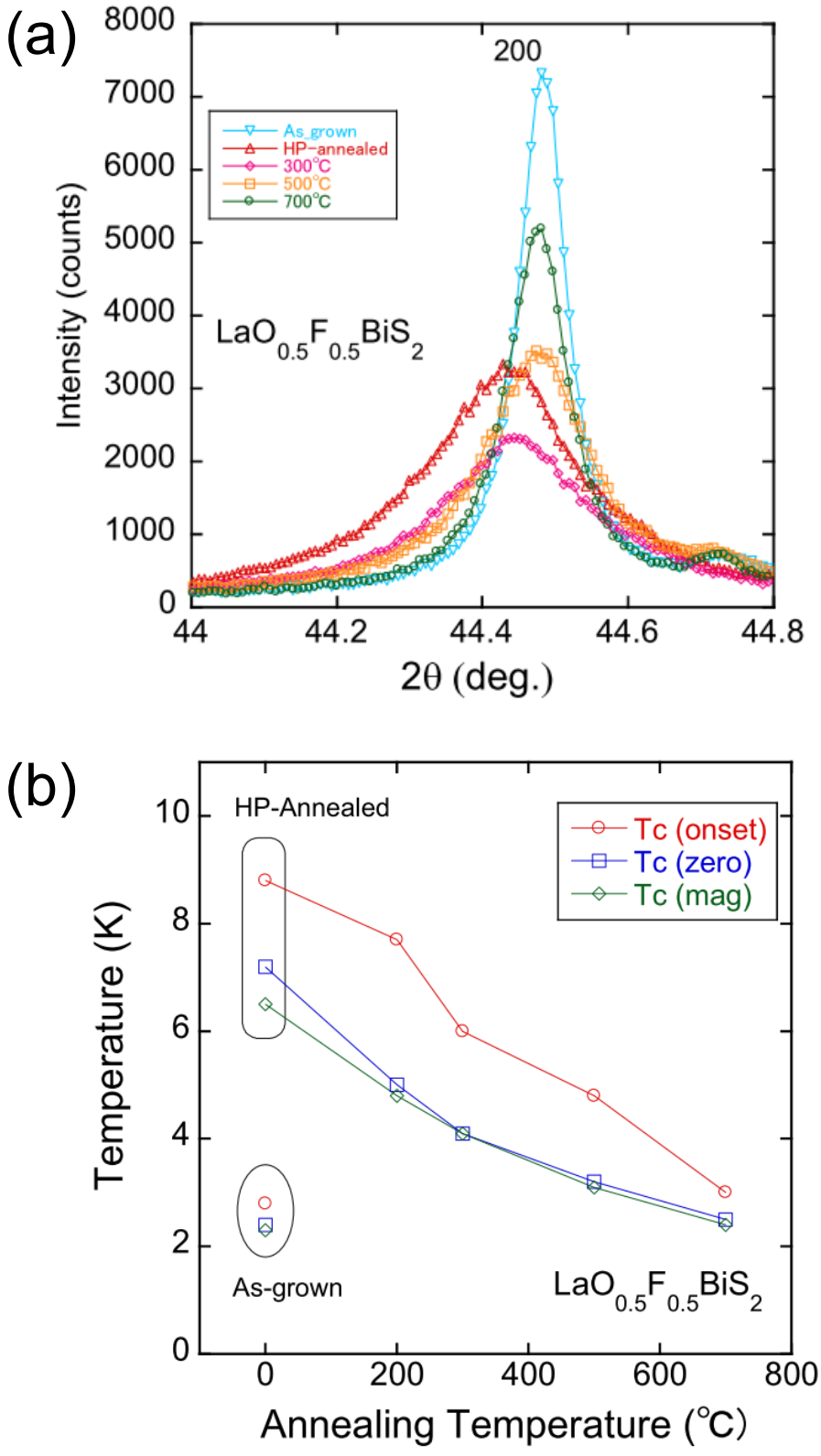

FIGURE 3.10: (a) X-ray diffraction patterns around Q = (200) peak at different annealing temperature under HP (b) Annealing temperature dependence of T_c (onset), T_c (zero), and T_c (mag). The former two are measured by the electrical resistivity, and the latter is measured by DC magnetic susceptibility. Panels are taken from reference [80].

3.6 Summary

In summary, our neutron powder diffraction data reveals the crystal structure of non-SC $LaOBiS_2$ and SC $LaO_{0.5}F_{0.5}BiS_2$. Large broadening of the Bragg peaks has been observed in the SC compound. In both compounds, discrepancies between experimental and calculated structural parameters have been observed, which suggest inherent structural instabilities in these systems. Furthermore, it was theoretically predicted that in the SC phase, a significant change in the phonon density of states at low energies would occur due to a possible large e-ph coupling. Our inelastic neutron scattering data, however, yields no considerable change in the low energy phonon modes as the system becomes SC either by F-doping or by cooling through the superconducting transition. Our results should provide important constraints on future theoretical works examining these new Bi-based superconductors.

Chapter 4

Ferromagnetism and Superconductivity in $CeO_{0.3}F_{0.7}BiS_2$

4.1 Introduction

It was generally thought that the ferromagnetism and supconductivity are mutually imcompatible [82]. Antiferromagnetism can coexist with superconductivity as the net magnetic effect would be zero in the Cooper pair size length scale. Ferromagnetism, on the other hand, is known to break the conventional s-wave singlet Cooper pairs in two ways: the orbital effect [83] and the paramagnetic effect [84, 85]. These effects are illustrated in Figure 4.1. The orbital effect occurs when the electrons of opposite momentum in a Cooper pair gain a Lorentz force in different directions from an external magnetic field. The paramagnetic effect occurs when the electrons of opposite spins in a Cooper pair get one of the electrons to flip spin by an external field. Both effects cause a spin-singlet Cooper pair to break. Meanwhile, in a spin-triplet Cooper pair, only orbital effect can contribute to breaking the pairing, which makes the p-wave superconductivity more favorable when there is ferromagnetism.

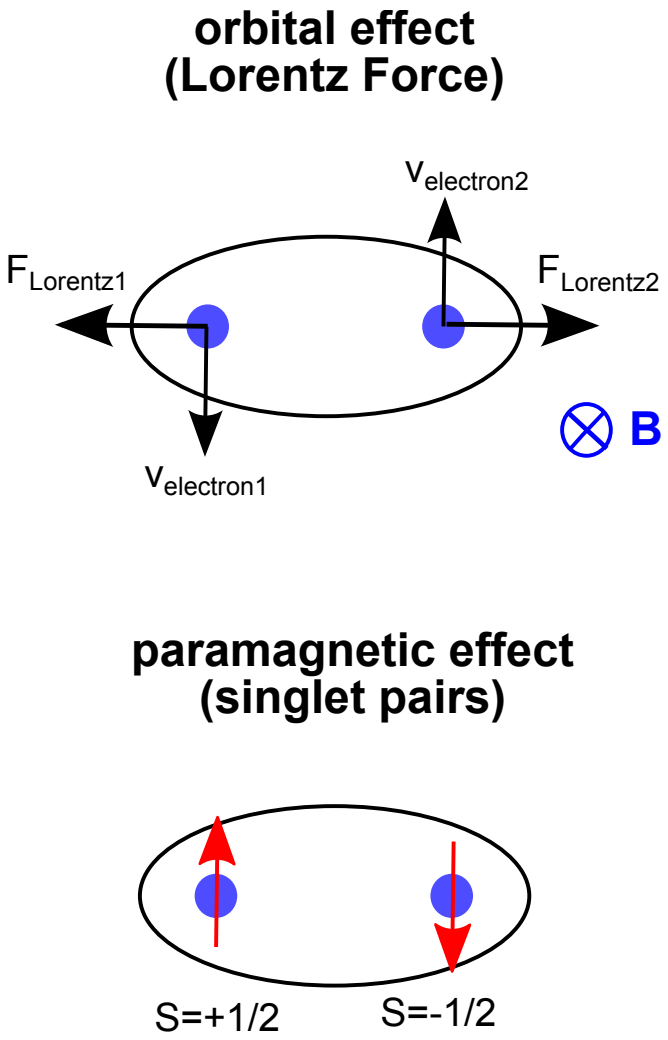

FIGURE 4.1: The antagonistic nature of magnetic field and s-wave Cooper pair.

Earlier examples of superconducting ferromagnets such as Chevrel [86–89] phases or borocarbides [90–94] demonstrate well the competing nature of ferromagnetism and superconductivity. For example, in Figure 4.2 showing the susceptibility and resistance of $ErRh_4B_4$ as a function of temperature, the system becomes superconducting below 8.7 K, and when cooled further, it undergoes a ferromagnetic phase transition at 0.8 K, below which it is no longer superconduting.

Nevertheless, there are still some mechanisms by which superconductivity can coexist with ferromagnetism [95, 96]. When the internal magnetic field is greater than a lower

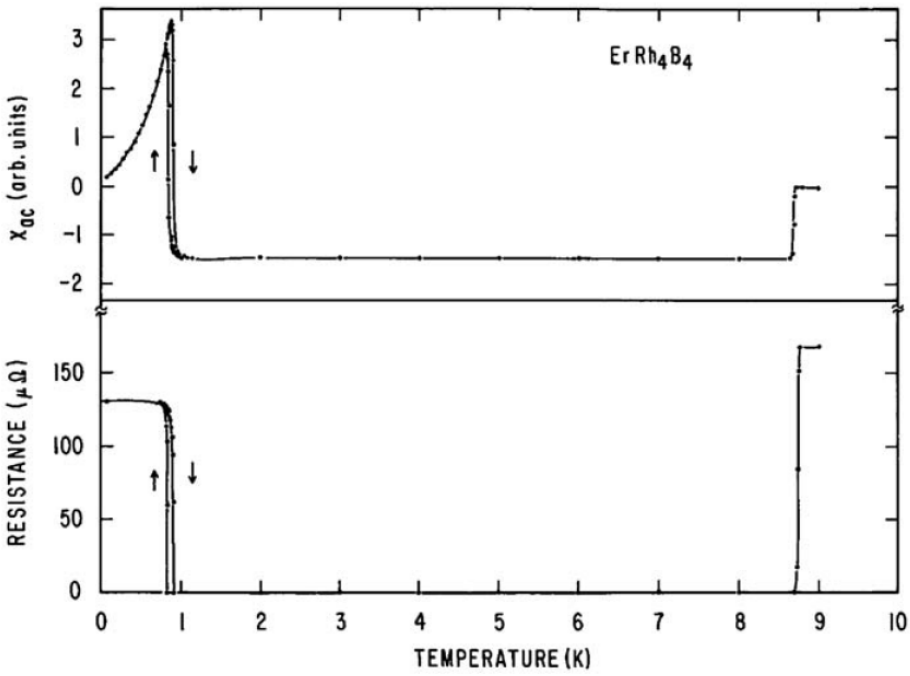

FIGURE 4.2: (top) The ac magnetic susceptibility and (bottom) electrical resistance of $ErRh_4B_4$ as a function of temperature. The panels are taken from Reference [89].

criitical field, H_{c1}, a spontaneous vortex state would be more favorable where the ferromagnetic field exists inside vortices, as shown in Figure 4.3. However, actual systems exhibiting the coexistence is quite rare, including only some heavy fermion superconductors [97–107], Ruthenate-layered cuprates [108–113], $Eu(Fe_{1-y}Co_y)_2(As_{1-x}P_x)_2$ [114–119], and $CeFe(As_{1-y}P_y)(O_{1-x}F_x)$ [120–124].

The ferromagnetic ordering temperature of these systems is known usually to be quite low. This suggests that dipolar interactions may be responsible for the ferromagnetism, which is a usual case in rare earth magnetism. However, in some materials, the ordering temperature is too high to be explained by only diploar interactions. Furthermore, antiferromagnetic ground states are sometimes found even with the same crystal structure, which is hard to be explained with simple diploar interactions. Hence, to better understand the physics of unconventional superconductivity, it is crucial to answer the questions on what the nature of magnetic interactions in a superconductor is, how the magnetism interacts with superconductivity, and how

superconductivity can survive in a ferromagnetic background.

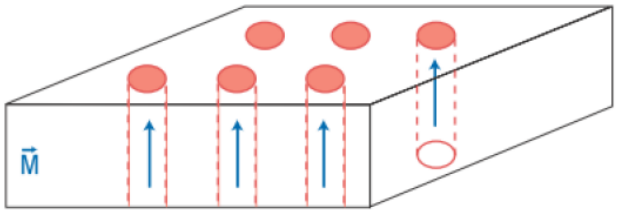

FIGURE 4.3: The mechanism of coexistence of ferromagnetism and superconductivity by forming a spontaneuous vorext state. Panels are take from Reference [125].

The recently found BiS_2-based superconductors are interesting in that they share many common features with other unconventional superconductors like cuprates or iron-based superconductors. Whether the superconducting mechanism in this new superconductors is conventional or unconventional, however, is still under debate. In this regard, the $CeO_{1-x}F_xBiS_2$ sample is unique due to its possible coexistence of ferromagnetism and superconductivity in the low temperature region [126]. The existence of ferromagnetism is observed in the magnetic susceptibility measurements, and it is further supported in the isothermal magnitization-hysterisis-loops. The ferromagnetism in this system is believed to be coming from the ferromagnetic ordering of Ce ions in the CeO layers. Our goal is to determine the nature of magnetic ordering below T_{FM} and the interactions between the magnetic moments by neutron scattering. This study will help us understand the relationship between magnetism and superconductivity in this rare case of coexistence of ferromagnetism and superconductivity.

4.2 Experimental details

A 1.0 g polycrystalline sample of $CeO_{0.3}F_{0.7}BiS_2$ was synthesized using the solid state reaction method under high pressure at NIMS in Tsukuba, Japan. Figure 4.4 shows the low-temperature magnetic susceptibility data. As shown in Figure 4.4, the magnetic susceptibility increases at $T_{FM} \approx 7.5$K, while showing the divergence between field-cooled and zero-field-cooled data. This suggests the onset of spin-glassy ferromagnetism below T_{FM}. On further cooling under zero field, the susceptibility drops at $T_c \approx 5.5$K signaling the onset of a large diamagnetic susceptibility from bulk superconductivity. Recent specific heat measurement also confirms that the superconductivity in this sample is bulk in nature [56].

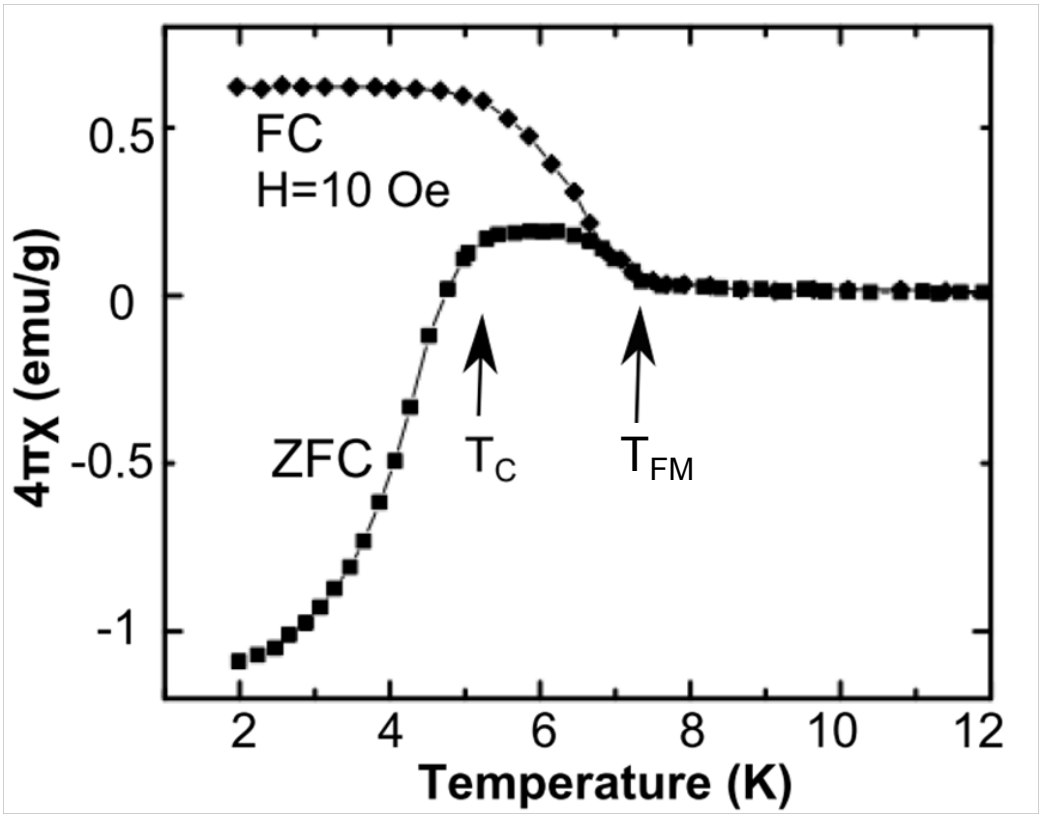

FIGURE 4.4: Magnetic susceptibility measurement of $CeO_{0.3}F_{0.7}BiS_2$

Neutron scattering measurements were performed at the High Flux Isotope Reactor(HFIR) using HB2A powder diffractometer, and at the Spallation Neutron Source

(SNS) using the POWGEN diffractometer, and the Cold Neutron Chopper Spectrometer (CNCS). Samples were loaded into vanadium cans for the diffraction measurements (at HB2A and POWGEN) or aluminum can for the inelastic neutron scattering measurement (at CNCS) with a He atmosphere and mounted to the liquid helium cryostat. When an external magnetic field was applied, a magnet that can go up to 5 T was used.

Neutron diffraction data from HB2A were collected with a constant wavelength of 1.5408 Å at 2K and 20K. Data from POWGEN [70] were collected using a wavelength band to cover a wide range of d spacing from 0.28 to 3.10 Å or from 1.7 to 8.2 Å at 2K, 6K, and 10K. Inelastic neutron scattering (INS) measurements were performed at CNCS [72] with monochromatic neutrons of incident energies E_i = 4meV. All the INS data presented here are corrected for background by subtraction of an empty can measurement.

4.3 Zero field study

4.3.1 Crystal and magnetic structure

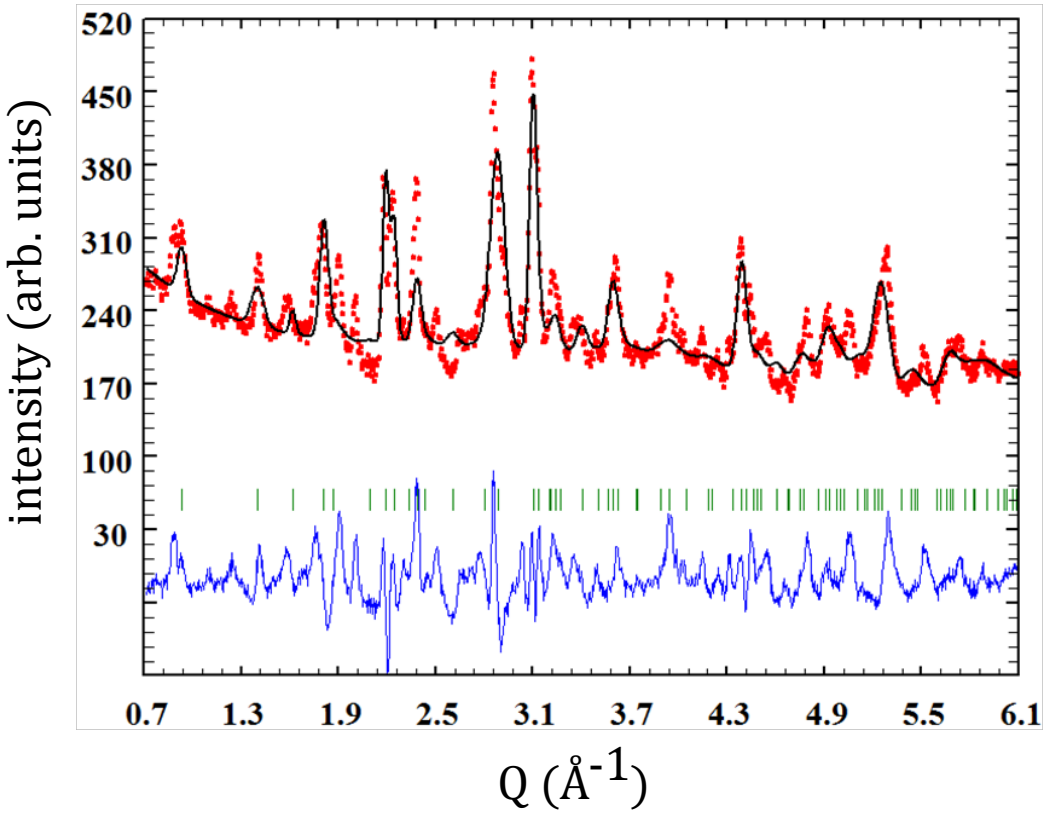

FIGURE 4.5: Neutron Powder Diffraction and the crystal structure refinement of $CeO_{0.3}F_{0.7}BiS_2$ at T = 10K obtained from HB2A. The red squares indicate the data observed, and the black solid line represents the fit to the data. The green horizontal bars indicate Bragg reflection positions of $CeO_{0.3}F_{0.7}BiS_2$, and blue solid line show the difference between measured and fitted intesities.

Figure 4.5 shows the neutron powder diffraction data obtained from HB2A at T = 10K. Similar results have been found from the POWGEN experiment as well. We find significant broadening of the Bragg peaks and large background in the data, which suggest a disordered nature in this system. These characteristics are similar to those of La(O,F)BiS_2, but the broadening is even larger in this system.

$CeO_{0.3}F_{0.7}BiS_2$ P4/nmm T=10K		$\chi^2 = 8.30$
	a (Å)	4.043(1)
	c (Å)	13.519(8)
Ce	2c (0.5, 0, z)	0.114(1)
Bi	2c (0, 0.5, z)	0.622(2)
S_1	2c (0.5, 0, z)	0.360(1)
S_2	2c (0.5, 0, z)	0.850(5)
O/F	2a (0, 0, 0)	–

TABLE 4.1: Refined structural parameters of $CeO_{0.3}F_{0.7}BiS_2$ obtained from neutron powder diffraction using Fullprof [127]. Numbers in parentheses correspond to one standard deviation in the mean value.

Furthermore, it is found that there are several impurities in this compound, including Bi_2S_3 indexed with x-ray diffraction data. It is very likely that there is another significant phase with similar lattice parameters of the main phase since there are two peaks overlapped near the Q =(002) position, or $|Q| \approx 0.9\ \mathring{A}^{-1}$. This new impurity, however, could not be identified with existing crystallographic database. Two peaks around Q=(002) yield two different c-lattice parameters of 14.23 Å and 13.49 Å. Since other similar BiS_2-based superconductors yield c-lattice parameter about 13 Å, it is reasonable to assume the larger d-spacing peak is coming from an impurity phase.

S_{400}	S_{004}	S_{220}	S_{202}
7.471E+01	9.794E+00	1.302E+02	2.913E+01
(0.695E+01)	(1.212E+00)	(0.366E+02)	(0.767E+01)

TABLE 4.2: The anisotropic phenomenological strain parameter used to fit the diffraction pattern of $CeO_{0.3}F_{0.7}BiS_2$. The numbers in the parentheses represent estimated error.

Excluding the peak corresponding to the large c-axis, we were able to reproduce the neutron diffraction data with space group P 4/n m m, and with the structure parameters shown in Table 4.1. The black solid line shown in Figure 4.5 is the best fit we could obtain with the use of phenomenological model of anisotropic broadening. Again, for the tetragonal crystal system, the possible non zero anisotropic strain parameters are S_{400}=S_{040}, S_{202}=S_{002}, S_{004}, and S_{220}, whose refined parameters are

summarized in Table 4.2.

As we cool down the sample to the base temperature, approx. 1.5 K, we observed an increase of the neutron scattering intensities on top of the nuclear Bragg peaks as shown in Figure 4.6 (a). This suggests that there is a ferromagnetic ordering of Ce^{3+} ions. The increase is especially significant at Q = (102) peak, and the summed intensities of Q=(102) Bragg peak are plotted as a function of temperature in Figure 4.6 (b). When the sample is cooled down to the base temperature, the summed intensities seem to go through a 2nd order phase transition around $T_{FM} \approx 7$K, and below about 4 K, the intensity, i. e., the magnetic moment saturates.

It is, however, not straight-forward to refine the magnetic structure. The nuclear Bragg peaks are very broad, the magnetic signals are weak, and there are many impurity phases overlapped. The situation is worse in case of ferromangetic order since their effect are often obscured by other effects related with nuclear Bragg peaks, such as thermal effects, or strain/stress broadening.

Fortunately, we can use group theoretical analysis to determine the type of magnetic order in this system. With the naive interpretation of Landau theory of second order phase transition associated with a symmetry breaking, only one of the irreducible representations will become critical at the transition. In P 4/n m m crystallographic space group, there are, in total, 4 possible irreducible representations (IRs): Γ2, Γ3, Γ9, Γ10. They represent antiferromagnetic ordering with spins along the c-axis, ferromagnetic ordering with spins along the c-axis, ferromangnetic ordering with spins in the ab-plane, and antiferromangetic ordering with spins in the ab-plane, respectively. Their spin configurations, or basis vectors, for each IR are shown in Figure 4.7.

The model magnetic neutron scattering intensities for each IR are shown in Figure 4.8. Let us first consider the case where spins are lying along the c-axis: Γ2 and Γ5. If the spins are along the c-axis, there cannot be any (00L) magnetic Bragg peaks because only spin moment orthogonal to the wave vector can contribute to the scattering intensities. While the strongest peaks are (100) and (101) in the antiferromagnetic

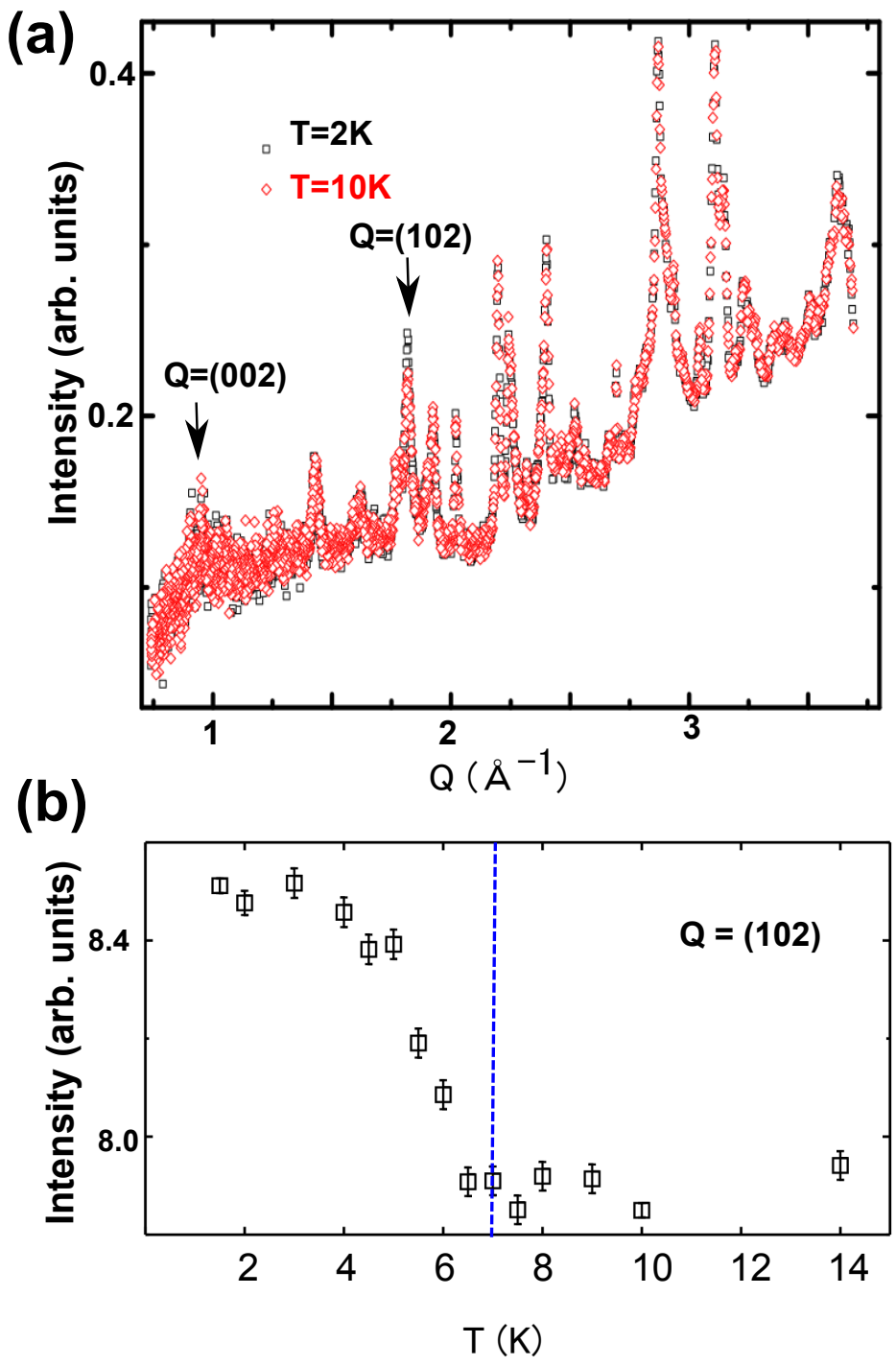

FIGURE 4.6: (a) The NPD $CeO_{0.3}F_{0.7}BiS_2$ below and above the magnetic phase transition temperature, T_{FM}. (b) The summed intensity of the Q = (102) Bragg peak as a function of temperature.

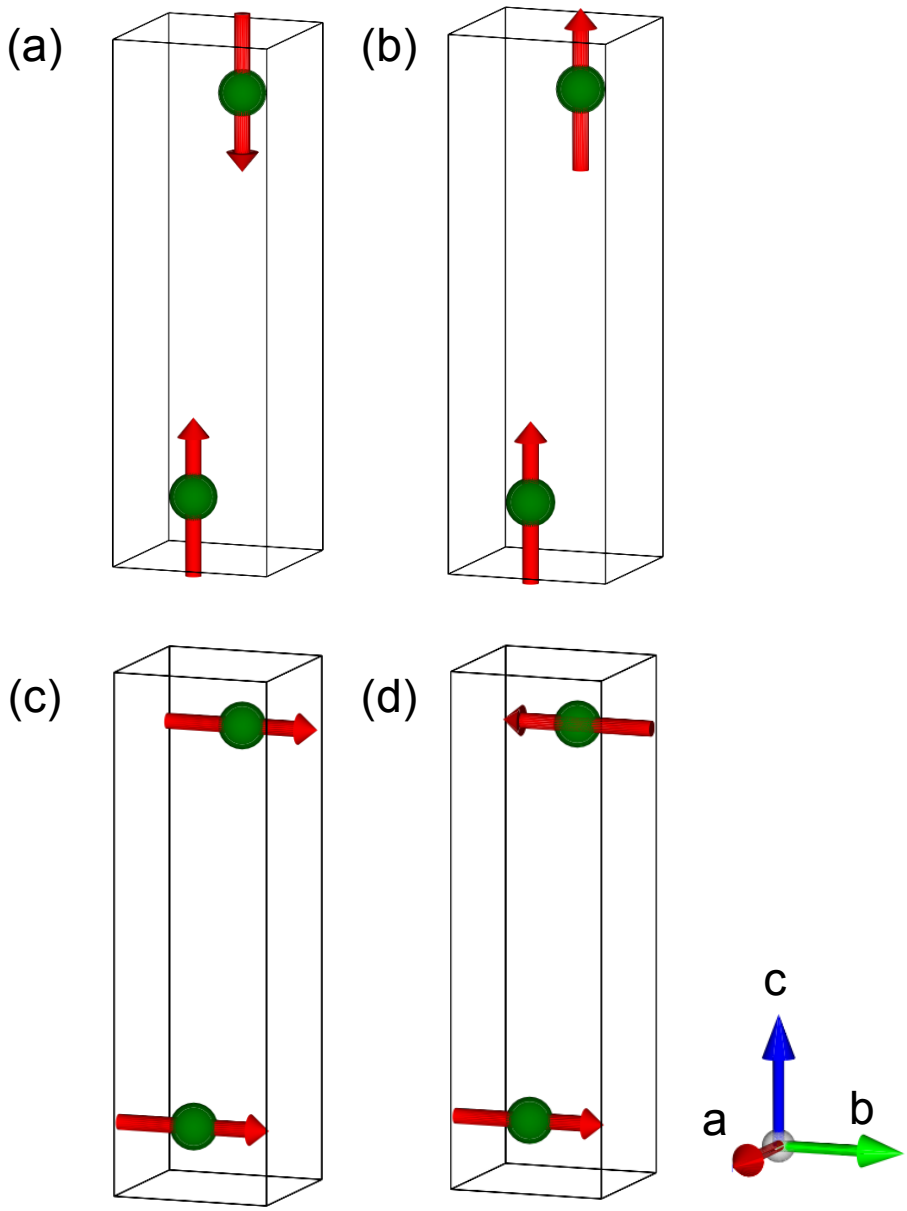

FIGURE 4.7: The basis vectors of each irreducible representation: (a) Γ2, (b) Γ3, (c) Γ9, (d) Γ10. The order of Γ9 and Γ10 are 2, which means there will be two basis vectors in these IRs, while the order of Γ2 and Γ3 is 1, hence one basis vector for them. Here, for Γ9 and Γ10, only one basis vector along b-direction is shown here: the other is just orthogonal being along a-direction.

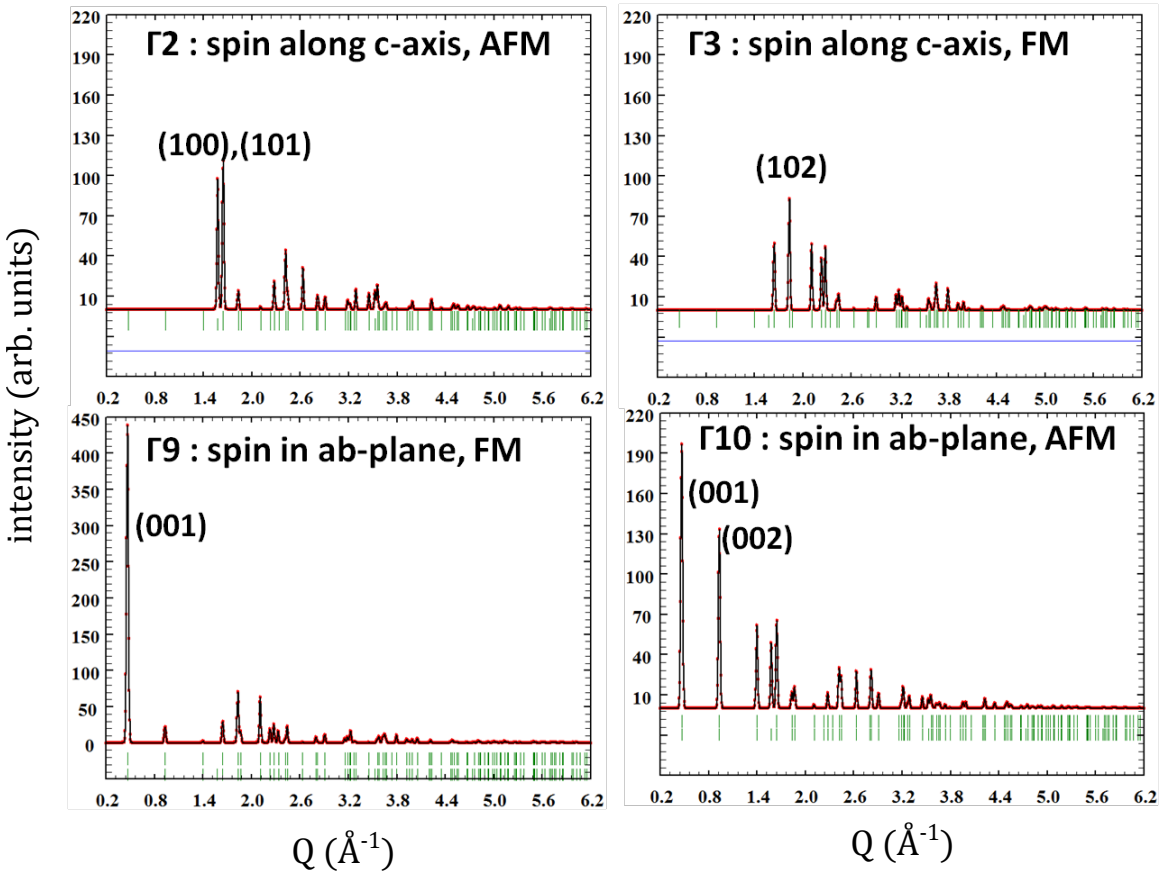

FIGURE 4.8: Group theoretical analysis on the possible magnetic structures and their neutron scattering intensities.

spin configuration of Γ2, the (102) peak is the strongest peak in the ferromagnetic spin configuration of Γ5.

On the other hand, if the spins are in the ab-plane as in Γ9 and Γ10, we can have (00L) type magnetic Bragg peaks. It turns out that the (001) magnetic Bragg peak is uncomparably the strongest peak in ferromagnetic configuration of Γ9. If the magnetic order is antiferromagnetic in the ab-plane as in Γ10, the (002) peak is also comparable with the still-strongest (001) peak.

From these arguments, since the increase of scattering intensities are prominent at Q = (102), we can conclude our system belongs to IR of Γ3 showing ferromagnetic

ordering of Ce^{3+} magnetic ions along the c-axis. It is unlikely for other IRs to be mixed with Γ3 as small component along the c-axis, whether AFM or FM, would have produced significant scattering at Q=(001), which could not be confirmed within the instrumental resolution.

4.3.2 Spin fluctuation

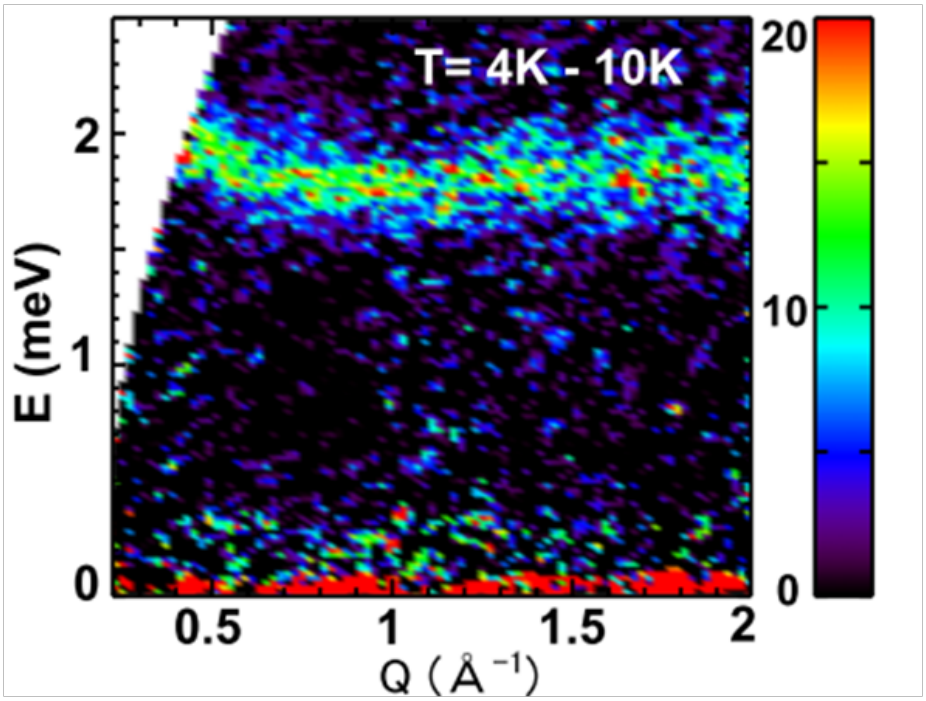

FIGURE 4.9: The contour map of inelastic neutron scattering intensity in Q-E space

To study the interactions between the spin moments, we performed an inelastic neutron scattering experiment at CNCS. In order to observe only magnetic signals, we used T = 10K data above the magnetic phase transition temperature as a background in our analysis. Below T_{FM}, we find the emergence of strong, and rather flat excitation as can be seen in Figure 4.9.

We can also plot the inelastic neutron scattering intensities along the energy transfer as in Figure 4.10 (a), and we could find that the excitation is centered around E = 1.8 meV. This excitation becomes weaker as we increase the temperature, and is suppressed to the background level above T_{FM}.

This dependence becomes more evident when we plot the summed intensity as a function of temperature as in 4.10 (b). We summed the neutron scattering intensities over a region of interest in the Q-E space: the intensity has been integrated over Q-space of [0.5, 2.0] $\mathring{A}^{-1}$ for the pronounced magnetic effect, and over E-space of [1.5, 2.5] and [0.5, 1.5] meV for the magnetic excitation and background, respectively. We also over-plot the summed intensities of the Q = (102) magnetic Bragg peak arbitrarily scaled for comparison.

It is clear that both the magnetic Bragg peak and the summed intensities over E = [1.5, 2.5] begin to increase at the same temperature around $T_{FM} \approx 7.5$ K and become almost saturated below 4 K. Meanwhile, the summed intensity over E = [0.5, 1.5] begins to decrease around T_{FM} satisfying the neutron scattering sum rule, meaning that the depleted scattering at this Q-E space contributes to the scattering of the emergent excitation. From this trend, we can conclude that the nature of this E $\approx$ 1.8meV excitation is spin-wave, i. e., collective excitation of ordered magnetic moments.

In order to understand the nature of spin interaction in this system, we can model the spin Hamiltonian as in Equation 4.1.

$$H = \sum_{i,j} J_{i,j} \vec{S}_i \cdot \vec{S}_j + D \sum_i S_{i,z}^2 + g\mu_B \sum_i \vec{B} \cdot \vec{S}_i \tag{4.1}$$

Here, isotropic Heisenberg interaction has been assumed. $J_{i,j}$, D, and B are the exchange integral, the anisotropy, and the external magnetic field, respectively. g is the

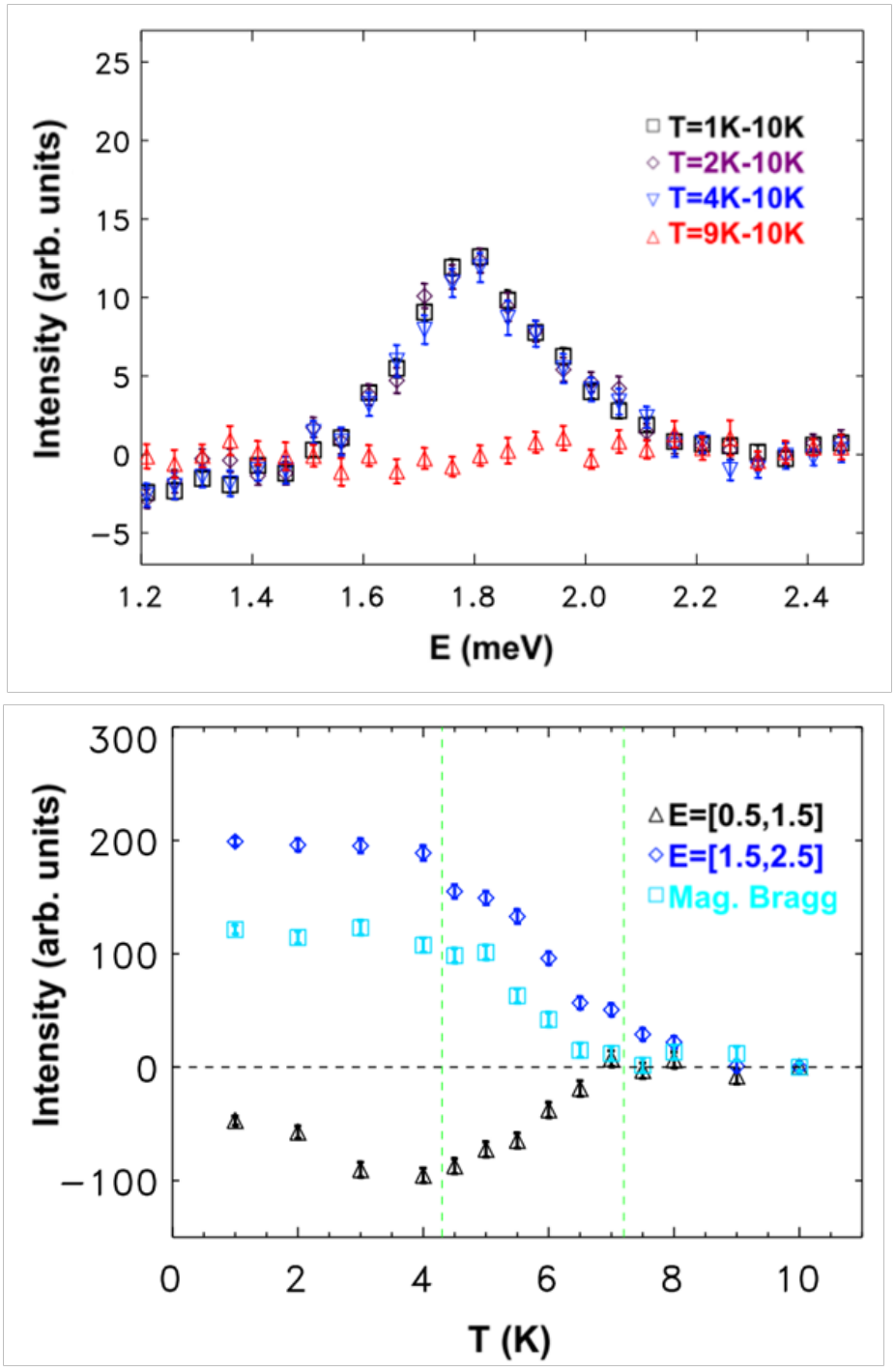

FIGURE 4.10: (top) Inelastic neutron scattering intensity around E ≈ 1.8meV across the T_C and T_{FM}. (bottom) The summed intensity over Q-E region of interest as a function of temperature.

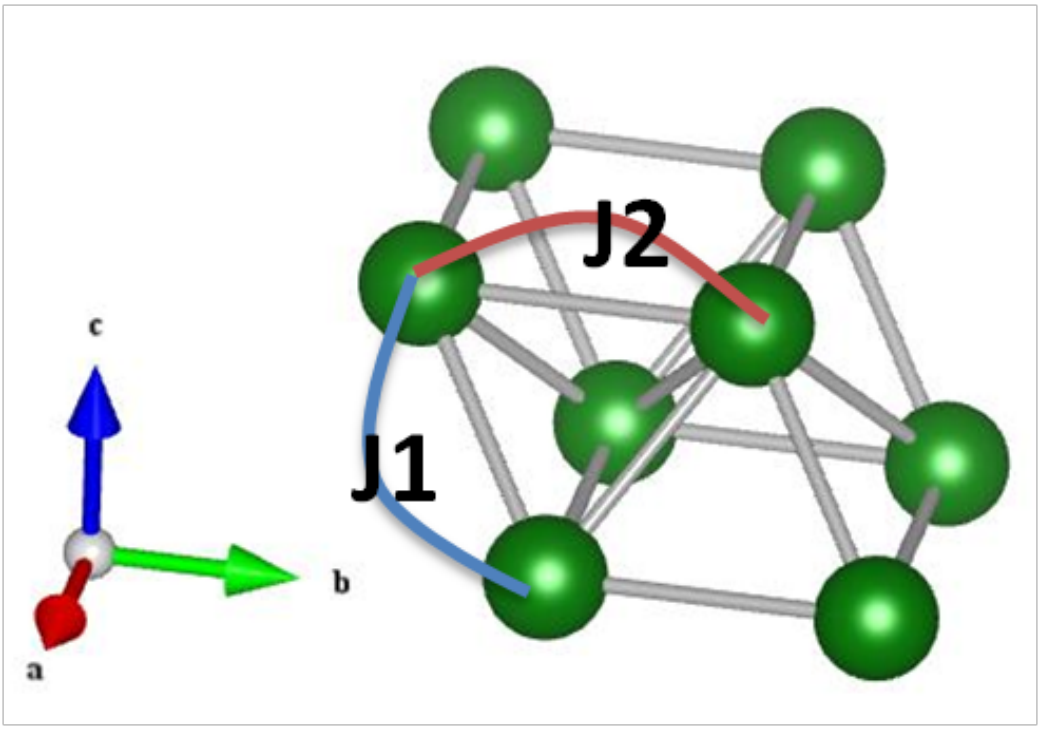

FIGURE 4.11: Schematic diagram showing J_1 and J_2

g-factor, and μ_B is the Bohr magneton. The first term describes the isotropic Heisenberg interaction between the magnetic moments, and the second term accounts for the anisotropy term, which aligns the spins along the c-axis if negative, and in the ab-plane if positive. The last term gives rise to the Zeeman energy from the external magnetic field.

For the exchange interactions, nearest neighbor(NN) J_1 and next-nearest neighbor(NNN) J_2 have been considered. The corresponding bonds for J_1 and J_2 are shown in Figure 4.11, and their lengths correspond to 4.20 $\mathring{A}$ and 4.04 $\mathring{A}$, respectively, while the next shortest bond length is about 5.72 $\mathring{A}$. Therefore, it suffices to consider only two exchange interactions in this case.

This Hamiltonian can be solved analytically, and gives the eigenenergies in the form of

$$E = -4J_1 - 4J_2 + J_2 \sum_{\vec{R_2}} cos(\vec{k}\cdot\vec{R_2}) + g\mu_B B - 2D + |J_1| \sum_{\vec{R_1},\vec{R_2}} cos(\vec{k}\cdot(\vec{R_1}-\vec{R_2})). \quad (4.2)$$

We find the parameters of J_1 = -0.5 and J_2 = -0.4 best reproduces the given dispersion of the spin wave. The effect of anisotropy, D, should be negligibly small, as it produces very low energy excitation whose energy gap would be proportional to $2D$. For example, dispersions along high symmetric direction have been plotted in Figure 4.12 for the case J_1 = -0.5, J_2 = -0.4, and also for the case J_1 = -0.5, J_2 = -0.4, and D = -0.1 case.

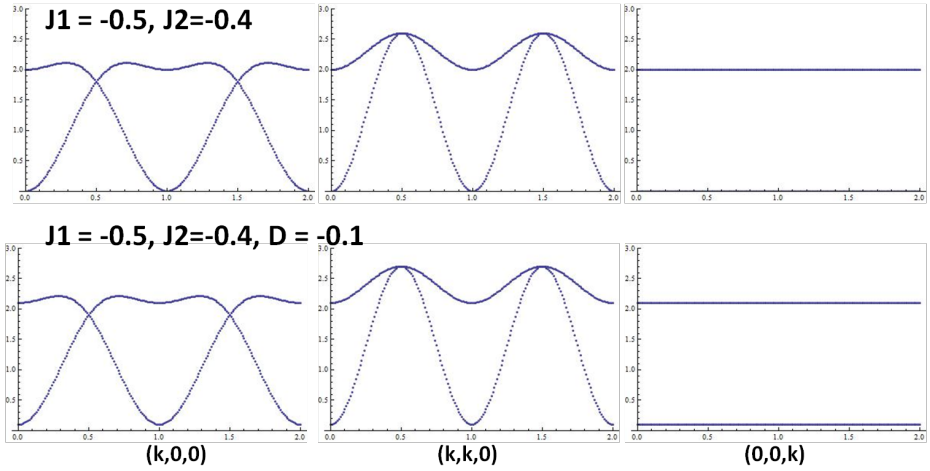

FIGURE 4.12: The calculated spin wave dispersion along high symmetry directions (k,0,0), (k,k,0) and (0,0,l) with and without the anisotropy term.

For a more comprehensive analysis, the scattering intensities were calculated as well. The neutron scattering intensities are calculated assuming the sample is a single crystal, and then the intensities are averaged over all Brillouin zone for the case of powder. The final result is shown in the Figure 4.13. We then simulated the excitation around 1.8 meV, while the flat mode is coming from the van-Hove singularity. We also tried other models with a non-Heisneberg interaction, such as the Ising model, or the XY-model. However, none of these could reproduce the given data well, confirming the

isotropic nature of the magnetic interaction in this system.

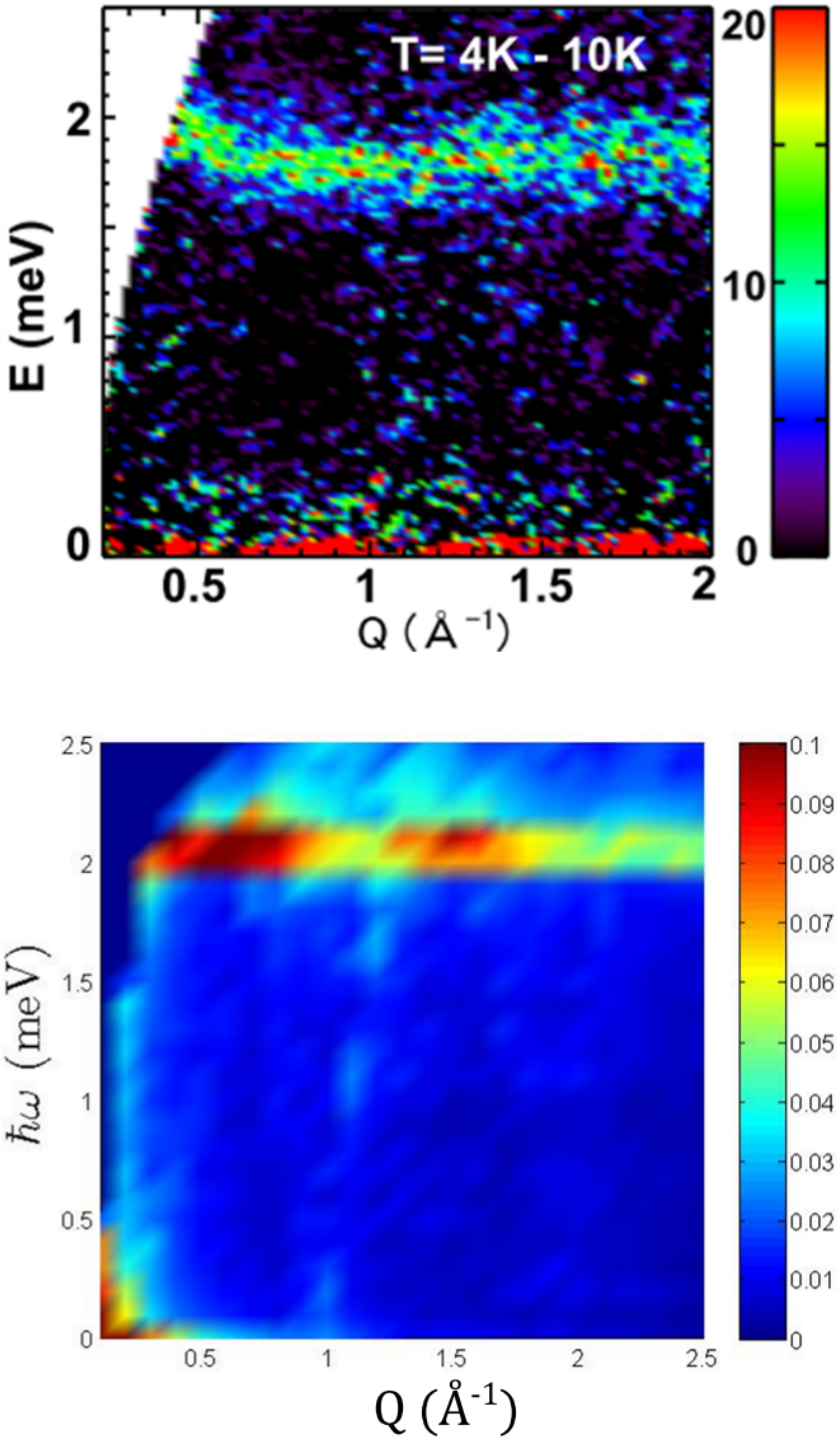

FIGURE 4.13: The calculated spin wave intensity compared with experimental result.

4.3.3 Calculation of spin wave dispersion

Here, we will derive the spin wave dispersion analytically. We only consider the isotropic Heisenberg spin Hamiltonian with nearest neighbor and next-nearest neighbor interactions. Other types of interactions including magnetic anisotropy or magnetic field dependence will not be considered here. This derivation is described more in detail in the Appendix C.

The first term in Equation 4.1 can be written as

$$H = \sum_i \left\{ J_1 \sum_{\vec{R_1}} \left(\vec{S_A} \cdot \vec{S_B} + \vec{S_B} \cdot \vec{S_A} \right) + J_2 \sum_{\vec{R_2}} \left(\vec{S_A} \cdot \vec{S_{A'}} + \vec{S_B} \cdot \vec{S_{B'}} \right) \right\} \tag{4.3}$$

Here, A and B are ions in different sublattices, and $\vec{R_1}$ and $\vec{R_2}$ are the displacement related to J_1 and J_2, respectively. As can be seen from Figure 4.11, J_1 corresponds to an interlayer coupling, while J_2 corresponds to an intralayer coupling. We can rewrite the x and y component of spin S, S^x and S^y, with lowering and raising operator when the z-axis is defined as the quantization. Then, the J_1 terms and J_2 terms in the Hamiltonian are

$$J_1 \sum_{\vec{R_1}} \left(\vec{S_A} \cdot \vec{S_B} + \vec{S_B} \cdot \vec{S_A} \right) \tag{4.4}$$

$$= 2J_1 \sum_{\vec{R_1}} \left(\frac{1}{2} \left(S_A^+ S_B^- + S_B^- S_A^+ \right) + S_A^z S_B^z \right), \tag{4.5}$$

$$J_2 \sum_{\vec{R_2}} \left(\vec{S_A} \cdot \vec{S_{A'}} + \vec{S_B} \cdot \vec{S_{B'}} \right) \tag{4.6}$$

$$= J_2 \sum_{\vec{R_2}} \left(\frac{1}{2} \left(S_A^+ S_{A'}^- + S_A^- S_{A'}^+ \right) + S_A^z S_A^z + \frac{1}{2} \left(S_B^+ S_{B'}^- + S_B^- S_{B'}^+ \right) + S_B^z S_B^z \right). \tag{4.7}$$

To describe spin wave excitations, it is convenient to introduce Holstein-Primakoff transformation. It is a mapping from the angular momentum operators to spin-wave boson operator: a^+, for creation, and a, for annihilations with $|n\rangle$ being an eigenstate of a^+a having eigenvalue n corresponding to the spin-deviation quantum number, n. We obtain

$$\left[a,\ a^+\right] = 1 \tag{4.8}$$

$$a\,|n\rangle = \sqrt{n}\,|n-1\rangle\,, \quad a^+\,|n\rangle = \sqrt{n+1}\,|n+1\rangle\,, \quad a^+a\,|n\rangle = n\,|n\rangle\,. \tag{4.9}$$

For sublattice B, another set of bosonic operators b^+ and b are applied in the same way as sublattice A.

Furthermore, if the spin-deviation $n << S$, which is not a strict restriction since a spin-deviation can be spread over all the spin moments as a wave, we can use the "linear approximation" which is expressed as

$$\begin{aligned} S^+_{A,i} &\approx \sqrt{2S}a_i \quad & S^+_{B,i} &\approx \sqrt{2S}b_i \\ S^-_{A,i} &\approx \sqrt{2S}a_i^+ \quad & S^-_{B,i} &\approx \sqrt{2S}b_i^+ \\ S^z_{A,i} &\approx S - a_i^+a_i \quad & S^z_{B,i} &\approx S - b_i^+b_i. \end{aligned} \tag{4.10}$$

It should be noted that the signs of the $S_{B,i}$ components are decided by the relationship of the spin directions of the two sublattices. In this approach, therefore, it is essential to know the magnetic ground spin configuration in advance to find the spin wave excitation.

Applying these relationships, the J_1 terms in the Hamiltonian become

$$= 2J_1S\sum_{\vec{R_1}}\left(a_ib^+_{i+R_1} + a_i^+b_{i+R_1} - a_i^+a_i - b^+_{i+R_1}b_{i+R_1}\right), \tag{4.11}$$

and the J_2 terms become

$$\begin{aligned} = J_2 S \sum_{\vec{R_2}} \; (\; & a_i a^+_{i+R_2} + a^+_i a_{i+R_2} - a^+_i a_i - a^+_{i+R_2} a_{i+R_2} \\ & + b_i b^+_{i+R_2} + b^+_i b_{i+R_2} - b^+_i b_i - b^+_{i+R_2} b_{i+R_2} \;) \; . \end{aligned} \tag{4.12}$$

To find out the dispersion relation, we can Fourier-transform the bosonic operators to momentum space.

$$\begin{aligned} a_i &= \frac{1}{\sqrt{N}} \sum_{\vec{k}} e^{+i\vec{k}\cdot\vec{r_i}} a_{\vec{k}} \qquad b_i = \frac{1}{\sqrt{N}} \sum_{\vec{k}} e^{+i\vec{k}\cdot\vec{r_i}} b_{\vec{k}} \\ a^+_i &= \frac{1}{\sqrt{N}} \sum_{\vec{k}} e^{-i\vec{k}\cdot\vec{r_i}} a^+_{\vec{k}} \qquad b^+_i = \frac{1}{\sqrt{N}} \sum_{\vec{k}} e^{-i\vec{k}\cdot\vec{r_i}} b^+_{\vec{k}} \end{aligned} \tag{4.13}$$

Then, J_1 terms reduce to

$$= \sum_k 2S \; \left[\; J_1(k) \, a_k b^+_k + J_1(-k) \, a^+_k b_k - J_1(0) \, a^+_k a_k - J_1(0) \, b^+_k b_k \; \right] \tag{4.14}$$

where $J_1(k)$ are defined as

$$\left(J_1(k) \equiv J_1 \sum \vec{R_1} e^{-i\vec{k}\cdot\vec{R_1}} \right). \tag{4.15}$$

J_2 terms reduce to

$$= \sum_k 2S \; \left[\; \gamma \left(a^+_k a_k + b^+_k b_k \right) \; \right] \tag{4.16}$$

where γ are defined as

$$\gamma \equiv J_2 \left(\sum_{\vec{R_2}} cos\left(\vec{k} \cdot \vec{R_2}\right) - 1 \right). \tag{4.17}$$

Summing both J_1 and J_2 terms gives final spin Hamiltonian of

$$H = 2S \sum_{\vec{k}} \left\{ J_1(k)\, a_k b_k^+ + J_1(-k)\, a_k^+ b_k + \beta a_k^+ a_k + \beta b_k^+ b_k \right\} \tag{4.18}$$

where β has been defined as

$$\beta \equiv (-J_1(0) + \gamma). \tag{4.19}$$

The eigenenergies are the eigenvalues of the matrix

$$\begin{pmatrix} \beta & J_1(k) \\ J_1(-k) & \beta \end{pmatrix}$$

and it can be easily shown that the eigenvalues of the above matrix are

$$\omega = \beta \pm \sqrt{J_1(k)\, J_1(-k)}. \tag{4.20}$$

The eigenvalues can be further simplified by the two relations below,

$$J_1(k)\, J_1(-k) = J_1^2 \sum_{\vec{R_1}, \vec{R_1'}} \left\{ cos\left(\vec{k} \cdot \left(\vec{R_1} - \vec{R_1'}\right)\right) \right\} \tag{4.21}$$

and,

$$\beta = -4J_1 - 4J_2 + J_2 \sum_{R_2} cos\left(\vec{k} \cdot \vec{R_2}\right) \tag{4.22}$$

Therefore, the final eigenenergies of the spin Hamiltonian in terms of the wave vector, i.e., spin wave dispersion relation, is

$$\omega = -4J_1 - 4J_2 + J_2 \sum_{R_2} cos\left(\vec{k} \cdot \vec{R_2}\right) \pm |J_1| \sqrt{\sum_{\vec{R_1},\vec{R_1'}} cos\left(\vec{k} \cdot \left(\vec{R_1} - \vec{R_1'}\right)\right)}. \quad (4.23)$$

4.4 Field dependence study

The onset of superconductivity is closely related to the external magnetic field. This relationship is evident for $CeO_{0.3}F_{0.7}BiS_2$ in Figure 4.14. Here we measure the resistivity under different external magnetic fields as a function of temperature in Figure 4.14 (a). We find the transition temperature decreases as we increase the applied field. Superconductivity becomes completely suppressed when H $\approx$ 2T, however, traces of superconductivity are still observed even at higher fields by a drop in resistivity. In Figure 4.14 (b), the resistance is shown in a H-T plane as a contour plot. White dotted lines indicate the boundaries of 10% and 90% of normal state resistivity, corresponding to H_{irr} and H_{c2}, respectively.

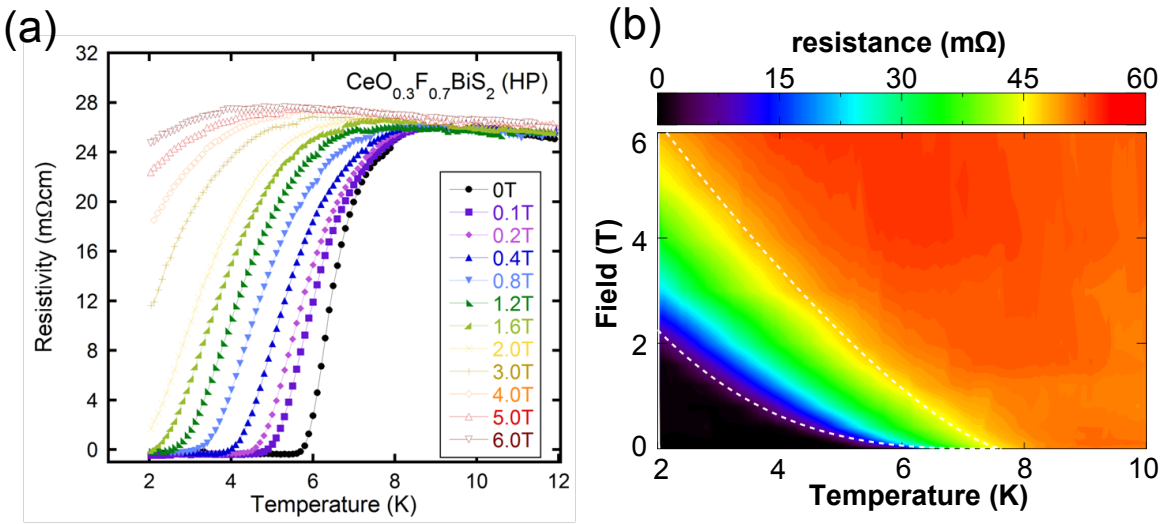

FIGURE 4.14: (a) Resistivity as a function of magnetic field and temperature. (b) Contour map of resistance for better visualization.

To further understand the relationship between the magnetism and superconductivity in this system, we performed neutron scattering experiment at CNCS with fields up to 5 T.

4.4.1 Magnetic structure

Figure 4.15 (a) shows the neutron scattering intensities integrated over the elastic scattering region, E = [-0.5, 0.5], at T = 1.5 K with varying field to find the field dependence of the magnetic structure. We observe strong increase of the Q = (001) Bragg peak, indexed from the lattice parameters obtained by the zero-field neutron powder experiment. In addition, the broad hump in the low Q area, below about 0.5 $\mathring{A}^{-1}$ becomes less pronounced as we increase the magnetic field. This might be related with ordering of magnetic moments in the spin-glassy state due to the external field.

The summed intensities of the Q = (001) Bragg peak as a function of magnetic field are shown in Figure 4.15 (b) at both T = 1.5K, the base temperature, and 5.5K, just below the T_{FM} of zero field. They both increase as we increase the field. At T = 1.5 K, the magnetic moment increases up to 4 T, above which it becomes saturated. At T = 5.5 K, the magnetic moment keeps increasing as the field increases, though it is smaller compared with the magnetic moment at T = 1.5K.

We can compare the observed elastic neutron scattering intensities with the simulated intensities based on the representation theory of magnetic structure as we did in the zero-field study. The Q = (001) magnetic peak can be observed only if the magnetic moments have an ab-plane component. Furthermore, while the ferromangetic spin configuration in the ab-plane results in incomparably strong Q = (001) peak, the antiferromangetic spin configuration in the ab-plane produces other comparable peaks such as Q = (002). Therefore, we can conclude that the spin configuration changes from the ferromagnetic alignment along the c-axis, $\Gamma 3$, to ferromagnetic alignment in the ab-plane, $\Gamma 9$ after applying a field.

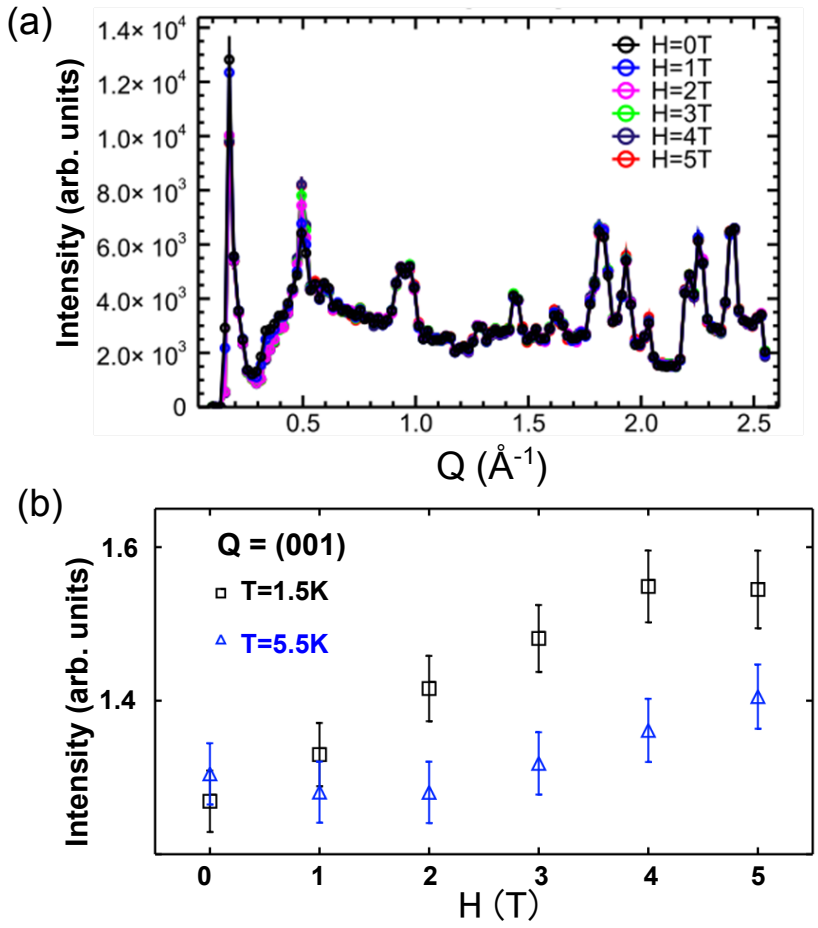

FIGURE 4.15: (a) Onset of magnetic Bragg peak at Q = (001) upon applying external field at T = 1.5 K (b) the summed intensity of the Q = (001) magnetic Bragg peak at T = 1.5 K and T = 5.5 K.

4.4.2 Spin fluctuation under external magnetic field

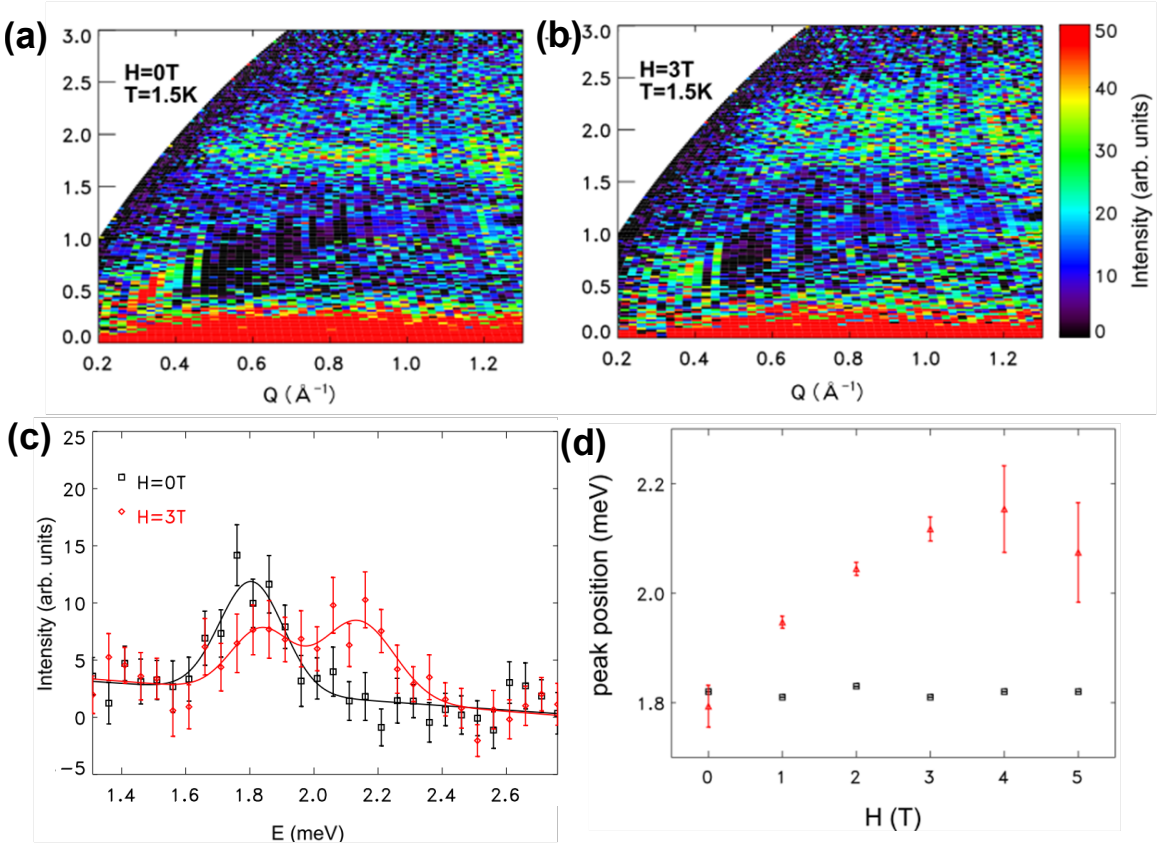

FIGURE 4.16: The change of inelastic neutron scattering with external magnetic field.

We also investigated the change of spin fluctuation upon applying an external field. It should be noted that there is a He-roton excitation ranging between E = [0.5, 1.5] meV at T = 1.5K in this experiment setup, which has been removed manually by Gaussian fitting the excitation.

As shown in Figure 4.16, we observed a broadening of spin wave excitation under a field. This broadening is clear when we plot the neutron scattering intensity versus energy transfer at different fields, for example, at H = 0 T and 3 T as in Figure 4.16 (a) and (b). At zero field, there is a single peak centered at E = 1.8meV. This peak split into two peaks, one of which remains nearly at the same starting position, while

the other peak moves to higher energy transfer as the external field increases.

This trend becomes evident in Figure 4.16 (c) where we plot the neutron scattering intensity along energy transfer at two different magnetic fields. Figure 4.16 (d) shows the Gauss fitted peak positions of the two peaks at different fields at T = 1.5 K. Above 4 T, the uncertainties in the peak positions are larger due to the weak signal and insufficient neutron counting time.

The splitting of the ferromagnetic spin wave under external magnetic field is, in fact, very unusal. As can be inferred from the analytical form of eigenenergies of spin Hamiltonian, the whole spin wave dispersion is expected to be just shifted by the amount proportional to the magnitude of external magnetic field, $g\mu_B BS$. It may be possible other mechanisms like dipole-dipole interactions might be responsible for the field dependent splitting, in which case the role of exchange interactions and dipolar interactions in magnetism and superconductivity needs to be clarified more in more detail. Further analysis would be required to understand this unusual behavior.

4.5 Conclusion

In this chapter, we have studied the rare case of coexistence of ferromagnetism and superconductivity in the $CeO_{0.3}F_{0.7}BiS_2$ system. The crystal structure and magnetic structure were studied.

The neutron powder diffraction data shows significant broadening as other systems in this new BiS_2-based superconductor family. Although there were large broadening and several impurities, we could fit the structure with the space group P 4/n m m reasonably well.

The magnetic structure was investigated by comparing with simulated elastic magnetic scattering intensities using group theoretical analysis. The magnetic moments align ferromagnetically along the c-axis, which, upon application of external magnetic field, flips to the ab-plane with ferromagnetic spin configuration.

By measuring the spin wave with inelastic neutron scattering method, we could model the spin Hamiltonian in this system. The Heisenberg isotropic exchange interaction with NN and NNN interaction was able to describe the observed spin fluctuation. By applying a magnetic field up to 5 T, we could observe the splitting of the spin fluctuation. There is an excitation that remains at the same position around E = 1.8meV, and another excitation moves up as the field increases.

Chapter 5

Conclusion

The nature of superconductivity in the new family of BiS_2-layer superconductors has been investigated in this dissertation. Several theories have presented different scenarios of superconducting mediating mechanisms for the BiS_2-based systems: conventional phonons [60, 61, 64], spin density waves [57, 58, 63], or charge density waves [60, 64]. To shed light on the nature of superconductivity, we have studied two systems, La(O,F)BiS_2 and $CeO_{0.3}F_{0.7}BiS_2$, using neutron scattering.

In particular, for $LaO_{1-x}F_xBiS_2$, we have investigated the crystal structure and lattice vibrations as a function of temperature at two different F-doping levels, non-SC $LaOBiS_2$ and SC $LaO_{0.5}F_{0.5}BiS_2$. For $CeO_{0.3}F_{0.7}BiS_2$, we have examined the crystal structure, magnetic structure, and magnetic fluctuations either by changing temperature or by varying the external magnetic field.

In the case of $LaOBiS_2$, our neutron powder diffraction data showed large broadening of the nuclear Bragg peaks with non-zero l, indicating structural disorder along the c-axis. Furthermore, a significant difference between the calculated and experimentally refined position of the in-plane S ion was observed in both non-SC and SC compounds. Our inelastic neutron scattering data yielded no detectable change in the phonon spectrum either by doping or by cooling.

The large broadening of Bragg peaks and inconsistency in the in-plane S atomic position suggest a structural instability of the system. Recent research [80] also

reports a close relationship between crystallinity and superconductivity by observing higher T_c in less-crystalline samples. The reason why the structural instability is strong in this system and the mechanism through which the instability is related with superconductivity deserve further investigation.

The little change in the phonon density-of-states of $LaO_{1-x}F_xBiS_2$ implies that the electron-phonon coupling is much weaker than theoretically expected, pointing to an unconventional mechanism for superconductivity. Our inelastic measurements are based on powder samples of solid-angle averaged density-of-states, thus possible weak anomalies may become undetectable. Further studies on single crystals are needed for a more concrete conclusion. Our results still provide important constraints on future theoretical works examining these new BiS_2-based superconductors.

In the $CeO_{0.3}F_{0.7}BiS_2$ system, the neutron powder diffraction also finds large broadening of the nuclear Bragg peaks. Below $T_{FM} \approx 7$ K, the Ce^{3+} magnetic moments begin to align ferromagnetically along the c-axis, and a spin-wave mode around $\hbar\omega \approx 1.8$ meV appears. This spin-wave can be described by a Heisenberg isotropic interaction Hamiltonian with nearest-neighbor and next-nearest-neighbor model. Upon applying an external magnetic field, the magnetic moments flip to the ab-plane with ferromagnetic spin configuration, and the $\hbar\omega \approx 1.8$ meV mode splits into two.

The broad Bragg peaks in $CeO_{0.3}F_{0.7}BiS_2$ suggests that the structural instability can be playing an important role in this sample just like in $LaO_{1-x}F_xBiS_2$. By comparing the magnetism with resistivity either by changing the magnetic field or by changing temperature, no direct relationship between magnetism and superconductivity can be found. In this system, superconductivity seems to be robust against a magnetic field, and there appears no correlation between the two phenomena. Lastly, the split of the mode at 1.8 meV cannot be explained by the isotropic Heisenberg model alone, and requires further investigation on the nature of magnetic interactions in this system.

The BiS_2 system provides us with a venue to study the interplay of structure, phonons and magnetism, and of their role in the superconducting mechanism.

Appendix A

Quantum Espresso

A.1 Install

To install Quantum Espresso(QE), you will need a Linux environment with an up-to-date Fortran and C compilers. If you are using windows, installing the latest version of Cygwin is highly recommended. If you are new to Linux environment like me, it will be easier for you just to follow the sequences below:

1) download the QE program from the official website
http://www.quantum-espresso.org/

2) unzip the downloaded QE under the directory you want
tar zxvf espresso-X.Y.Z.tar.gz

3) configure and make
./configure
make all

4) test if setup is completed
cd PW/tests/
./check_pw.x.j
cd CPV/tests/
./check_cp.x.j

For more help about the setup procedure, please refer to setup user guide in the website.
http://www.quantum-espresso.org/wp-content/uploads/Doc/user_guide.pdf

A.2 Theoretical Background

The atomic position in an equilibrium can be written as

$$\vec{R}_l = \vec{R}_\mu + \vec{d}_s \tag{A.1}$$

where

$\vec{R}_l$: equilibrium positions of each atoms
$\vec{R}_\mu$: Bravais lattice vector
$\vec{d}_s$: position of the atoms in one unit cell (s=1, ..., N_{at})

and

N: number of unit cell
N_{at}: number of atoms in one unit cell.

The atoms are not static, and, at time t, it is displaced from equilibrium center by $\vec{u}_l(t)$.

$\vec{u}_l(t)$: displacement of the atom l at time t

Within the Born-Oppenheimer adiabatic approximation, the nuclei move in a potential energy given by the total energy of the electron system calculated at fixed nuclei, $E_{tot}(\vec{R}_l + \vec{u}_l)$. The electrons are assumed to be in the ground state for each nuclear configuration. When the $|\vec{u}_l|$ is small, within the harmonic approximation,

$$E_{tot}(\vec{R}_l + \vec{u}_l) = E_{tot}(\vec{R}_l) + \sum_{l\alpha} \frac{\partial E_{tot}}{\partial \vec{u}_{l\alpha}} \vec{u}_{l\alpha} + \frac{1}{2} \sum_{l\alpha, l'\beta} \frac{\partial^2 E_{tot}}{\partial \vec{u}_{l\alpha} \partial \vec{u}_{l'\beta}} \vec{u}_{l\alpha} \vec{u}_{l'\beta} + ... \tag{A.2}$$

where the derivatives are calculated at $\vec{u_l} = 0$ and α and β indicate the three cartesian coordinates.

At equilibrium, i.e., $\frac{\partial E_{tot}}{\partial \vec{u}_{l\alpha}} = 0$, the Hamiltonian is:

$$H = \sum_{l\alpha} \frac{\vec{P}_{l\alpha}^2}{2M_l} + \frac{1}{2} \sum_{l\alpha, l'\beta} \frac{\partial^2 E_{tot}}{\partial \vec{u}_{l\alpha} \partial \vec{u}_{l'\beta}} \vec{u}_{l\alpha} \vec{u}_{l'\beta} \tag{A.3}$$

where $\vec{P_l}$: the momenta of the nuclei, and
M_l: masses of the nuclei

The classical motion of the nuclei is given by $3 \times N \times N_{at}$ functions of $\vec{u}_{l\alpha}(t)$. These functions can be obtained by solving the Hamiltonian equations:

$$\begin{aligned} \dot{\vec{u}}_{l\alpha} &= \frac{\partial H}{\partial \vec{P}_{l\alpha}} \\ \dot{\vec{P}}_{l\alpha} &= -\frac{\partial H}{\partial \vec{u}_{l\alpha}} \end{aligned} \tag{A.4}$$

For the given Hamiltonian, these can be re-written as:

$$\begin{aligned}\dot{\vec{u}}_{l\alpha} &= \frac{\vec{P}_{l\alpha}}{M_l} \\ \dot{\vec{P}}_{l\alpha} &= -\sum_{l'\beta} \frac{\partial^2 E_{tot}}{\partial \vec{u}_{l\alpha} \partial \vec{u}_{l'\beta}} \vec{u}_{l'\beta}\end{aligned} \tag{A.5}$$

The two equations in A.5 can be combined to give:

$$M\ddot{\vec{u}}_{l\alpha} = -\sum_{l'\beta} \frac{\partial^2 E_{tot}}{\partial \vec{u}_{l\alpha} \partial \vec{u}_{l'\beta}} \vec{u}_{l'\beta} \tag{A.6}$$

We can insert the solution of the above equation A.6 in the form of a phonon with a momentum wave vector, $\vec{q}$, where we re-wrote $l = (\mu, s)$, $l' = (\nu, s')$. Here, μ, ν represent Bravais lattice, and s, s' represent atoms in a unit cell.

$$\begin{aligned}\vec{u}_{\mu s\alpha} &= \frac{1}{\sqrt{M_s}} \vec{u}_{s\alpha} e^{i\left(\vec{q}\vec{R}_\mu - \omega_{\vec{q}} t\right)} \\ \vec{u}_{\nu s'\beta} &= \frac{1}{\sqrt{M'_s}} \vec{u}_{s'\beta} e^{i\left(\vec{q}\vec{R}_\nu - \omega_{\vec{q}} t\right)}\end{aligned} \tag{A.7}$$

The time dependence is given by $e^{-\omega_{\vec{q}} t}$ and the displacement of the atoms in each unit cell identified by the the Bravais lattice R_μ can be obtained as $\frac{1}{\sqrt{M_s}} \vec{u}_{s\alpha} e^{i\vec{q}\vec{R}_\mu}$.

Inserting this solution A.7 in the equation of motionA.6, we can obtain an eigenvalue problem for the $3 \times N_{at}$ variables of $\vec{u}_{s\alpha}(\vec{q})$:

$$\omega^2_{\vec{q}} \vec{u}_{s\alpha}(\vec{q}) = \sum_{s'\beta} D_{s\alpha s'\beta}(\vec{q}) \vec{u}_{s'\beta}(\vec{q}) \tag{A.8}$$

where D is called the dynamical matrix of the solid,

$$D_{s\alpha s'\beta}(\vec{q}) = \frac{1}{\sqrt{M_s M_{s'}}} \sum_{\nu} \frac{\partial^2 E_{tot}}{\partial \vec{u}_{\mu s\alpha} \partial \vec{u}_{\nu s'\beta}} e^{i\vec{q}\left(\vec{R}_\nu - \vec{R}_\mu\right)} \ . \tag{A.9}$$

Within DFT, the ground state total energy of the solid at fixed nuclei is:

$$E_{tot} = \sum_i \left\langle \psi_i \left| -\frac{1}{2}\nabla^2 \right| \psi_i \right\rangle + \int V_{loc}(\vec{r})\rho(\vec{r})d^3r + E_H\left[\rho\right] + E_{XC}\left[\rho\right] + U_{II} \quad \text{(A.10)}$$

where $|\psi_i\rangle$ is the solution of Kohn-Sham equation, and $\rho(\vec{r})$ is the density of the electron gas:

$$\rho(\vec{r}) = \sum_i \left|\psi_i(\vec{r})\right|^2 \quad \text{(A.11)}$$

E_H is the Hartree energy, E_{XC} is the exchange and the correlation energy, and U_{II} is the ion-ion interaction. According to Hellmann-Feynman theorem,

$$\frac{\partial E_{tot}}{\partial \lambda} = \int \frac{\partial V_{loc}(\vec{r})}{\partial \lambda}\rho(\vec{r})d^3r + \frac{\partial U_{II}}{\partial \lambda} \quad \text{(A.12)}$$

$$\frac{\partial^2 E_{tot}}{\partial \mu \partial \lambda} = \int \frac{\partial^2 V_{loc}(\vec{r})}{\partial \mu \partial \lambda}\rho(\vec{r})d^3r + \int \frac{\partial V_{loc}(\vec{r})}{\partial \lambda}\frac{\rho(\vec{r})}{\partial \mu}d^3r + \frac{\partial^2 U_{II}}{\partial \mu \partial \lambda} \quad \text{(A.13)}$$

The new quantity we need to calculate is the charge density induced, at first order, by the perturbation:

$$\frac{\partial \rho(\vec{r})}{\partial \mu} = \sum_i \frac{\partial \psi_i^*(\vec{r})}{\partial \mu}\psi_i(\vec{r}) + \psi_i^*(\vec{r})\frac{\partial \psi_i(\vec{r})}{\partial \mu} \quad \text{(A.14)}$$

The wave functions obey:

$$\left[-\frac{1}{2}\nabla^2 + V_{KS}(\vec{r})\right]\psi_i(\vec{r}) = \epsilon_i \psi_i(\vec{r}) \quad \text{(A.15)}$$

where $V_{KS} = V_{loc}(\vec{r}) + V_H(\vec{r}) + V_{XC}(\vec{r})$. V_{KS} depends on μ so that $\psi_i(\vec{r},\mu)$ and $\epsilon_i(\mu)$ also depends on μ. We can expand these quantities in a Taylor series:

$$V_{KS}(\vec{r},\mu) = V_{KS}(\vec{r},\mu=0) + \mu\frac{\partial V_{KS}(\vec{r})}{\partial\mu} + ... \tag{A.16}$$

$$\psi_i(\vec{r},\mu) = \psi_i(\vec{r},\mu=0) + \mu\frac{\partial \psi_i(\vec{r})}{\partial\mu} + ... \tag{A.17}$$

$$\epsilon_i(\mu) = \epsilon_i(\mu=0) + \mu\frac{\partial \epsilon_i}{\partial\mu} + ... \tag{A.18}$$

Inserting these expansions to the equation A.15 and keeping only the first order in μ, we obtain:

$$\left[-\frac{1}{2}\nabla^2 + V_{KS}(\vec{r}) - \epsilon_i\right]\frac{\partial\psi_i(\vec{r})}{\partial\mu} = -\frac{\partial V_{KS}}{\partial\mu}\psi_i(\vec{r}) + \frac{\partial\epsilon_i}{\partial\mu}\psi_i(\vec{r}) \tag{A.19}$$

where

$$\frac{\partial V_{KS}}{\partial\mu} = \frac{\partial V_{loc}}{\partial\mu} + \frac{\partial V_H}{\partial\mu} + \frac{\partial V_{XC}}{\partial\mu} \tag{A.20}$$

and

$$\begin{aligned}\frac{\partial V_H}{\partial\mu} &= \int \frac{1}{\left|\vec{r}-\vec{r'}\right|}\frac{\partial\rho(\vec{r'})}{\partial\mu}d^3r' \\ \frac{\partial V_{XC}}{\partial\mu} &= \frac{d\ V_{XC}}{d\ \rho}\frac{\partial\rho(\vec{r})}{\partial\mu}\end{aligned} \tag{A.21}$$

depend self-consistently on the charge density induced by the perturbation.

The induced charge density depends only on $P_c\frac{\partial\psi_i}{\partial\mu}$ where $P_c = 1 - P_v$ is the projector on the conduction bands and $P_v = \sum_i |\psi_i\rangle\langle\psi_i|$ is the projector on the valence bands:

$$\begin{aligned}\frac{\partial\rho(\vec{r})}{\partial\mu} =& \sum_i P_c \frac{\partial\psi_i^*(\vec{r})}{\partial\mu}\psi_i(\vec{r}) + \sum_i \psi_i^*(\vec{r}) P_c \frac{\partial\psi_i(\vec{r})}{\partial\mu} \\ &+ \sum_i P_v \frac{\partial\psi_i^*(\vec{r})}{\partial\mu}\psi_i(\vec{r}) + \sum_i \psi_i^*(\vec{r}) P_v \frac{\partial\psi_i(\vec{r})}{\partial\mu} \\ =& \sum_i P_c \frac{\partial\psi_i^*(\vec{r})}{\partial\mu}\psi_i(\vec{r}) + \sum_i \psi_i^*(\vec{r}) P_c \frac{\partial\psi_i(\vec{r})}{\partial\mu} \\ &+ \sum_{i,j} \psi_j^*(\vec{r})\psi_i(\vec{r}) \left(\left\langle \frac{\partial\psi_i}{\partial\mu} | \psi_j \right\rangle + \left\langle \psi_i | \frac{\partial\psi_j}{\partial\mu} \right\rangle \right)\end{aligned} \tag{A.22}$$

Therefore we can solve the self-consistent linear system:

$$\left[-\frac{1}{2}\nabla^2 + V_{KS}(\vec{r}) - \epsilon_i \right] P_c \frac{\partial\psi_i(\vec{r})}{\partial\mu} = -\frac{\partial V_{KS}}{\partial\mu}\psi_i(\vec{r}) + \frac{\partial\epsilon_i}{\partial\mu}\psi_i(\vec{r}) \tag{A.23}$$

$$\left(\frac{\partial V_{KS}}{\partial\mu} = \frac{\partial V_{loc}}{\partial\mu} + \frac{\partial V_H}{\partial\mu} + \frac{\partial V_{XC}}{\partial\mu} \right) \tag{A.24}$$

$$\frac{\partial\rho(\vec{r})}{\partial\mu} = \sum_i P_c \frac{\partial\psi_i^*(\vec{r})}{\partial\mu}\psi_i(\vec{r}) + \sum_i \psi_i^*(\vec{r}) P_c \frac{\partial\psi_i(\vec{r})}{\partial\mu} \tag{A.25}$$

A.3 Practical Guide

QE can calculate the phonon dispersion using density functional perturbation theory (DFPT). The general approach will be:

1) Calculate the self-consistent charge and potential for your system using pw.x
2) Run DFPT calculations for several q-points in your Brillouin Zone to determine the dymanical matrix and phonon frequencies at each q-points using ph.x
3) Convert the q-space dynamical matrix to the real space interatomic force constants using q2r.x

4) Use the code matdyn.x to interpolate to other q-vectors to et the full phonon dispersion and phonon density of states.

A.3.1 structural optimization

pw.x calculates the self-consistent charge and potential for the given system.

To run the calculation:
/usr/bin/pw.x < scf.in > scf.out

The pw.x will require input such as mass of atoms, Bravais lattice type, lattice parameters, number and type of atoms, atomic positions, potential functions to be used, convergence threshold, etc. It creates output dynG file containing the dynamical matrix information. The information regarding eigenenergies, eigenvectors, and symmetries at the zone center can be found in the output file as well.

A.3.2 phonon at a fixed Q

ph.x solves the self-consistent linear system for $3 \times N_{at}$ perturbations at a fixed wave vector $\vec{q}$. With $\frac{\partial \rho(\vec{r})}{\partial \mu}$ for all the perturbations, it calculates the dynamical matrix, $D_{s\alpha s'\beta}(\vec{q})$, at the given $\vec{q}$. By diagonalizing this matrix, we obtain $3 \times N_{at}$ frequencies $\omega_{\vec{q}}$.

We can run the phonon eigenenergy, eigenvector, and symmetry calculation at a fixed $\vec{q}$, for example, at the Γ position. To run the command:

/usr/bin/ph.x < phG.in > phG.out

The ph.x will require input such as mass of atoms, previously calculated dynamical matrix output file, etc.

A.3.3 phonon dispersion

By repeating the phonon energy calculation for several $\vec{q}$, we can plot $\omega_{\vec{q}}$ as a function of $\vec{q}$ and display the phonon dispersion. However, there is more convenient and computational efficient way which requires smaller set of $\vec{q}$ points.

The dynamical matrix of the solid in the equation A.9

$$D_{s\alpha s'\beta}(\vec{q}) = \frac{1}{\sqrt{M_s M_{s'}}} \sum_{\nu} \frac{\partial^2 E_{tot}}{\partial \vec{u}_{\mu s\alpha} \partial \vec{u}_{\nu s'\beta}} e^{i\vec{q}\left(\vec{R}_\nu - \vec{R}_\mu\right)} \tag{A.26}$$

is a periodic function of $\vec{q}$ with $D_{s\alpha s'\beta}(q + \vec{G}) = D_{s\alpha s'\beta}(\vec{q})$ for reciprocal lattice vector $\vec{G} = \frac{2\pi}{R}$. Therefore, the equation A.9 can be regarded as a Fourier series of a 3 dimensional periodic function. It should be noted that, since in a solid all Bravais lattice points are equivalent, it does not depend on μ. The Fourier components, in turn, can be written as:

$$\frac{1}{\sqrt{M_s M_{s'}}} \frac{\partial^2 E_{tot}}{\partial \vec{u}_{\mu s\alpha} \partial \vec{u}_{\nu s'\beta}} = \frac{\Omega}{(2\pi)^3} \int d^3\vec{q} D_{s\alpha s'\beta}(\vec{q}) e^{-i\vec{q}\left(\vec{R}_\nu - \vec{R}_\mu\right)} \tag{A.27}$$

We can use the properties of the discrete Fourier transform and sample the integral in a uniform mesh of $\vec{q}$ points. This will give the interatomic force constants only for a set of R_ν neighbors of R_μ.

The q2r.x code is used for this job: it will read a set of dynmaical matrices calculated in a uniform mesh of $\vec{q}$ points, and by using the equation A.27, calculates the interatomic force constants for a few neighbors of the point near $R_\mu = 0$.

Let us consider, for example, a toy model with a one dimensional periodic function of $f(x+a) = f(x)$ with period a. This function can be expanded in a Fourier series,

$$f(x) = \sum_n c_n e^{ik_n x} \tag{A.28}$$

which have a discrete set of Fourier components at the points $k_n = \frac{2\pi}{a} n$ (n: integer).

$$c_n = \frac{1}{a} \int_0^a f(x) e^{-ik_n x} dx \tag{A.29}$$

In general, if the periodic function inside the integral, $f(x)$, is a sufficiently smooth, the Fourier component with higher order, c_n goes to zero. Suppose we know $f(x)$ only in a small set of N points:

$$x_j = j\Delta x \ \left(\Delta x = \frac{a}{N},\ j = 0, ..., N-1\right) \tag{A.30}$$

then we can calculate:

$$\widetilde{c_n} = \frac{1}{N} \sum_{j=0}^{N-1} f\left(x_j\right) e^{-i\frac{2\pi}{N} n_j} \tag{A.31}$$

$\widetilde{c_n}$ is a periodic function of n where $\widetilde{c}_{n+N} = \widetilde{c}_n$. If N is sufficiently large that $c_n \to 0$ when $|n| \geq N/2$ then $\widetilde{c_n}$ is a good approximation of c_n for $|n| \leq N/2$ and the function,

$$f\left(x\right) = \sum_{n=-N/2}^{n=+N/2} \widetilde{c_n} e^{ik_n x} \tag{A.32}$$

is a good approximation of the function $f(x)$ also on the points x different from x_j.

Therefore, if the dynamical matrix is a sufficiently smooth function of $\vec{q}$ and the interatomic force constants decay sufficiently rapidly in real space, we can calculate

the dynamical matrix at arbitrary $\vec{q}$, limiting the sum to a few $\vec{R}_\nu$ neighbors of $\vec{R}_\mu = 0$.

To run q2r in order to convert phonon information in q-space into real space force constant files:

/usr/bin/q2r.x < q2r.in > q2r.out

It needs input file which contains dynamical matrix file. Then, it will create output file of fc containing interatomic force constants information.

The matdyn.x program reads the interatomic force constants calculated by q2r.x and calculates the dynamical matrices at an arbitrary $\vec{q}$.

/usr/bin/matdyn.x < matdyn.in > matdyn.out

With input file of fc type, it will create an output list of phonon frequencies in cm^{-1} for each of the q-vectors given in the input list.

A.3.4 phonon density of states

Using the interatomic force constant file generated, you can also calculate the phonon density of states. This is done by sampling a large number of q points in the Brillouin Zone using matdyn.x. The number of q-points is controlled by the Monkhorst-Pack grid parameters, i.e., nk1, nk2, and nk3.

You can run this calculation as:
/usr/bin/matdyn.x < pdos.in > pdos.out

This will generate an phods output file, which contains the density of states as a function of frequency.

Appendix B

Group Theoretical Analysis of Magnetic Structure

B.1 SARAh Representation

SARAh is a program developed to help with group theoretical analysis of the magnetic structure. It is composed of two programs: 'SARAh Representation Analysis' and 'SARAh Refine'. The former is used for the group theoretical analysis, and the latter is for the actual refinement with given representations.

To find out the Irreducible Representations (IRs) of the magnetic structure, we need 3 information: (1) the crystallographic space group, (2) magnetic propagation wave vector (k-vector), and (3) the position of magnetic atoms. The k-vector defines which symmetries of the starting structure are compatible with the translational symmetry of the magnetic structure. Our goal is to find out the symmetry operations of the crystallographic space group, G_0, compatible with the k-vector, as they form the 'little group' or the 'space group of the propagation vector', G_k. From this G_k, we can work out the different symmetry types, and these are the irreducible representation(IR) we are looking for.

First, the crystallographic space group is needed to define the starting symmetry for the calculation. If there is a second order phase transition, the space group before the transition is used, while if it is a first order transition, the space group after the transition should be used. First order phase transitions are those that involve a latent heat, and the system is in a mixed phase during the transition. Second order phase transitions are also called continuous phase transition, and characterized by a divergent susceptibility, an infinite correlation length, and power-law decay of correlations near criticality.

Second, we need the magnetic propagation vector, k-vector. The k-vector is defined with respect to the crystal structure and space group setting. Again, if the transition is of second order, the space group before the transition should be used, and if the transition is of first order, the space group after the transition should be used. The values are limited within the range from -1 to +1 in case of primitive cell, which is not necessarily the case for the centered cells.

Finally, we need the Wyckoff position of the magnetic ions. Other symmetrically equivalent sites will be generated automatically. The valence state and therefore, the magneric form factor is not necessary until we do the actual fitting of the observed data.

The SARAh Representation Analysis can now calculate the irreducible representation with these given information. Either Kovalev's table or ab-initio calculation can be used, while the former is recommended for reference purpose as there is no accepted rules on labeling the IRs. The IRs can be complex but always can be made real by a similarity transformation.

IR should be considered as building blocks of symmetry types. Their symmetries may join together to form irreducible corepresentation when less obvious symmetries, such as time reversal, are considered. The number of IR tells us about the number of different symmetry types that can occur in G_k. Some of these may be shown to be incompatible with the positions used in the calculations. The magnetic moments on

each site are related by the symmetry operations, and these relationships are termed 'basis vectors' (BV). The number of BV associated with an IR is given by multiplication of the repetition with the order of IR. The total number of basis vector, however, should be the same as the multiplication of the number of symmetry related atomic positions bythe number of magnetic moment component (most of the case, 3). That is, group theoretical analysis, does not reduce the number of BVs, but offers the way to systemically categorize them.

The SARAh Representation Analysis will create several files after the calcualtion. The txt file is a general summary, tex file is a report customized to the calculation runs, lst1 file is a summary of IR calculations, lst2 file is a summary of a BV calculations, and mat file is a file used for SARAh Refine. The fst(Fullprof Studio) files can be generated from the mat file, which will visualize each of the BVs. The (approximate) lattice parameters will be asked to make the figure sensible in this course. One should not forget to consult lst2 file to the details of each BVs to understand what they refer to.

B.2 SARAh Refine

SARAh refine will help you to actually refine the magnetic diffraction data using the representation analysis from SARAh Representation Analysis. You will be required to choose either GSAS or Fullprof for this purpose. While the use of GSAS enables one to automatically find the magnetic structure using Reverse Monte Carlo(RMC) method, only Fullprof can refine the magnetic diffraction data in case the the magnetic structure is incommensurate.

Fullprof Control menu enables one to select BVs, and generate model magnetic phases. It contains information such as the number of BVs (N_Bas), and components of the BVs. There resulting BV matrix will have total 3 x N_Bas columns corresponding to x, y, z components of each BVs, and 2 rows corresponding for real and imaginary

component for each Wykoff sites. C's represent the coefficient of mixing for each BVs.

One can manually add this magnetic PCR file to the already existing nuclear phase PCR file, usually just before the angle limits. The profile coefficients need to be replaced to that of the nuclear phase, and the number of phase(Nph) should increase by 1. With these all step finished, one can fit the magnetic structure by varying the mixing coefficients, and changing the BVs in case the model do not work well. The refined magnetic moment can be found in the resultant fst file at the end, or by considering the mixing coefficient and the BV components.

When using the GSAS Control menu, we need to load the mat file as in Fullprof. It is recommended to confirm the positions of magnetic ions by clicking the 'View All Magnetic Atoms' before precede. 'Make Magnetic Phase' menu will automatically set up a new magnetic phase for GSAS. The exp file of the nuclear phase is needed that is to be copied and used as the basis for the magnetic phase. Oxidation state of the magnetic ions will be used to calculate the magnetic form factor in the meanwhile.

Now, with 'Select Basis Vectors - Main Refinement' menu, one can select the basis vectors, set the number of RMC cycles, and let the computer start the refinement. There are many other options and tool which facilitate the magnetic structure refinement, so one is encouraged to consult the web page of the developer, Andrew Wills.

Appendix C

Spin Wave

C.1 spin Hamiltonian

Here, the spin wave dispersion in Chapter 4 is derived in more detail. We consider the isotropic Heisenberg spin Hamiltonian with nearest neighbor and next-nearest neighbor interactions. The first term in Equation 4.1 can be written as

$$H = \sum_i \left\{ J_1 \sum_{\vec{R_1}} \left(\vec{S_A} \cdot \vec{S_B} + \vec{S_B} \cdot \vec{S_A} \right) + J_2 \sum_{\vec{R_2}} \left(\vec{S_A} \cdot \vec{S_{A'}} + \vec{S_B} \cdot \vec{S_{B'}} \right) \right\} \tag{C.1}$$

Here, A and B are ions in different sublattices, and $\vec{R_1}$ and $\vec{R_2}$ are the displacement related to J_1 and J_2, respectively. As can be seen from Figure 4.11, J_1 corresponds to an interlayer coupling, while J_2 corresponds to an intralayer coupling. We can re-write the x and y component of spin S, S^x and S^y, with lowering and raising operator when the z-axis is defined as the quantization

$$\begin{aligned} S^+ &= S^x + iS^y \\ S^- &= S^x - iS^y \end{aligned} \tag{C.2}$$

or,

$$S_A^x S_B^x + S_A^y S_B^y = \frac{1}{2}\left(S_A^+ S_B^- + S_B^- S_A^+\right). \tag{C.3}$$

The dot product of two spins can be represented as

$$S_A \cdot S_B = \frac{1}{2}\left(S_A^+ S_B^- + S_B^- S_A^+\right) + S_A^z S_B^z \tag{C.4}$$

The J_1 terms and J_2 terms in the Hamiltonian are

$$J_1 \sum_{\vec{R_1}} \left(\vec{S_A} \cdot \vec{S_B} + \vec{S_B} \cdot \vec{S_A}\right) \tag{C.5}$$

$$= 2J_1 \sum_{\vec{R_1}} \left(\frac{1}{2}\left(S_A^+ S_B^- + S_B^- S_A^+\right) + S_A^z S_B^z\right), \tag{C.6}$$

$$J_2 \sum_{\vec{R_2}} \left(\vec{S_A} \cdot \vec{S_{A'}} + \vec{S_B} \cdot \vec{S_{B'}}\right) \tag{C.7}$$

$$= J_2 \sum_{\vec{R_2}} \left(\frac{1}{2}\left(S_A^+ S_{A'}^- + S_A^- S_{A'}^+\right) + S_A^z S_A^z + \frac{1}{2}\left(S_B^+ S_{B'}^- + S_B^- S_{B'}^+\right) + S_B^z S_B^z\right). \tag{C.8}$$

With the spin operators applied to eigenstate, $|m\rangle$, with eigenvalue m corresponding the magnetization along the quantized axis, we obtain

$$\begin{aligned} S^z |m\rangle &= m |m\rangle \\ S^+ |m\rangle &= \sqrt{(S-m)(S+m+1)}\, |m+1\rangle \\ S^- |m\rangle &= \sqrt{(S+m)(S-m+1)}\, |m-1\rangle . \end{aligned} \tag{C.9}$$

C.2 Holstein-Primakoff transformation and Linear approximation

To describe spin wave excitations, it is convenient to introduce spin-wave boson operator a^+, for creation, and a, for annihilations with $|n\rangle$ being an eigenstate of a^+a having eigenvalue n corresponding to the spin-deviation quantum number, $n = S-m$. We obtain

$$\left[a,\ a^+\right] = 1 \tag{C.10}$$

$$a\,|n\rangle = \sqrt{n}\,|n-1\rangle\,, \quad a^+\,|n\rangle = \sqrt{n+1}\,|n+1\rangle\,, \quad a^+a\,|n\rangle = n\,|n\rangle\,. \tag{C.11}$$

For sublattice B, another set of bosonic operators b^+ and b are applied in the same way as sublattice A. Equation C.9 is re-written with boson creation and annihilation operator as

$$\begin{aligned} S^z\,|n\rangle &= (S-n)\,|n\rangle \\ S^+\,|n\rangle &= \sqrt{2Sn(1-\frac{n-1}{S})}\,|n-1\rangle \\ S^-\,|n\rangle &= \sqrt{2S(n+1)(1-\frac{n}{2S}}\,|n+1\rangle\,. \end{aligned} \tag{C.12}$$

We simplify the relationship in Equation C.12 if the spin-deviation $n << S$, which is not a strict restriction since a spin-deviation can be spread over all the spin moments as a wave. This is known as the linear approximation which is expressed as

$$\begin{aligned} S^+_{A,i} &\approx \sqrt{2S}a_i & S^+_{B,i} &\approx \sqrt{2S}b_i \\ S^-_{A,i} &\approx \sqrt{2S}a_i^+ & S^-_{B,i} &\approx \sqrt{2S}b_i^+ \\ S^z_{A,i} &\approx S - a_i^+a_i & S^z_{B,i} &\approx S - b_i^+b_i. \end{aligned} \tag{C.13}$$

It should be noted that the signs of the $S_{B,i}$ components are decided by the relationship of the spin directions of the two sublattices. In this approach, therefore, it is essential to know the magnetic ground spin configuration in advance to find the spin wave excitation.

Applying the relationship in Eqaution C.13, the J_1 terms in the Hamiltonian become

$$= 2J_1 S \sum_{\vec{R_1}} \left(a_i b^+_{i+R_1} + a^+_i b_{i+R_1} - a^+_i a_i - b^+_{i+R_1} b_{i+R_1} \right), \tag{C.14}$$

and the J_2 terms become

$$\begin{aligned} = J_2 S \sum_{\vec{R_2}} \; (\; & a_i a^+_{i+R_2} + a^+_i a_{i+R_2} - a^+_i a_i - a^+_{i+R_2} a_{i+R_2} \\ & + b_i b^+_{i+R_2} + b^+_i b_{i+R_2} - b^+_i b_i - b^+_{i+R_2} b_{i+R_2} \;) \; . \end{aligned} \tag{C.15}$$

C.3 Fourier transformation

To find out the dispersion relation, we can Fourier-transform the bosonic operators to momentum space.

$$\begin{aligned} a_i &= \frac{1}{\sqrt{N}} \sum_{\vec{k}} e^{+i\vec{k}\cdot\vec{r_i}} a_{\vec{k}} \qquad b_i = \frac{1}{\sqrt{N}} \sum_{\vec{k}} e^{+i\vec{k}\cdot\vec{r_i}} b_{\vec{k}} \\ a^+_i &= \frac{1}{\sqrt{N}} \sum_{\vec{k}} e^{-i\vec{k}\cdot\vec{r_i}} a^+_{\vec{k}} \qquad b^+_i = \frac{1}{\sqrt{N}} \sum_{\vec{k}} e^{-i\vec{k}\cdot\vec{r_i}} b^+_{\vec{k}} \end{aligned} \tag{C.16}$$

The terms in Equation C.14 is now written as

$$\begin{aligned}
\sum_i \sum_{\vec{R_1}} a_i b^+_{i+R_1} &= \sum_{\vec{k}} \sum_{\vec{R_1}} e^{-i\vec{k}\cdot R_1} a_k b^+_k \\
\sum_i \sum_{\vec{R_1}} a^+_i b_{i+R_1} &= \sum_{\vec{k}} \sum_{\vec{R_1}} e^{+i\vec{k}\cdot R_1} a^+_k b_k \\
\sum_i \sum_{\vec{R_1}} a^+_i a_i &= \sum_{\vec{k}} \sum_{\vec{R_1}} a^+_k a_k \\
\sum_i \sum_{\vec{R_1}} b^+_{i+R_1} b_{i+R_1} &= \sum_{\vec{k}} \sum_{\vec{R_1}} b^+_k b_k,
\end{aligned} \tag{C.17}$$

and the terms in Equation C.15 become

$$\begin{aligned}
\sum_i \sum_{\vec{R_2}} a_i a^+_{i+R_2} &= \sum_{\vec{k}} \sum_{\vec{R_2}} e^{-i\vec{k}\cdot R_2} a_k a^+_k \\
\sum_i \sum_{\vec{R_2}} a^+_i a_{i+R_2} &= \sum_{\vec{k}} \sum_{\vec{R_2}} e^{+i\vec{k}\cdot R_2} a^+_k a_k \\
\sum_i \sum_{\vec{R_2}} b_i b^+_{i+R_2} &= \sum_{\vec{k}} \sum_{\vec{R_2}} e^{-i\vec{k}\cdot R_2} b_k b^+_k \\
\sum_i \sum_{\vec{R_2}} b^+_i b_{i+R_2} &= \sum_{\vec{k}} \sum_{\vec{R_2}} e^{+i\vec{k}\cdot R_2} b^+_k b_k
\end{aligned} \tag{C.18}$$

In the above equation, the relation below (Equation C.19) has been used

$$\sum_{\vec{R}} e^{\left\{i(\vec{k}-\vec{k'})\cdot\vec{R}\right\}} = N\delta_{\vec{k},\vec{k'}}. \tag{C.19}$$

Therefore, J_1 terms reduce to

$$
\begin{aligned}
&= \sum_k 2S \left[\left(J_1 \sum_{\vec{R_1}} e^{-i\vec{k}\cdot\vec{R_1}} \right) a_k b_k^+ + \left(J_1 \sum_{\vec{R_1}} e^{+i\vec{k}\cdot\vec{R_1}} \right) a_k^+ b_k \right. \\
&\qquad \left. - \left(J_1 \sum_{\vec{R_1}} e^{+i\vec{k}\cdot 0} \right) a_k^+ a_k - \left(J_1 \sum_{\vec{R_1}} e^{+i\vec{k}\cdot 0} \right) b_k^+ b_k \right] \\
&= \sum_k 2S \left[J_1(k)\, a_k b_k^+ + J_1(-k)\, a_k^+ b_k - J_1(0)\, a_k^+ a_k - J_1(0)\, b_k^+ b_k \right]
\end{aligned}
\tag{C.20}
$$

where $J_1(k)$ are defined as

$$
\left(J_1(k) \equiv J_1 \sum \vec{R_1} e^{-i\vec{k}\cdot\vec{R_1}} \right). \tag{C.21}
$$

J_2 terms reduce to

$$
\begin{aligned}
&= \sum_k S \left[\left(J_2 \sum_{\vec{R_2}} e^{-i\vec{k}\cdot\vec{R_2}} \right) a_k a_k^+ + \left(J_2 \sum_{\vec{R_2}} e^{+i\vec{k}\cdot\vec{R_2}} \right) a_k^+ a_k - \sum_{R_2} 2J_2 a_k^+ a_k \right. \\
&\qquad \left. - \left(J_2 \sum_{\vec{R_2}} e^{-i\vec{k}\cdot\vec{R_2}} \right) b_k b_k^+ - \left(J_2 \sum_{\vec{R_2}} e^{+i\vec{k}\cdot\vec{R_2}} \right) b_k^+ b_k - \sum_{R_2} 2J_2 b_k^+ b_k \right] \\
&= \sum_k S \left[\left(2J_2 \sum_{\vec{R_2}} cos\left(\vec{k}\cdot\vec{R_2}\right) \right) a_k^+ a_k - \sum_{R_2} 2J_2 a_k^+ a_k \right. \\
&\qquad \left. - \left(2J_2 \sum_{\vec{R_2}} cos\left(\vec{k}\cdot\vec{R_2}\right) \right) b_k^+ b_k - \sum_{R_2} 2J_2 b_k^+ b_k \right] \\
&= \sum_k 2S \left[J_2 \left(\sum_{\vec{R_2}} cos\left(\vec{k}\cdot\vec{R_2}\right) - 1 \right) \left(a_k^+ a_k + b_k^+ b_k \right) \right] \\
&= \sum_k 2S \left[\gamma \left(a_k^+ a_k + b_k^+ b_k \right) \right]
\end{aligned}
\tag{C.22}
$$

where γ are defined as

$$\gamma \equiv J_2 \left(\sum_{\vec{R}_2} cos\left(\vec{k} \cdot \vec{R}_2\right) - 1 \right). \tag{C.23}$$

In the above equation, this relation below (Equation C.24 has been used to simplify the equation.

$$\begin{aligned} \left[a_{\vec{k}}^{+}, a_{\vec{k}}\right] &= a_{\vec{k}}^{+} a_{\vec{k}} - a_{\vec{k}} a_{\vec{k}}^{+} = 1 \\ \left[b_{\vec{k}}^{+}, b_{\vec{k}}\right] &= b_{\vec{k}}^{+} b_{\vec{k}} - b_{\vec{k}} b_{\vec{k}}^{+} \ = 1 \end{aligned} \tag{C.24}$$

Summing both J_1 and J_2 terms gives final spin Hamiltonian of

$$\begin{aligned} H =& 2S \sum_{\vec{k}} \left\{ J_1(k)\, a_k b_k^{+} + J_1(-k)\, a_k^{+} b_k + \left(-J_1(0) + \gamma\right) a_k^{+} a_k + \left(-J_1(0) + \gamma\right) b_k^{+} b_k \right\} \\ =& 2S \sum_{\vec{k}} \left\{ J_1(k)\, a_k b_k^{+} + J_1(-k)\, a_k^{+} b_k + \beta a_k^{+} a_k + \beta b_k^{+} b_k \right\} \end{aligned} \tag{C.25}$$

where β has been defined as

$$\beta \equiv \left(-J_1(0) + \gamma\right). \tag{C.26}$$

C.4 Diagonalization of spin Hamiltonian matix

The eigenenergies are the eigenvalues of the matrix

$$\begin{pmatrix} \beta & J_1(k) \\ J_1(-k) & \beta \end{pmatrix}$$

and it can be easily shown that the eigenvalues of the above matrix are

$$\omega = \beta \pm \sqrt{J_1(k)\, J_1(-k)}. \tag{C.27}$$

The eigenvalues can be further simplified by the two relations below,

$$\begin{aligned} J_1(k)\, J_1(-k) &= J_1^2 \sum_{\vec{R}_1} e^{-i\vec{k}\cdot\vec{R}_1} \sum_{\vec{R}_1'} e^{+i\vec{k}\cdot\vec{R}_1'} \\ &= J_1^2 \sum_{\vec{R}_1,\vec{R}_1'} e^{-i\vec{k}\cdot\vec{R}_1 - \vec{R}_1'} \\ &= J_1^2 \sum_{\vec{R}_1,\vec{R}_1'} \left\{ cos\left(\vec{k}\cdot\left(\vec{R}_1 - \vec{R}_1'\right)\right) - isin\left(\vec{k}\cdot\left(\vec{R}_1 - \vec{R}_1'\right)\right)\right\} \\ &= J_1^2 \sum_{\vec{R}_1,\vec{R}_1'} \left\{ cos\left(\vec{k}\cdot\left(\vec{R}_1 - \vec{R}_1'\right)\right)\right\} \end{aligned} \tag{C.28}$$

and,

$$\beta = \sum_{\vec{R}_2} \left\{ cos\left(\vec{k}\cdot\vec{R}_2\right) - 1\right\} - \sum_{\vec{R}_1} J_1 = -4J_1 - 4J_2 + J_2 \sum_{R_2} cos\left(\vec{k}\cdot\vec{R}_2\right) \tag{C.29}$$

Therefore, the final eigenenergies of the spin Hamiltonian in terms of the wave vector, i.e., spin wave dispersion relation, is

$$\omega = -4J_1 - 4J_2 + J_2 \sum_{R_2} cos\left(\vec{k}\cdot\vec{R}_2\right) \pm |J_1| \sqrt{\sum_{\vec{R}_1,\vec{R}_1'} cos\left(\vec{k}\cdot\left(\vec{R}_1 - \vec{R}_1'\right)\right)}. \tag{C.30}$$

Bibliography

[1] H. K. Onnes, Commun. Phys. Lab. Univ. Leiden **12**, 120 (1911).

[2] W. Meissner and R. Ochsenfeld, Naturwissenschaften **21**, 787 (1933).

[3] Electric power transmission and distribution losses, The World Bank, Retrived 09/10/2013, http://data.worldbank.org/indicator/EG.ELC.LOSS.ZS.

[4] D. van Delft and P. Kes, Phys. Today **63**, 38 (2010).

[5] L. N. Cooper, Phys. Rev. **104**, 1189 (1956).

[6] J. Bardeen, L. N. Cooper, and J. R. Schrieffer, Phys. Rev. **106**, 162 (1957).

[7] J. Bardeen, L. N. Cooper, and J. R. Schrieffer, Phys. Rev. **108**, 1175 (1957).

[8] M. N. Chernodub, arXiv: 1208.5025 (2012).

[9] N. D. Mathur, F. M. Grosche, S. R. Julian, I. R. Walker, D. M. Freye, R. K. W. Haselwimmer, and G. G. Lonzarich, Nature **394**, 39 (1998).

[10] Q. Si and F. Steglich, Science **329**, 1161 (2010).

[11] G. M. Eliashberg, Sov. Phys. JETP **11**, 696 (1960).

[12] M. R. Norman, Science, **332**, 196 (2011).

[13] I. I. Mazin, Nature **464**, 183 (2010)

[14] A. J. Leggett, Rev. Mod. Phys. **47**, 331 (1975).

[15] Y. Maeno, H. Hashimoto, K. Yoshida, S. Nishizaki, T. Fujita, J. G. Bednorz, and F. Lichtenberg, Nature **372**, 532 (1994).

[16] K. D. Nelson, Z. Q. Mao, Y. Maeno, and Y. Liu, Science **306**, 1151 (2004).

[17] G. Burns, High-temperature superconductivity (Academic Press Inc., 1992).

[18] P. C. Canfield and G. W. Crabtree, Phys. Today **56**, 34 (2003).

[19] J. Nagamatsu, N. Nakagawa, T. Muranaka, Y. Zenitani, and J. Akimitsu, Nature **410**, 63 (2001).

[20] J. Kortus, I. I. Mazin, K. D. Belashchenko, V. P. Antropov, and L. L. Boyer, Phys. Rev. Lett. **86**, 4656 (2001).

[21] S. L. Bud'ko, G. Lapertot, C. Petrovic, C. E. Cunningham, N. Anderson, and P. C. Canfield, Phys. Rev. Lett. **86**, 1877 (2001).

[22] D. G. Hinks, H. Claus, and J. D. Jorgensen, Nature **411**, 457 (2001).

[23] P. C. Canfield, S. L. Bud'ko, D. K. Finnemore, Physica C **385**, 1 (2003).

[24] R. A. Ribeiro, S. L. Bud'ko, C. Petrovic, P. C. Canfiel, Physica C **382**, 194 (2002).

[25] J. M. An and W. E. Pickett, Phys. Rev. Lett. **86**, 4366 (2001).

[26] H. J. Choi, D. Roundy, H. Sun, M. L. Cohen, and S. G. Louie, Phys. Rev. B **66**, 020513(R) (2002).

[27] H. J. Choi, D. Roundy, H. Sun, M. L. Cohen, and S. G. Louie, Nature **418**, 758 (2002).

[28] M. Angst, R. Puzniak, A. Wisniewski, J. Jun, S. M. Kazakov, J. Karpinski, J. Roos, and H. Keller, Phys. Rev. Lett. **88**, 167004 (2002).

[29] U. Welp, A. Rydh, G. Karapetrov, W. K. Kwok, G. W. Crabtree, Ch. Marcenat and L. Paulius, T. Klein, J. Marcus, K. H. P. Kim, C. U. Jung, H.-S. Lee, B. Kang, and S.-I. Lee, Phys. Rev. B **67**, 012505 (2003).

[30] F. Bouquet, R. A. Fisher, N. E. Phillips, D. G. Hinks, and J. D. Jorgensen, Phys. Rev. Lett **87**, 047001 (2001).

[31] Y. Wang, T. Plackowski, A. Junod, Physica C, **355**, 179 (2001).

[32] C. Buzea and T. Yamashita, Supercond. Sci. Tech. **14**, 115 (2001).

[33] JST Breakthrough Report, Japan Science and Technology Agency, Retrived 09/12/2013, http://www.jst.go.jp/EN/research/bt07_en.html.

[34] J. G. Bednorz and K. A. Müller, Z. Physik. B **64**, 189 (1986).

[35] P. Morel and P. W. Anderson, Phys. Rev. **125**, 1263 (1962).

[36] C. W. Chu, L. Gao, F. Chen, Z. J. Huang, R. L. Meng and Y. Y. Xue, Nature **365**, 323 (1993).

[37] Y. Kamihara, T. Watanabe, M. Hirano, and H. Hosono, J. Am. Chem. Soc. **130**, 3296 (2008).

[38] C. Wang, L. Li, S. Chi, Z. Zhu, Z. Ren, Y. Li, Y. Wang, X. Lin, Y. Luo, S. Jiang, X. Xu, G. Cao and Z. Xu, Europhys. Lett. **83**, 67006 (2008).

[39] K. Momma and F. Izumi, J. Appl. Crystallogr. **44**, 1272 (2011).

[40] J. M. Tranquada, H. Woo, T. G. Perring, H. Goka, G. D. Gu, G. Xu, M. Fujita and K. Yamada, Nature **429**, 534 (2004).

[41] J. M. Tranquada, B. J. Sternlieb, J. D. Axe, Y. Nakamura and S. Uchida, Nature **375**, 561 (1995).

[42] H. Kontani and S. Onari, Phys. Rev. Lett. **104**, 157001 (2010).

[43] A. Cho, Science **327**, 1320 (2010).

[44] S. A. Kievelson, I. P. Bindloss, E. Fradkin, V. Oganesyan, J. M. Tranquada, A. Kapitulnik and C. Howald, Rev. Mod. Phys. **75**, 1201 (2003).

[45] V. J. Emery, S. A. Kivelson, and J. M. Tranquada, Proc. Natl. Acad. Sci. **96**, 8814 (1999).

[46] Y Mizuguchi, Y. Hara, K. Deguchi, S. Tsuda, T. Yamaguchi, K. Takeda, H. Kotegawa, H. Tou and Y. Takano, Supercond. Sci. Tech. **23**, 054013 (2010).

[47] C. -H. Lee, A. Iyo, H. Eisaki, H. Kito, M. T. Fernandez-Diaz, T. Ito, K. Kihou, H. Matsuhata, M. Braden, and K. Yamada, J. Phys. Soc. Jpn. **77**, 083704 (2008).

[48] P. Dai, J. Hu, and E. Dagotto, Nat. Phys. **8**, 709 (2012).

[49] M. A. Kastner, R. J. Birgeneau, G. Shirane, and Y. Endoh, Rev. Mod. Phys. **70**, 897 (1998).

[50] N. P. Armitage, P. Fournier, and R. L. Greene, Rev. Mod. Phys. **82**, 2521 (2010).

[51] Y. Mizuguchi, S. Demura, K. Deguchi, Y. Takano, H. Fujihisa, Y. Gotoh, H. Izawa, and O. Miura, Phys. Rev. B **86**, 220510(R) (2012).

[52] Y. Mizuguchi, S. Demura, K. Deguchi, Y. Takano, H. Fujihisa, Y. Gotoh, H. Izawa, and O. Miura, J. Phys. Soc. Jpn. **81**, 114725 (2012).

[53] S. Demura, Y. Mizuguchi, K. Deguchi, H. Okazaki, H. Hara, T. Watanabe, S. J. Denholme, M. Fujioka, T. Ozaki, H. Fujihisa, Y. Gotoh, O. Miura, T. Yamaguchi, H. Takeya, and Y. Takano, J. Phys. Soc. Jpn. **82**, 033708 (2013).

[54] R. Jha, S. Kumar Singh, and V. P. S. Awana, J. Supercond. Nov. Magn. **26**, 499 (2013).

[55] J. Xing, S. Li, X. Ding, H. Yang, and H. -H. Wen, Phys. Rev. B **86**, 214518 (2012).

[56] D. Yazici, K. Huang, B. D. White, A. H. Chang, A. J. Friedman, and M. B. Maple, Philos. Mag. **93**, 673 (2013).

[57] H. Usui, K. Suzuki, and K. Kuroki, Phys. Rev. B **86**, 220501(R) (2012).

[58] T. Zhou and Z. D. Wang, J. Supercond. Nov. Magn. **26**, 2735 (2012).

[59] V. P. S. Awana, A. Kumar, R. Jha, S. Kumar, J. Kumar, A. Pal, Shruti, J. Saha, and S. Patnaik, Solid State Commun. **157**, 21 (2013)

[60] X. Wan, H. -C. Ding, S. Y. Savrasov, and C. -G. Duan, Phys. Rev. B **87**, 115124 (2013).

[61] B. Li, Z. W. Xing, and G. Q. Huang, Europhys. Lett. **101**, 47002 (2013).

[62] S. L. Liu, arXiv: 1210.2154v2 (2013).

[63] G. B. Martins, A. Moreo and E. Dagotto, Phys. Rev. B **87**, 081102(R) (2013).

[64] T. Yildirim, Phys. Rev. B **87**, 020506(R) (2013).

[65] K. Deguchi, Y. Mizuguchi, S. Demura, H. Hara, T. Watanabe, S. J. Denholme, M. Fujioka, H. Okazaki, T. Ozaki, H. Takeya, T. Yamaguchi, O. Miura, and Y. Takano, Europhys. Lett. **101**, 17004 (2013).

[66] S. Li, H. Yang, J. Tao, X. Ding, and H. -H. Wen, Sci China Phys Mech Astron **56**, 2019 (2013).

[67] S. K. Singh, A. Kumar, B. Gahtori, S. Kirtan, G. Sharma, S. Patnaik, and V. P. S. Awana, J. Am. Chem. Soc. **134**, 16504 (2012).

[68] H. Kotegawa, Y. Tomita, H. Tou, H. Izawa, Y. Mizuguchi, O. Miura, S. Demura, K. Deguchi, and Y. Takano, J. Phys. Soc. Jpn. **81**, 103702 (2012).

[69] K. Miyake and O. Narikiyo, Phys. Rev. Lett. **83**, 1423 (1999).

[70] A. Huq, J. P. Hodges, O. Gourdon, L. Heroux, Z. Kristallogr. **1**, 127 (2011).

[71] D. L. Abernathy, M. B. Stone, M. J. Loguillo, M. S. Lucas, O. Delaire, X. Tang, J. Y. Y. Lin, B. Fultz, Rev. Sci. Instrum. **83**, 15114 (2012).

[72] G. Ehlers, A. A. Podlesnyak, J. L. Niedziela, E. B. Iverson, P. E. Sokol, Rev. Sci. Instrum. **82**, 85108 (2011).

[73] P. Giannozzi, S. Baroni, N. Bonini, M. Calandra, R. Car, C. Cavazzoni, D. Ceresoli, G. L. Chiarotti, M. Cococcioni, I. Dabo, A. Dal Corso, S. Fabris, G. Fratesi, S. de Gironcoli, R. Gebauer, U. Gerstmann, C. Gougoussis, A. Kokalj, M. Lazzeri, L. Martin-Samos, N. Marzari, F. Mauri, R. Mazzarello, S. Paolini, A. Pasquarello, L. Paulatto, C. Sbraccia, S. Scandolo, G. Sclauzero, A. P. Seitsonen, A. Smogunov, P. Umari, and R. M. Wentzcovitch, J. Phys.: Condens. Mat. **21**, 395502 (2009).

[74] J. P. Perdew, K. Burke, and M. Ernzerhof, Phys. Rev. Lett. **77**, 3865 (1996).

[75] C. Larson and R. B. von Dreele, Los Alamos National Laboratory Tech. Report No. LAUR 86, (2000).

[76] P. W. Stephens, J. Appl. Cryst. **32** , 281 (1999).

[77] S. W. Lovesey, Theory of Neutron Scattering from Condensed Matter Vol. 1 (Clarendon, Oxford, 1984).

[78] G. L. Squires, Introduction to the Theory of Thermal Neutron Scattering (Cambridge Univ. Press, 1978).

[79] V. F. Sears, E. C. Svensson, and B. M. Powell, Can. J. Phys. **73**, 726 (1995).

[80] J. Kajitani, K. Deguchi, A. Omachi, T. Hiroi, Y. Takano, H. Takatsu, H. Kadowaki, O. Miura, Y. Mizuguchi, arXiv: 1306:3346 (2013).

[81] D. Belitz, Phys. Rev. B **36**, 47 (1987).

[82] A. A. Abrikosov and L. P. Gor'kov, Sov. Phys. JETP **12**, 1243 (1961)

[83] V. L. Ginzburg, Zh. Eksp. Teor. Fiz. **31**, 202 (1956).

[84] A. M. Clogston, Phys. Rev. Lett. **9**, 266 (1962).

[85] B. S. Chandrasekhar, Appl. Phys. Lett. **1**, 7 (1962).

[86] J. W. Lynn, G. Shirane, W. Thomlinson, R. N. Shelton, and D. E. Moncton, Phys. Rev. B **24**, 3817 (1981).

[87] O. Fischer and M. B. Maple, Superconductivity in Ternary Compounds I, Topics in Current Physics, vol. 32 (Springer, Berlin, 1982).

[88] M. B. Maple and O. Fischer, Superconductivity in Ternary Compounds II, Topics in Current Physics, vol. 34 (Springer, Berlin, 1982).

[89] M. B. Maple, R. E. Baumbach, J. J. Hamlin, D. A. Zocco, B. J. Taylor, N. P. Butch, J. R. Jeffries, S. T. Weir, B. C. Sales, D. Mandrus, M. A. McGuire, A. S. Sefat, R. Jin, Y. K. Vohra, J. -H. Chu, and I. R. Fisher, Physica B **404**, 2924 (2009).

[90] K. -H. M*ü*ller and V. N. Narozhnyi, Rep. Prog. Phys. **64** 943 (2001).

[91] H. Takagi, M. Nohara, and R.J. Cava, Physica B **237**, 292 (1997).

[92] M. El Massalami, R. -M. Galera, D. Schmitt, B. Ouladdiaf, and H. Takeya, Phys. Rev. B **72**, 144521 (2005).

[93] S. -M Choi, J. W. Lynn, D. Lopez, P. L. Gammel, P. C. Canfield, and S. L. Bud'ko, Phys. Rev. Lett. **87**, 107001 (2001).

[94] A. J. Campbell, D. McK Paul, and G. J. McIntyre, Solid State Comm. **115**, 213 (2000).

[95] B. Lorenz and C. -W. Chu, Nat. Materials **4**, 516 (2005).

[96] L. N. Bulaevskii, A. I. Buzdin, M. L. Kulić, and S. V. Panjukov, Adv. Phys. **34**, 175 (1985).

[97] F. Hardy, A. Huxley, J. Flouquet, B. Salce, G. Knebel, D. Braithwaite, D. Aoki, M. Uhlarz, and C. Pfleiderer, Physica B **359**, 1111 (2005).

[98] N. T. Huy, A. Gasparini, D. E. de Nijs, Y. Huang, J. C. P. Klaasse, T. Gortenmulder, A. de Visser, A. Hamann, T. Görlach, and H. v. Löhneysen, Phys. Rev. Lett. **99**, 067006 (2007).

[99] N. T. Huy, D. E. de Nijs, Y. K. Huang, and A. de Visser, Phys. Rev. Lett. **100**, 077002 (2008).

[100] T. C. Kobayashi, S. Fukushima, H. Hidaka, H. Kotegawa, T. Akazawa, E. Yamamoto, Y. Haga, R. Settai, and Y. Onuki, Physica B **378**, 355 (2007).

[101] T. C. Kobayashi, A. Hori, S. Fukushima, H. Hidaka, H. Kotegawa, T. Akazawa, K. Takeda, Y. Ohishi, and E. Yamamoto, J. Phys. Soc. Jpn. **76**, 051007 (2007).

[102] F. Lévy, I. Sheikin, B. Grenier, and A. D. Huxley, Science **309**, 1343 (2005).

[103] S. S. Saxena, P. Agarwal, K. Ahilan, F. M. Grosche, R. K. W. Haselwimmer, M. J. Steiner, E. Pugh, I. R. Walker, S. R. Julian, P. Monthoux, G. G. Lonzarich, A. Huxley, I. Sheikin, D. Braithwaite, and J. Flouquet, Nature **406**, 587 (2000).

[104] D. Aoki, T. D. Matsuda, V. Taufour, E. Hassinger, G. Knebel, and J. Flouquet, J. Phys. Soc. Jpn. **78**, 113709 (2009).

[105] D. Aoki, A. Huxley, E. Ressouche, D. Braithwaite, J. Flouquet, J. -P. Brison, E. Lhotel, and C. Paulsen, Nature **413**, 613 (2001).

[106] D. Aoki, F. Hardy, A. Miyake, V. Taufour, T. D. Matsuda, and J. Flouquet, C. R. Physique **12**, 573 (2011).

[107] C. Pfleiderer and A. D. Huxley, Phys. Rev. Lett. **89**, 147005 (2002).

[108] I. Felner, U. Asaf, Y. Levi, and O. Millo, Phys. Rev. B **55**, 3374 (1997).

[109] A. C. Mclaughlin, I. Felner, and V. P. S. Awana, Phys. Rev. B **78**, 094501 (2008).

[110] G. V. M. Williams and S. Krämer, Phys. Rev. B **62**, 4132 (2000).

[111] O. Chmaissem, J. D. Jorgensen, H. Shaked, P. Dollar, and J. L. Tallon, Phys. Rev. B **61**, 6401 (2000).

[112] N. M. Souza-neto, D. Haskel, J. C. Lang, O. Chmaissem, B. Dabrowski, and I. Felner, Phys. Rev. B **80**, 140414(R) (2009).

[113] G. I. Leviev, M. I. Tsindlekht, E. B. Sonin, and I. Felner, Phys. Rev. B **70**, 212503 (2004).

[114] W. -H. Jiao, Q. Tao, J. -K. Bao, Y. -L. Sun, C. -M. Feng, Z. -A. Xu, I. Nowik, I. Felner and G. -H. Cao, Europhys. Lett. **95**, 67007 (2011).

[115] G. Cao, S. Xu, Z. Ren, S. Jiang, C. Feng and Z. Xu, J. Phys.: Condens. Mat. **23**, 464204 (2011).

[116] S. Jiang, H. Xing, G. Xuan, Z. Ren, C. Wang, Z. -A. Xu, and G. Cao, Phys. Rev. B **80**, 184514 (2009).

[117] S. Zapf, D. Wu, L. Bogani, H. S. Jeevan, P. Gegenwart, and M. Dressel, Phys. Rev. B **84**, 140503(R) (2011).

[118] Z. Ren, Q. Tao, S. Jiang, C. Feng, C. Wang, J. Dai, G. Cao, and Z. Xu, Phys. Rev. Lett. **102**, 137002 (2009).

[119] H. S. Jeevan, D. Kasinathan, H. Rosner, and P. Gegenwart, Phys. Rev. B **83**, 054511 (2011).

[120] J. Xing, S. Li, X. Ding, H. Yang, and H. -H. Wen, Phys. Rev. B **86**, 214518 (2012).

[121] Y. Luo, Y. Li, S. Jiang, J. Dai, G. Cao, and Z. -A. Xu, Phys. Rev. B **81**, 134422 (2010).

[122] Y. Luo, H. Han, S. Jiang, X. Lin, Y. Li, J. Dai, G. Cao, and Z. -A. Xu, Phys. Rev. B **83**, 054501 (2011).

[123] R. Sarkar, M. Baenitz, A. Jesche, C. Geibel, and F. Steglich, J. Phys.: Condens. Mat. **24**, 135602 (2012).

[124] A. Jesche, T. Förster, J. Spehling, M. Nicklas, M. de Souza, R. Gumeniuk, H. Luetkens, T. Goltz, C. Krellner, M. Lang, J. Sichelschmidt, H. -H. Klauss, and C. Geibel, Phys. Rev. B **86**, 020501(R) (2012).

[125] B. Lorentz and C. -W. Chu, Nature Mat. **4**, 516 (2005).

[126] J. Xing, S. Li, X. Ding, H. Yang, and H. -H. Wen, Phys. Rev. B **86**, 214518 (2012).

[127] J. Rodriguez-Carvajal, Physica B **192**, 55 (1993).